

8-25-2016

Topics in the Physics of Supernovae and Neutron Stars

Sajad Abbar

Follow this and additional works at: https://digitalrepository.unm.edu/phyc_etds

Recommended Citation

Abbar, Sajad. "Topics in the Physics of Supernovae and Neutron Stars." (2016). https://digitalrepository.unm.edu/phyc_etds/1

This Dissertation is brought to you for free and open access by the Electronic Theses and Dissertations at UNM Digital Repository. It has been accepted for inclusion in Physics & Astronomy ETDs by an authorized administrator of UNM Digital Repository. For more information, please contact disc@unm.edu.

Sajad Abbar

Candidate

Physics and Astronomy

Department

This dissertation is approved, and it is acceptable in quality and form for publication:

Approved by the Dissertation Committee:

Dr. Huaiyu Duan, Chairperson (University of New Mexico)

Dr. Rouzbeh Allahverdi (University of New Mexico)

Dr. Akimasa Miyake (University of New Mexico)

Dr. Sanjay Reddy (University of Washington)

Topics in the Physics of Supernovae and Neutron Stars

by

Sajad Abbar

B.S., Physics, Islamic Azad University, 2006

M.S., Physics, Sharif University of Technology, 2009

DISSERTATION

Submitted in Partial Fulfillment of the
Requirements for the Degree of

Doctor of Philosophy
Physics

The University of New Mexico

Albuquerque, New Mexico

July, 2016

DEDICATION

I dedicate my dissertation work to my parents, for their continuous support, my wife, for her unceasing love, and all people helped me in preparing this work.

ACKNOWLEDGMENTS

Firstly, I would like to thank my advisor Dr. Huaiyu Duan for his continuous support during my Ph.D, for his unceasing patience, and motivation. He supported me in all the time during my research and writing this dissertation.

Besides my advisor, I would like to thank the rest of my dissertation committee: Dr. Rouzbeh Allahverdi, Dr. Akimasa Miyake, and Dr. Sanjay Reddy, for their insightful comments and encouragements.

Topics in the Physics of Supernovae and Neutron Stars

by

Sajad Abbar

B.S., Physics, Islamic Azad University, 2006

M.S., Physics, Sharif University of Technology, 2009

Ph.D., Physics, University of New Mexico, 2016

ABSTRACT

A star with a mass larger than 8 – 10 solar masses can end its life in a supernova explosion and possibly form a neutron star. In this dissertation, I study two important aspects of the physics of supernovae and neutron stars.

In the first part, I consider neutrino flavor oscillations in supernovae. Neutrino flavor oscillations in the presence of ambient neutrinos is nonlinear in nature which leads to interesting phenomenology that has not been well understood. This phenomenon in the supernova context has been studied in the so-called *neutrino Bulb model* which is a restricted, stationary supernova model and which possesses the (spatial) spherical symmetry about the center of the supernova and the (directional) axial symmetry around the radial direction.

By studying the problem of the neutrino oscillations in a two dimensional toy model, the so-called *neutrino Line model*, I show that the spatial symmetries can be broken spontaneously in a dense neutrino gas. Using a time-dependent version of

the neutrino Bulb model, I also show that the stationarity of a neutrino gas can be broken spontaneously as well.

In the second part, I compute the thermal conductivity of the neutron star crust. I use the quantum Monte Carlo (QMC) technique to calculate the static structure function $S(q)$ of a one-component ion lattice and use it to compute the thermal conductivity κ of high-density solid matter expected in the neutron star crust. By making detailed comparisons with the results obtained using one-phonon approximation (OPA), and the multi-phonon harmonic approximation, we assess the temperature regime where $S(q)$ from QMC can be used directly to calculate κ . We also compare the QMC results to those obtained using the classical Monte Carlo technique to quantitatively assess the magnitude of the quantum corrections. We show that the quantum effects become relevant at temperature $T \lesssim 0.3 \Omega_P$, where Ω_P is the ion plasma frequency. At $T \simeq 0.1 \Omega_P$ the quantum effects suppress κ by about 30%. The comparison with the results of the OPA indicates that dynamical information beyond the static structure is needed when $T \lesssim 0.1 \Omega_P$.

CONTENTS

LIST OF FIGURES	x
1 Introduction	1
1.1 Stellar evolution	1
1.2 Supernova neutrinos	3
1.3 Neutron star cooling	4
1.4 Outline of the dissertation	5
2 Supernova Explosion	7
2.1 Types of supernova	7
2.2 Core-collapse supernovae	9
2.3 Phases of core-collapse supernovae	11
2.4 Neutrino energy spectra	15
3 Physics of Neutrino Oscillations	18
3.1 Neutrino mixing	18

CONTENTS

3.2	Neutrino oscillations in vacuum	21
3.2.1	Three-flavor senario	21
3.2.2	Antineutrinos and CPT transformation	22
3.2.3	Two-flavor scenario	24
3.3	Neutrino oscillations in matter	25
3.3.1	The matter potential	25
3.3.2	The MSW effect	26
3.4	Collective neutrino oscillations in supernovae	29
3.4.1	Hamiltonian in a dense neutrino gas	30
3.4.2	Neutrino Bulb model	31
3.4.3	Simulation of neutrino oscillations in the Bulb model	33
3.4.4	Neutrino flavor isospin	35
4	Flavor Instabilities in the Neutrino Line Model	41
4.1	The neutrino Line model	42
4.1.1	Equations of motion	42
4.1.2	Collective modes in the linear regime	45
4.2	Results in the linear regime	48
4.2.1	Numerical results	48
4.2.2	Flavor instabilities and matter effect	52
4.3	Discussion	54

CONTENTS

5	Neutrino Flavor Instabilities in Time-Dependent Bulb Model	57
5.1	Time-dependent neutrino Bulb model	58
5.2	Linear regime	60
5.3	Results and discussion	63
6	Neutron Stars	66
6.1	Mass and radius of the neutron star	67
6.2	Cooling of the neutron star	73
7	Thermal Conductivity of the Neutron Star Crust	78
7.1	Thermal conductivity of the outer crust	79
7.2	Phonon spectrum and dynamical response	83
7.3	Static structure function and Monte Carlo simulations	88
7.4	Discussion	92
8	Summary and Outlook	96

LIST OF FIGURES

2.1	The classification scheme of supernovae.	8
2.2	Remnants of massive single stars as a function of initial metallicity and initial mass.	10
2.3	Schematic representation of the evolution stages of a core collapse supernova.	14
3.1	Schematic representation of the different mass hierarchies.	20
3.2	Scheme of the CPT, CP, and T transformations.	23
3.3	Effective mixing angle and the effective squared masses in matter as functions of the electron number density.	28
3.4	A schematic representation of the neutrino Bulb model.	32
3.5	Energy-averaged survival probabilities.	35
3.6	The energy spectra for neutrinos and antineutrinos.	36
3.7	The survival probabilities as functions of the neutrino energy and emission angle	37

LIST OF FIGURES

3.8	Comparison between numerical and semi-analytical solutions of neutrino oscillations in supernovae.	40
4.1	A schematic diagram of the two-dimensional (neutrino) Line model.	43
4.2	The evolution of the amplitudes of the off-diagonal elements of the neutrino moment matrices.	49
4.3	The amplitudes of the unstable modes of the m th neutrino moments.	50
4.4	The exponential growth rates $\kappa_m^{(i)}$ of the unstable collective modes .	52
4.5	Maximum exponential growth rate of the collective neutrino oscillation modes.	53
5.1	The geometric picture of the time-dependent (neutrino) Bulb model.	58
5.2	The maximum exponential growth rates κ^{\max} of a few Fourier modes with various frequencies.	63
6.1	Mass-radius curves for a verity of popular equations of state.	71
6.2	Schematic representation of the structure of a neutron star.	72
6.3	Schematic picture of the composition of the neutron star along the density axis.	73
7.1	The dispersion relations of the phonon modes of the Coulomb lattice.	84
7.2	The one-phonon approximation results of $S'_\kappa(q)$ and $S'(q)$	87
7.3	The inelastic part of static structure function $S'(q)$ of the LD matter at the two temperatures.	91

LIST OF FIGURES

7.4 Thermal conductivity of the matter as a function of temperature. . . 93

Chapter 1

Introduction

Supernovae and neutron stars are among the most interesting phenomena in the universe. Due to their extreme physical conditions, the understanding of supernovae and neutron stars involves many branches of physics such as nuclear physics, particle physics, general relativity, condensed matter physics and so on. This makes the physics of supernovae and neutron stars a vitrine of physics in which a large number of, if not all, categories of physics are displayed.

The study of supernovae and neutron stars enables us to probe the physics of matter at extreme densities and temperatures. Since studying the matter under such extreme conditions is very difficult (if not impossible) in the laboratory, supernovae and neutron stars can be considered as laboratories for physics in extreme conditions.

1.1 Stellar evolution

Astrophysicists have been trying to understand the lives of stars for many years. The main energy source of a star's luminosity is the nuclear fusion. Stars are born in giant molecular clouds consisted mostly of hydrogen. They first burn hydrogen to

Chapter 1. Introduction

helium¹ and then, depending on their masses, they continue to burn lighter elements into heavier elements (see, e.g., (Kippenhahn et al. 1990)).

For stars with masses larger than approximately 8 – 10 solar masses, they can go through all the stages of nuclear fusion until the core is composed of iron group nuclei. Since the iron is the most tightly bound nucleus, the fusion stops at this point. The star is supported against the gravity by the thermal pressure while it is still losing thermal energy due to radiation. When the fusion does not provide sufficient heat to support the weight of the stellar envelope, the gravitational pull can be balanced by the pressure of degenerate electron gas in the core. In this case, the core is stable only if its mass is smaller than a critical mass called the *Chandrasekhar mass* (Chandrasekhar 1934). If the mass of the core becomes larger than this critical mass, the stellar core becomes unstable and begins to collapse under its own gravity.

The collapse proceeds until the inner core reaches densities of order of nuclear density, the pressure of the degenerate nonrelativistic gas of nuclei halts the collapse, causes bounce of the core and generates a shock wave. The final result is a supernova explosion that can outshine the rest of the galaxy and can eject a few solar masses of stellar materials with a kinetic energy of about 10^{51} erg within a few seconds.

During the collapse, a huge amount of gravitational binding energy (of about 10^{53} erg) is released. Approximately 99% of this energy is in the form of neutrinos of all flavors. The rest of the energy goes into the kinetic energy of the ejecta ($\sim 1\%$) and the electromagnetic radiation ($\sim 0.01\%$) (Raffelt 1996).

¹If the giant molecular cloud is not massive enough, its core will not become sufficiently hot to burn hydrogen and it will become a brown dwarf (Kippenhahn et al. 1990).

1.2 Supernova neutrinos

Neutrinos are subatomic particles that participate only in the weak and gravitational interactions. These particles come in three flavors ν_e, ν_μ and ν_τ and with very small masses. As we will see in Chapter 3, since the weak-interaction and mass (propagation) eigenstates of the neutrino are not the same, neutrinos can oscillate from one flavor into another during propagation.

The physics of the oscillations of supernova neutrinos is not well understood. Studying the evolution of these neutrinos is very important in different aspects of supernova physics.

The primordial element abundances froze out when the universe consisted of about 75% H and 25% He by mass with a very small fraction of heavier elements. As we mentioned in the previous section, stars can produce heavier elements up to iron through nuclear fusion that occurs inside their cores. The elements heavier than iron must be produced somewhere else. It is thought that elements with $A > 70$ are mostly produced through the slow and fast neutron capture processes, also known as the s- and r-processes. Core-collapse supernovae are one of the most popular candidate sites in the universe for r-process nucleosynthesis.

Understanding neutrino flavor evolution is important to r-process nucleosynthesis. The reason is that the neutrino flavor transformation can substantially modify the r-process by changing the neutron-to-proton ratio. In particular, the oscillations between $\nu_e(\bar{\nu}_e)$ and $\nu_{\mu,\tau}(\bar{\nu}_{\mu,\tau})$ can modify the ν_e and $\bar{\nu}_e$ energy spectra which in turn can change the neutron-to-proton ratio through the processes



Understanding neutrino flavor evolution can also be important to the supernova

dynamics. As we will see in the next chapter, one of the most popular explosion mechanism is the *delayed explosion*. In this mechanism, the shock is first stalled and then revived by absorbing a small fraction of the energy of the neutrinos released in the supernova explosion. A possible swap of the energy spectra of the neutrinos of different flavors can change the absorption of the neutrino energy by the shock wave and, as a result, it can affect the dynamics of the explosion.

Finally, if we can observe a galactic supernova, we may be able to measure the supernova neutrino energy spectra. By comparing the theoretical predictions with the observations, we can obtain valuable information of the physics of supernovae.

1.3 Neutron star cooling

For a range of values of initial masses and metallicities of the progenitor star, a supernova explosion can lead to the formation of a neutron star. The idea of the existence of neutron stars was first proposed by Baade and Zwicky (1934) almost a year after the discovery of the neutron by Chadwick (1932). However, the first observational evidence only came almost 30 years later when the first pulsar was observed by Anthony Hewish and Jocelyn Bell in 1967 (Hewish et al. 1968). We now know that pulsars are highly magnetized rotating neutron stars that emit electromagnetic radiation along their magnetic axes.

Neutron stars are formed with extremely high internal temperatures (of about $T \geq 10^{11}\text{K}$) and cool down in a few hundred thousands of years. The evolution of the thermal content of a neutron star is directly related to the properties of the very dense matter inside it. Studying the evolution of the surface temperature of the neutron star can provide us with the valuable information of its interior, structure and composition. In particular, we can obtain the information about the temperature-sensitive properties of the neutron star interior such as transport coefficients, the

superfluidity of the matter inside the neutron star core, the crust structure and composition, and so on.

1.4 Outline of the dissertation

In this dissertation I study two important aspects of the physics of supernovae and neutron stars. In the first part of this dissertation, I examine the neutrino flavor oscillations in supernovae and in the second part, I discuss briefly the topic of the neutron star cooling.

The main goal in the first part of this dissertation is to investigate the stability of the spatial and time symmetries in a dense neutrino gas. In Chapters 2 and 3, I review briefly the physics of supernovae and neutrino oscillations. In Chapters 4 and 5, I show that the time and spatial symmetries can be broken spontaneously in a dense neutrino gas due to neutrino oscillations. This means that even if the neutrino gas is initially equipped with spatial and time symmetries, a very small asymmetric perturbation in space (time) can lead to the breaking of the spatial (time) symmetry during the evolution of neutrinos.

In the second part of this dissertation, I consider the problem of the neutron star cooling. The main focus will be on the thermal conductivity of the neutron star crust. I investigate the importance of the quantum effects in the crust thermal conductivity by using classical and quantum Monte Carlo techniques and a semi-analytical calculation called the one-phonon approximation. We show that the quantum effects become important at temperature $T \leq 0.3 \Omega_P$ and the lattice dynamical information (information of the lattice variation in time) is needed when $T \leq 0.1 \Omega_P$. Here Ω_P is the *plasma frequency* which is an energy scale in the plasma related to the density, mass and charge of the ions.

Chapter 1. Introduction

Throughout this dissertation we adopt the natural physical units with $\hbar = c = k_{\text{B}} = 1$.

Chapter 2

Supernova Explosion

A massive star with a mass larger than $8 - 10 M_{\odot}$ can undergo a supernova explosion in the last stage of its life. During a supernova explosion, a huge amount of (gravitational binding) energy (of about 3×10^{53} erg) is released. The vast majority of this energy is released in the form of neutrinos of all flavors.

In this chapter, we will study the physics of supernova explosion with an emphasis on supernova neutrinos. We will review briefly the different types of supernovae and the explosion mechanisms behind them. We will also discuss the physics of supernova neutrinos and their energy spectra.

2.1 Types of supernova

Due to their large luminosities, supernovae were noticed very early by ancient civilizations. Chinese astronomers were the first to record a supernova explosion and there are notes showing that the first recorded supernova explosion is SN 185 occurred in 185 AD. There are records of several other supernovae observed by Chinese, middle eastern and European astronomers.

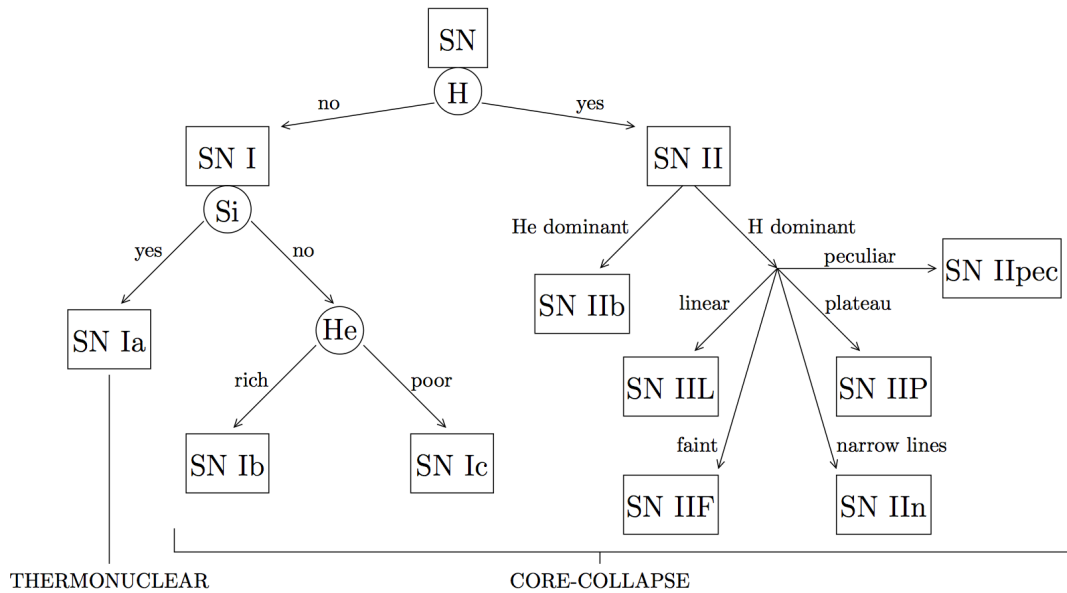


Figure 2.1: The classification scheme of supernovae. Figure adapted from (Giunti and Kim 2007).

The first modern classification of supernovae was proposed by American astronomers Rudolph Minkowski and Fritz Zwicky in 1941 (Da Silva 1993). Supernovae can be classified according to their spectroscopic properties (see Fig. 2.1). Based on the presence or absence of the hydrogen line in the spectrum, one can put a supernova in one of the two general categories. In the first category, called SN I, the hydrogen line is absent. This class itself is divided into several subclasses based on whether there exist Si or He lines in the spectra. On the other hand, if the H lines exist, the supernova belongs to the second category called SN II. Again this class can be divided into different subclasses based on other spectroscopic properties.

It turns out that the classification of supernovae based on their spectroscopic characteristics does not completely reflect the physics behind them. Supernovae can be classified in two general categories according to the mechanisms of their explosions.

Chapter 2. Supernova Explosion

The first category contains SN Ia which is conjectured to be the result of the explosion of a carbon-oxygen white dwarf that has a close companion star. White dwarfs are stellar remnants that are supported by the pressure of the degenerate gas of electrons. It can be shown that for such a configuration there exists a maximum mass, the so-called *Chandrasekhar mass*, above which the star is not stable (Chandrasekhar 1934). When the mass of the white dwarf exceeds the Chandrasekhar mass through accretion from the companion star, the degenerate electron gas can not balance the pull of gravity anymore. Even a very small fraction of excessive mass will trigger the collapse of the white dwarf. The collapse increases the pressure and the temperature which triggers the fusion of carbon and oxygen to heavier nuclei and leads to the release of a huge amount of energy. The amount of energy released is enough to explode the star and create an expanding nebula. The explosion of SN Ia blows the star completely apart and does not leave a central compact object.

The second class contains SN II, Ib, Ic that are thought to be generated by an explosion due to the core-collapse of the progenitor star. In the next section, we will discuss briefly the physics of the core-collapse supernovae.

2.2 Core-collapse supernovae

As mentioned above, SN II, SN Ib and SN Ic are produced by the core-collapse of massive stars. If the mass of the star is larger than $\sim 10M_{\odot}$, the core of the star can become sufficiently hot to go through all the stages of the nuclear fusion until Fe group nuclei become the dominant type of nuclei in the stellar core. As Fe is the most tightly bound nucleus, the fusion ceases after this stage. For the stars with masses smaller than $10M_{\odot}$, the core does not become hot enough to go through all the stages of the nuclear fusion. In particular, the cores of stars with masses in the range $8 - 10 M_{\odot}$ consist mostly of O, Ne and Mg.

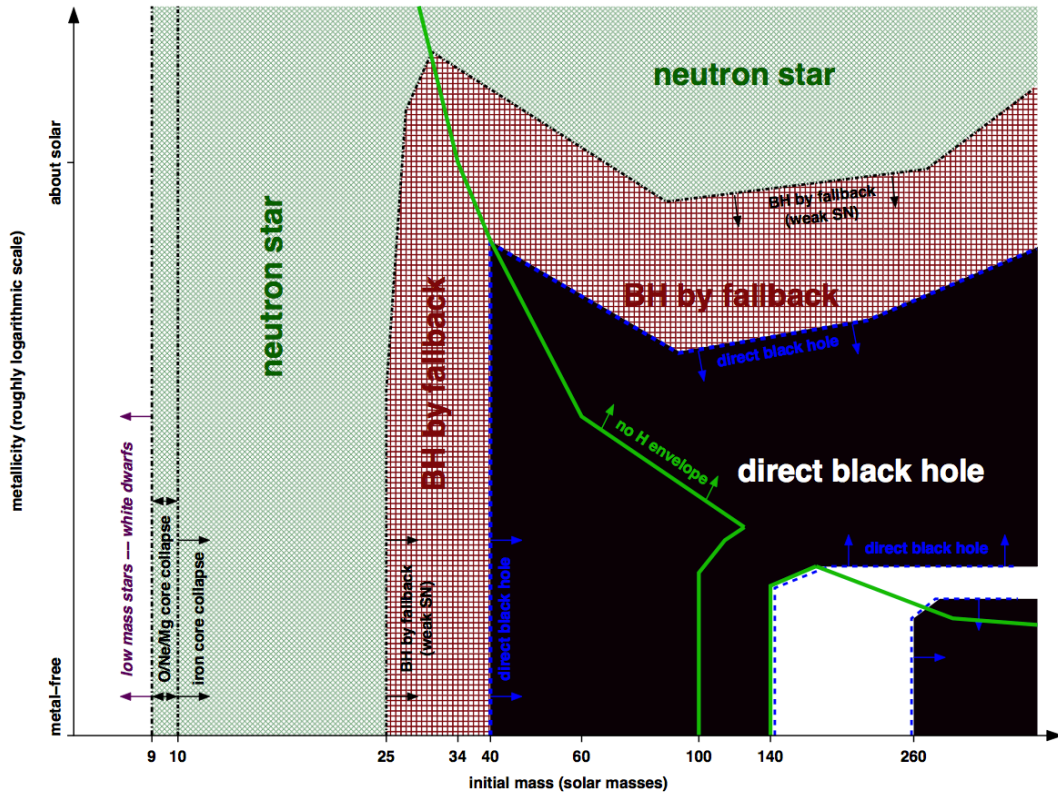


Figure 2.2: Remnants of massive single stars as a function of initial metallicity (y-axis; qualitatively) and initial mass (x-axis). The green curve determines the boundaries of the regions in which the star maintains and loses its H envelope. The white region is the region of pair-instability supernovae that leave no remnant. Figure adapted from (Heger et al. 2003) and reproduced by permission of the AAS.

At the end of the life of a massive star and just before the core-collapse, the stellar core has a mass of about $1.5 M_{\odot}$, a temperature of about 0.69 MeV, a central density of about $10^{10} \text{ g cm}^{-3}$ and a radius of about a few thousand kilometers. This configuration is supported against the pull of gravity by the pressure of the degenerate electron gas inside the core. Although the pressure is dominated by the degenerate electron gas, the contribution from the thermal pressure can not be neglected. When the collapse starts, the slightly higher temperature caused by the contraction of the

core leads to the photodissociation of Fe



This process consumes about 124 MeV of the thermal energy (per Fe nucleus) and therefore the thermal pressure is reduced even more rapidly. Beside this, free electrons will combine with nuclei in the inverse-beta-decay processes



which results in the reduction of the electron number density. Through these processes, both of the degenerate and thermal pressures diminish after the onset of the collapse and the collapse proceeds even faster.

During the collapse, the photon opacity inside the core is so large that neutrinos are essentially the only particles that can carry the energy out of the collapsing core. The total amount of the released energy is simply equal to the gravitational binding energy of the newly born central object (if any)

$$E_b \simeq \frac{3}{5} \frac{GM^2}{R} = 1.60 \times 10^{53} \text{ erg} \left(\frac{M}{M_\odot} \right)^2 \left(\frac{10 \text{ km}}{R} \right). \quad (2.3)$$

The total energy is equipartitioned among all the flavors of neutrinos and antineutrinos. This means that the total energy released in each type of neutrino is approximately $E_b/6$.

2.3 Phases of core-collapse supernovae

At the onset of the collapse, the neutrinos produced in the inverse-beta decay processes (Eq. (2.2)) can leave the core freely since the density inside the core is not sufficiently large to hinder their propagation. However, after a few milliseconds the

Chapter 2. Supernova Explosion

core density becomes large enough ($\rho \simeq 3 \times 10^{11} \text{ g cm}^{-3}$) to trap the neutrinos. This results in the formation of the *neutrino sphere* within which the neutrino mean free path λ is smaller than the radius of the neutrino sphere R_ν . This is the *capture phase* in a core-collapse supernova.

During the collapse, the core can be divided into two parts. The inner core collapses with a subsonic velocity. As a consequence, it can efficiently communicate within itself and collapses homologously. The subsonic velocity v inside the inner core is proportional to radius r :

$$\frac{v}{r} = 400 - 700 \text{ s}^{-1}. \quad (2.4)$$

In contrast, the outer core collapses almost freely with supersonic velocity.

After about a few hundred milliseconds, the matter inside the inner core reaches the nuclear density $\rho \simeq 10^{14} \text{ g cm}^{-3}$. At this point, the pressure of the degenerate gas of nonrelativistic nuclei halts and rebounds the collapse. The rebound results in the formation of an outward propagating shock wave at the edge of the inner core. This phenomenon is called the *core bounce*.

The initial velocity of the shock is very large with a value of about 100 km ms^{-1} . But as the shock travels through the infalling matter, it loses a large part of its energy through the processes discussed in the previous section (Eqs. (2.1) and (2.2)). As a consequence, a large number of electron neutrinos are produced at this stage. These neutrinos initially pile up behind the shock wave since the matter density is very large and the shock wave is well inside the neutrino sphere. However, a few tens of milliseconds after the bounce, the shock wave reaches the region with densities of order $10^{11} \text{ g cm}^{-3}$. At this point the matter becomes transparent to neutrinos and they can propagate freely. As a result, in a short interval of time (a few milliseconds), a large number of neutrinos are released. This is the *neutronization burst*, *electron neutrino burst* or *breakout pulse*. The neutrino luminosity is very large in the neutralization

Chapter 2. Supernova Explosion

burst $L_\nu \sim 6 \times 10^{51} \text{ erg s}^{-1}$. The burst lasts for a few milliseconds during which a total energy of a few 10^{51} erg is released.

The energy of the shock is finally exhausted, and it stalls at a radius of about 200 – 300 km. During the time when the shock stalls, the matter outside the shock keeps falling through it. This phase is the *accretion phase* which lasts for about a few hundred milliseconds. During the accretion phase, the matter behind the shock is heated by the accretion and produces neutrinos and antineutrinos of all flavors. Almost a quarter of the binding energy is released during this phase.

If there does not exist a mechanism to revive the shock, the explosion will cease at this point. It has been suggested that the thermal neutrinos coming from the deeper regions of the core could revive the shock in a mechanism called the *delayed explosion* (Burrows et al. 1995). The mechanism is based on the absorption of a fraction of the energy of neutrinos by the matter just below the shock. Most of the energy is deposited by electron neutrinos and electron antineutrinos since they can be absorbed by free nucleons just below the shock



It has been shown that the convection plays an essential role in the delayed supernova scenario. It can transport the hotter matter from innermost regions to the region just below the shock. For this reason many of one dimensional supernova simulations that do not include convection do not produce a successful supernova explosion.

What could be left behind a supernova explosion is the proto-neutron star which settles down in a few seconds and can form a neutron star or a black hole. After the accretion phase, the proto-neutron star continues to emit thermal neutrinos and anti-neutrinos of all flavors for a few seconds. This phase is called the *Kelvin-Helmholtz*

Chapter 2. Supernova Explosion

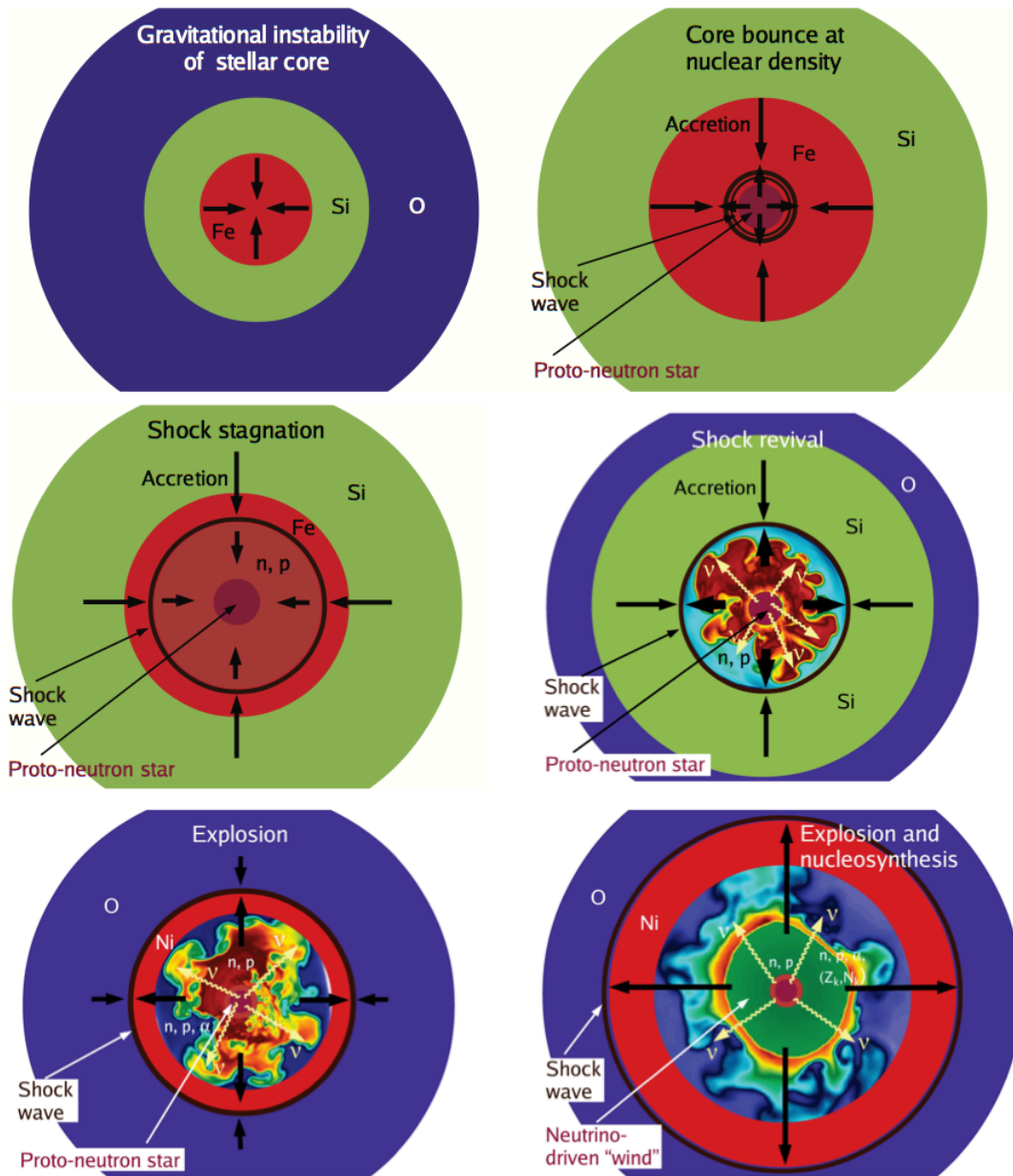


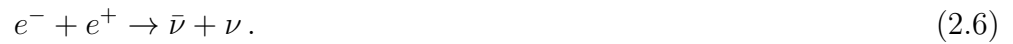
Figure 2.3: Schematic representation of the evolution stages of a core collapse supernova. The onset of the collapse is displayed in the top left panel and the last stage of explosion is displayed on bottom right. Figure adapted from (Janka et al. 2012).

cooling phase or simply the *cooling phase*. In Fig. 2.3, different stages of the supernova explosion are shown schematically.

2.4 Neutrino energy spectra

In the very hot core, neutrinos are produced through the following reactions:

- pair annihilation



- electron(positron)-nucleon bremsstrahlung



- nucleon-nucleon bremsstrahlung



- plasmon decay



- photoannihilation



- e^+ capture processes



Chapter 2. Supernova Explosion

These neutrinos are initially trapped inside the neutrino sphere due to neutral-current weak scattering by large nuclei such scattering processes are very effective since the scattering amplitudes of individual nucleons inside a large nucleus add up coherently. The cross section of the neutrino scattering on a large nucleus is proportional to the neutrino energy squared

$$\sigma \approx G_F^2 E_\nu^2. \quad (2.12)$$

From this equation, one observes that the neutrino sphere is a function of the neutrino energy and not a well-defined single surface.

One should note that the scattering on large nuclei does not change the neutrino energy by large amounts. In fact, the energies of the neutrinos are set inside the *energy sphere* where the neutrino energy was last modified due to processes such as scattering on electrons, pair production and charged-current absorption. This surface resides inside the neutrino sphere. To find the neutrino spectra on the surface of the neutrino sphere, one needs to track the neutrino evolution between the *energy sphere* and the *neutrino sphere*.

Since neutrinos are not in thermal equilibrium in the region between the neutrino sphere and the energy sphere, one does not expect a perfect blackbody spectrum for neutrinos on the surface of the neutrino sphere. Instead, the neutrino spectra are pinched in the sense that both of the high- and low-energy ends are suppressed in comparison with a perfect Fermi-Dirac spectrum (Keil et al. 2003).

One can fit the energy distribution $f_\nu(E)$ obtained from the Monte Carlo integration of the Boltzmann equation by an empirical formula (Keil et al. 2003). There are two widely used empirical formulae for neutrino energy distribution on the surface of neutrino sphere. The first one is the Fermi-Dirac like energy distribution

$$f_\nu(E) \propto \frac{E_\nu^2}{e^{E_\nu/T_\nu - \eta_\nu} + 1}, \quad (2.13)$$

Chapter 2. Supernova Explosion

where the degeneracy parameter η has a typical value of 1 – 3 and in general can be different for different flavors. The other widely used empirical formula is

$$f_\nu(E) \propto \left(\frac{E_\nu}{\langle E_\nu \rangle} \right)^\beta e^{-(1+\beta)E_\nu/\langle E_\nu \rangle}, \quad (2.14)$$

where β is the *pinching parameter* that depends on the flavor under consideration and $\langle E_\nu \rangle$ is the average energy of neutrino. The typical values of β are found to be in the range of 2 – 5 (Keil et al. 2003).

Chapter 3

Physics of Neutrino Oscillations

Neutrino flavor transformation is a quantum mechanical phenomenon in which neutrinos of different flavors transform into each other during propagation. The possibility of neutrino flavor transformation or neutrino oscillations was first proposed by Pontecorve in 1957 ¹ (Pontecorvo 1957; 1958).

Neutrino flavor transformation was first confirmed in late 1990s by the Super-Kamiokande Observatory (Fukuda et al. 1998) and the Sudbury Neutrino Observatory (Cleveland et al. 1998) in the solar neutrino experiments. This discovery led to the 2015 physics Nobel prize for Dr. Takaaki Kajita from the Super-Kamiokande Observatory and Dr. Arthur McDonald from the Sudbury Neutrino Observatory.

3.1 Neutrino mixing

Neutrino flavor transformation implies that neutrinos are massive particles. Neutrinos are produced and detected in the weak interaction (flavor) states. However, the

¹The phenomenon proposed by Pontecorve was the oscillation between the neutrino and antineutrino analogous to $K^0 - \bar{K}^0$ oscillations.

Chapter 3. Physics of Neutrino Oscillations

propagation (mass) states of the neutrino, the eigenstates of the propagation Hamiltonian, are not the same as the weak interaction states. As a consequence, neutrinos can undergo flavor transformation while they propagate.

The weak interaction states, $|\nu_\alpha\rangle$ ($\alpha = e, \mu, \tau$), and the mass eigenstates of the neutrino, $|\nu_k\rangle$ ($k = 1, 2, 3$), are related by the Pontecorvo-Maki-Nakagawa-Sakata (PMNS) matrix

$$|\nu_\alpha\rangle = \sum_{k=1}^3 U_{\alpha k}^* |\nu_k\rangle, \quad (3.1)$$

where U is a 3×3 unitary matrix (Giunti and Kim 2007).

The PMNS matrix can be parametrized in terms of four parameters: three mixing angles θ_{12} , θ_{23} and θ_{13} and one phase δ ². The phase δ is nonzero only if there exists a violation of combined charge and parity symmetry or CP violation (see next section). With these parameters, the PMNS matrix can be written as

$$U = \begin{pmatrix} U_{e1} & U_{e2} & U_{e3} \\ U_{\mu 1} & U_{\mu 2} & U_{\mu 3} \\ U_{\tau 1} & U_{\tau 2} & U_{\tau 3} \end{pmatrix} \quad (3.2)$$

$$= \begin{pmatrix} c_{12}c_{13} & s_{12}c_{13} & s_{13}e^{-i\delta} \\ -s_{12}c_{23} - c_{12}s_{23}s_{13}e^{i\delta} & c_{12}c_{23} - s_{12}s_{23}s_{13}e^{i\delta} & s_{23}c_{13} \\ s_{12}s_{23} - c_{12}c_{23}s_{13}e^{i\delta} & -c_{12}s_{23} - s_{12}c_{23}s_{13}e^{i\delta} & c_{23}c_{13} \end{pmatrix},$$

where $c_{ij} \equiv \cos \theta_{ij}$ and $s_{ij} \equiv \sin \theta_{ij}$. The neutrino mass-squared differences, $\Delta m_{kj}^2 = m_k^2 - m_j^2$, and the mixing angles can be measured in various neutrino oscillation experiments. The best fit values of the mass-squared differences are (Olive et al.

² This is true only if neutrinos are Dirac particles. In the case of Majorana neutrinos, there are two additional phases. The Majorana phases do not affect neutrino oscillations.

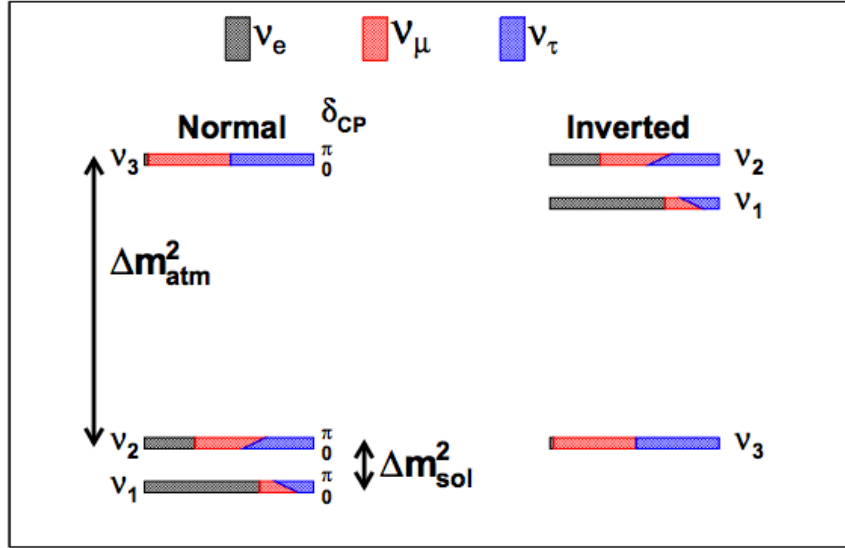


Figure 3.1: Schematic representation of the different mass hierarchies. Reprinted from *Prog. Part. Nucl. Phys.*, 83, X. Qian & P. Vogel, *Neutrino mass hierarchy*, 1 Copyright 2015, with permission from Elsevier (Ref. (Qian and Vogel 2015)).

2014)

$$\begin{aligned} \Delta m_{21}^2 &\simeq 7.6 \times 10^{-5} \text{eV}^2, \\ |\Delta m_{13}^2| &\simeq |\Delta m_{23}^2| \simeq 2.4 \times 10^{-3} \text{eV}^2, \end{aligned} \quad (3.3)$$

and for the $\sin 2\theta_{ij}$'s are

$$\begin{aligned} \sin^2 2\theta_{12} &= 0.846 \pm 0.021, \\ \sin^2 2\theta_{23} &= 0.999_{-0.018}^{+0.001} \text{ normal hierarchy} \\ &= 1.000_{-0.017}^{+0.000} \text{ inverted hierarchy}, \\ \sin^2 2\theta_{13} &= 0.085 \pm 0.005, \end{aligned} \quad (3.4)$$

where $m_3 > m_2 > m_1$ for the normal hierarchy, and $m_2 > m_1 > m_3$ for the inverted hierarchy (see Fig. 3.1).

The resulting PMNS matrix is

$$U = \begin{pmatrix} 0.82 \pm 0.01 & 0.54 \pm 0.02 & 0.15 \pm 0.03 \\ 0.35 \pm 0.06 & 0.70 \pm 0.06 & 0.62 \pm 0.06 \\ 0.44 \pm 0.06 & 0.45 \pm 0.06 & 0.77 \pm 0.06 \end{pmatrix}. \quad (3.5)$$

3.2 Neutrino oscillations in vacuum

3.2.1 Three-flavor scenario

Since the mass eigenstates $|\nu_k\rangle$ are the eigenstates of the propagation Hamiltonian in vacuum, their evolution in time and space can be written as

$$|\nu_k(\vec{x}, t)\rangle = e^{-iE_k t + i\vec{p}_k \cdot \vec{x}} |\nu_k\rangle,$$

where E_k and \vec{p}_k are the energy and momentum of the k^{th} mass eigenstate. Using Eq. (3.1), one finds the evolved flavor states to be

$$|\nu_\alpha(\vec{x}, t)\rangle = \sum_k U_{\alpha k}^* e^{-iE_k t + i\vec{p}_k \cdot \vec{x}} |\nu_k\rangle. \quad (3.6)$$

Now we can write $|\nu_k\rangle$ in terms of $|\nu_\alpha\rangle$ and obtain

$$|\nu_\alpha(\vec{x}, t)\rangle = \sum_{k,\beta} U_{\alpha k}^* e^{-iE_k t + i\vec{p}_k \cdot \vec{x}} U_{\beta k} |\nu_\beta\rangle. \quad (3.7)$$

Therefore $\nu_\alpha \rightarrow \nu_\beta$ transition amplitude can be written as

$$A_{\nu_\alpha \rightarrow \nu_\beta} = \langle \nu_\beta | \nu_\alpha(\vec{x}, t) \rangle = \sum_k U_{\alpha k}^* e^{-iE_k t + i\vec{p}_k \cdot \vec{x}} U_{\beta k}. \quad (3.8)$$

Assuming that the different mass eigenstates have the same momentum and that the neutrinos are traveling with the speed of light to a good approximation, the transition probability is

$$P_{\nu_\alpha \rightarrow \nu_\beta}(L) = |A_{\nu_\alpha \rightarrow \nu_\beta}(L)|^2 = \sum_{k,j} U_{\alpha k}^* U_{\beta k} U_{\beta j}^* U_{\alpha j} e^{-i(E_k - E_j)L} \quad (3.9)$$

after traveling a distance of $L \simeq t$. In the case of ultrarelativistic neutrinos, the energy of the neutrino can be written as

$$E_k = \sqrt{p_k^2 + m_k^2} \simeq p_k + \frac{m_k^2}{2E_k}. \quad (3.10)$$

Substituting this result in Eq. (3.9), we get

$$P_{\nu_\alpha \rightarrow \nu_\beta}(L) = \langle \nu_\beta | \nu_\alpha(\vec{x}, t) \rangle = \sum_{k,j} U_{\alpha k}^* U_{\beta k} U_{\beta j}^* U_{\alpha j} \exp \left[-i \frac{\Delta m_{kj}^2}{2E} L \right]. \quad (3.11)$$

One can immediately observe that the oscillation wavelengths are

$$\lambda_{kj} = \frac{4\pi E}{|\Delta m_{kj}^2|}. \quad (3.12)$$

Eq. (3.11) tells us that the experiments based on vacuum neutrino oscillations are sensitive only to the absolute values of mass-squared differences. Since there are three neutrino masses, there exist two independent mass-squared differences. The solar neutrino mass-squared difference $\Delta m_{\odot}^2 \simeq \Delta m_{12}^2 \simeq 7.6 \times 10^{-5} \text{ eV}^2$ is measured by the solar and reactor neutrino experiments. For solar neutrinos, it is known that $m_2^2 > m_1^2$ due to the presence of the matter effect (see the next section). The other mass-squared difference is measured in the atmospheric and long-baseline neutrino experiments and has a value $\Delta m_{\text{atm}}^2 \simeq |\Delta m_{13}^2| \simeq |\Delta m_{23}^2| \simeq 2.4 \times 10^{-3} \text{ eV}^2$. For the atmospheric neutrinos, the sign of the mass-squared difference is not known, and therefore there exist two hierarchies as discussed in the previous section.

3.2.2 Antineutrinos and CPT transformation

The PMNS matrix for the antineutrino is related to the one for the neutrino by noting that the neutrino becomes the antineutrino under the combined charge (C) and parity (P) transformation. In fact a P transformation takes a left-handed state to a right-handed one, and a C transformation makes particle its antiparticle. By

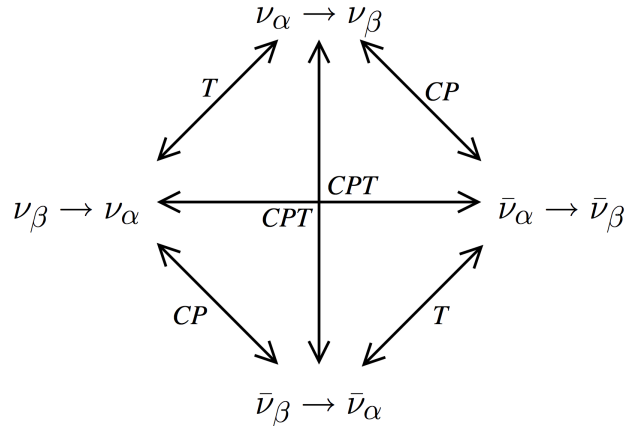


Figure 3.2: Scheme of the CPT, CP, and T transformations. Figure adapted from (Giunti and Kim 2007).

applying the CP transformation to the both sides of Eq. (3.1), we get (Peskin and Schroeder 1995)

$$CP|\nu_\alpha\rangle = |\bar{\nu}_\alpha\rangle = CP\left(\sum_k U_{\alpha k}^*|\nu_k\rangle\right) = \sum_k U_{\alpha k}|\bar{\nu}_k\rangle. \quad (3.13)$$

Therefore all the equations we found for neutrinos in the previous section can be used for antineutrinos by replacing U with U^* . It should be noted that the CP violation occurs if there is a channel in which the transition probabilities are different for neutrinos and antineutrinos

$$P_{\nu_\alpha \rightarrow \nu_\beta} \neq P_{\bar{\nu}_\alpha \rightarrow \bar{\nu}_\beta}. \quad (3.14)$$

This occurs if $\delta_{CP} \neq 0$.

Since the CP transformation changes the neutrino to the antineutrino and the T transformation switches initial and final states (see Fig. 3.2), the CPT symmetry implies that

$$P_{\nu_\alpha \rightarrow \nu_\beta} = P_{\bar{\nu}_\beta \rightarrow \bar{\nu}_\alpha}. \quad (3.15)$$

3.2.3 Two-flavor scenario

For many cases, we can simplify the problem of neutrino oscillations into an effective two-flavor scenario. The physical justification behind this can be understood by noting that the mass-squared differences differ by more than an order of magnitude ($|\Delta m_{31}^2| \simeq 30 \times \Delta m_{21}^2$), and most of the neutrino oscillation experiments are sensitive to only one of the mass-squared differences. In this case, it can be shown that the problem of neutrino oscillations in the three-flavor scenario reduces to an effective two-flavor scenario with an effective mixing angle which is a function of the parameters in the three-flavor scenario (Giunti and Kim 2007).

In the two-flavor mixing scenario, there is only one mixing angle and the transformation matrix can be written as

$$U = \begin{pmatrix} \cos \theta & \sin \theta \\ -\sin \theta & \cos \theta \end{pmatrix}, \quad (3.16)$$

where θ is the effective vacuum mixing angle with a value in the range $0 \leq \theta \leq \pi/4$.

The flavor transition probability $\nu_\alpha \rightarrow \nu_\beta$ can be easily obtained from an equation similar to Eq. (3.11)

$$P_{\nu_\alpha \rightarrow \nu_\beta}(L) = \sin^2 2\theta \sin^2 \left[\frac{\Delta m^2 L}{4E} \right] = \sin^2 2\theta \sin^2 \left[1.27 \left(\frac{\Delta m^2}{1 \text{ eV}^2} \right) \left(\frac{L}{1 \text{ m}} \right) \left(\frac{1 \text{ MeV}}{E} \right) \right], \quad (3.17)$$

where the mass squared difference is defined to be $\Delta m^2 = m_2^2 - m_1^2$. For the survival probability we have

$$P_{\nu_\alpha \rightarrow \nu_\alpha}(L) = 1 - P_{\nu_\alpha \rightarrow \nu_\beta}(L) = 1 - \sin^2 2\theta \sin^2 \left(\frac{\Delta m^2 L}{4E} \right). \quad (3.18)$$

One should note that since $U = U^*$ in the two-flavor scenario, there is no CP violation. This tells us that there is no difference between the transition or survival probabilities of the neutrino and the antineutrino in the two flavor scenario.

From Eq. (3.17) one immediately notes that the oscillatory behavior can be observed only when

$$\frac{\Delta m^2 L}{4E} \sim 1. \quad (3.19)$$

In the case that $\Delta m^2 L/4E \ll 1$ there is no significant flavor conversion, and when $\Delta m^2 L/4E \gg 1$, the oscillation gets washed out by averaging the Eq. (3.17):

$$\langle P_{\nu_\alpha \rightarrow \nu_\beta}(L) \rangle = \frac{1}{2} \sin^2 2\theta. \quad (3.20)$$

3.3 Neutrino oscillations in matter

In this section, we study the neutrino evolution in matter in the two-flavor scenario. When neutrinos travel in matter, they experience a potential due to the coherent forward elastic scattering with the electrons, protons, neutrons and other particles in the medium. This leads to an additional term in the Hamiltonian that can make the problem of neutrino oscillations in matter very rich.

3.3.1 The matter potential

Neutrinos can interact through both charged-current and neutral-current weak interactions. The charged current interaction exists only for electron neutrinos and antineutrinos if we assume that there is no τ or μ in the medium (which is a valid assumption in most of the problems of interest) and that the energy of the neutrino is not enough to produce τ or μ . The charged current potential can be written as (Giunti and Kim 2007)

$$V_{CC} = \sqrt{2}G_F n_e, \quad (3.21)$$

Chapter 3. Physics of Neutrino Oscillations

where n_e is the electron number density. On the other hand, the neutral-current potential is felt equally by neutrinos of all flavors (Giunti and Kim 2007)

$$V_{\text{NC}} = -\frac{1}{2}\sqrt{2}G_{\text{F}}n_n, \quad (3.22)$$

where n_n is the neutron number density. Here it has been assumed that the medium consists of electrons, protons and neutrons and $n_e = n_p$ so that the neutral-current contribution from electrons and protons cancel each other. It should be noted that since V_{NC} is the same for all flavors, it contributes only to a common phase of the neutrino and does not affect neutrino oscillations.

The evolution of neutrino flavor is governed by the Schrödinger equation

$$i\frac{d}{dt}\Psi = H_{\text{eff}}\Psi. \quad (3.23)$$

Here

$$\Psi = \begin{pmatrix} \psi_{\nu_e} \\ \psi_{\nu_x} \end{pmatrix} \quad (3.24)$$

is the neutrino wave function where ψ_{ν_e} and ψ_{ν_x} are the amplitudes of the neutrino in the electron and muon/tau flavor states, respectively, and

$$H_{\text{eff}} = \frac{1}{2} \begin{pmatrix} -\omega \cos 2\theta + V_{\text{CC}} & \omega \sin 2\theta \\ \omega \sin 2\theta & \omega \cos 2\theta - V_{\text{CC}} \end{pmatrix} \quad (3.25)$$

is the effective Hamiltonian where

$$\omega = \frac{\Delta m^2}{2E} \quad (3.26)$$

is the vacuum oscillation frequency.

3.3.2 The MSW effect

The new term in the Hamiltonian due to the presence of matter can lead to a very interesting phenomenon called the Mikheyev-Smirnov-Wolfenstein (MSW) effect. In

Chapter 3. *Physics of Neutrino Oscillations*

this phenomenon, significant neutrino flavor conversion can occur in the neutrino gas.

It is convenient to define the new set of parameters

$$\omega_M = \sqrt{(\omega \cos 2\theta - V_{CC})^2 + (\omega \sin 2\theta)^2}, \quad (3.27)$$

and

$$\tan 2\theta_M = \frac{\tan 2\theta}{1 - \frac{V_{CC}}{\omega \cos 2\theta}}. \quad (3.28)$$

Using this new parametrization, the effective Hamiltonian in matter can be written as

$$H_{\text{eff}} = \frac{1}{2} \begin{pmatrix} -\omega_M \cos 2\theta_M & \omega_M \sin 2\theta_M \\ \omega_M \sin 2\theta_M & \omega_M \cos 2\theta_M \end{pmatrix}. \quad (3.29)$$

Obviously, ω_M and θ_M can be interpreted as the effective oscillation frequency and effective mixing angle of the neutrino in matter, respectively. One can define the neutrino wave function in the matter basis

$$\Phi = U_M^{-1} \Psi = \begin{pmatrix} \cos \theta_M & -\sin \theta_M \\ \sin \theta_M & \cos \theta_M \end{pmatrix} \Psi. \quad (3.30)$$

In the matter basis, the Hamiltonian is diagonalized

$$H_M = U_M^{-1} H_{\text{eff}} U_M = \frac{1}{2} \begin{pmatrix} -\omega_M & 0 \\ 0 & \omega_M \end{pmatrix}. \quad (3.31)$$

By observing Eqs. (3.29) and (3.28) one can see that there can be a resonance in which there can be significant flavor conversion when the mixing is maximum ($2\theta_M = \pi/2$). The electron density at the resonance is

$$n_e^{\text{res}} = \frac{\omega \cos 2\theta}{\sqrt{2}G_F}. \quad (3.32)$$

Chapter 3. Physics of Neutrino Oscillations

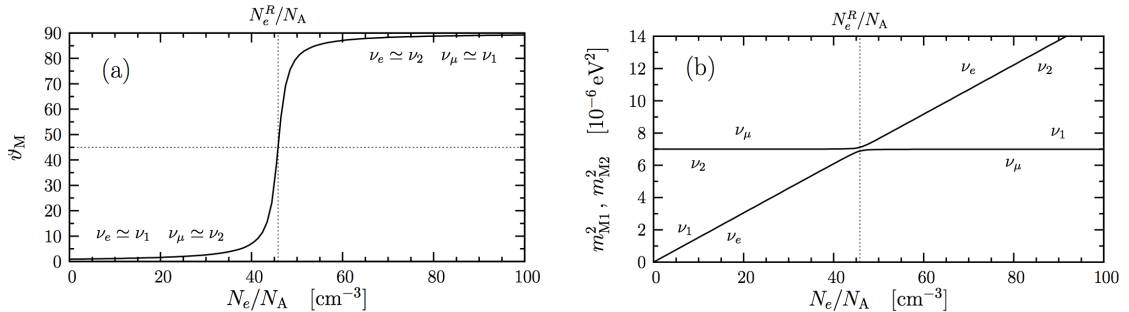


Figure 3.3: Effective mixing angle ϑ_M (a) and the effective squared-masses m_{M1}^2 , m_{M2}^2 (b) in matter as functions of the electron number density n_e divided by the Avogadro number N_A . Here it is assumed that $m_1 = 0$, $\Delta m^2 = 7 \times 10^{-6} \text{ eV}^2$, $\sin^2 2\theta = 10^{-3}$ and $E = 1 \text{ MeV}$. N_e^R is the electron density at resonance. Figure adapted from (Giunti and Kim 2007).

In the matter basis, the Equation of Motion (EoM) becomes

$$i \frac{d}{dt} \Phi = \frac{1}{2} \begin{pmatrix} -\omega_M & -2id\theta_M/dx \\ 2id\theta_M/dx & \omega_M \end{pmatrix} \Phi. \quad (3.33)$$

If the off-diagonal term in Eq. (3.33) is always small in comparison with the diagonal term, there is no significant mixing in the matter basis and the evolution is *adiabatic*. One can define the *adiabaticity parameter*

$$\gamma = \frac{\omega_M}{2|d\theta_M/dx|} \quad (3.34)$$

which determines the degree of the adiabaticity of the neutrino evolution. If $\gamma \gg 1$, the neutrino evolution is adiabatic and the transition between the two eigenstates in the matter basis is negligible.

To develop a better understanding of the MSW effect, let us consider the case in which an electron neutrino is produced in a region with a very large matter density. Eq. (3.28) implies that at large matter densities $\theta_M \simeq \pi/2$ and $\nu_e \simeq \nu_2^M$, where ν_2^M is the heavier mass state in the matter basis. If the matter density changes slowly,

the neutrino remains in ν_2^M in the matter basis during the propagation. However, at detection where the matter density is almost zero, Eq. (3.28) implies that $\nu_2^M \simeq \nu_x$ (for $\theta \ll 1$). This means that the electron neutrino has almost completely transformed into a μ/τ neutrino (see Fig. 3.3). This resonant behavior can explain the disappearance of a fraction of the electron neutrinos coming from the sun, which is known as *the solar neutrino problem* (Haxton 1995).

3.4 Collective neutrino oscillations in supernovae

In previous sections, we studied neutrino oscillations in vacuum and matter. In this section we consider neutrino oscillations in a dense neutrino gas in which the neutrino-neutrino interaction becomes significant. The presence of the neutrino-neutrino interaction makes the problem of neutrino oscillations in a dense neutrino gas highly coupled and nonlinear. Examples of such a medium can be found in supernovae, neutron star mergers and the early universe. Our main goal in this section is to study neutrino oscillations in supernovae.

In this section, as in the previous sections, we assume the two flavor scenario. This is justified by noting that ν_μ and ν_τ are maximally-mixed in vacuum ($\theta_{23} \simeq \pi/4$) and they experience similar weak interactions in supernovae. Moreover, one should note that since Δm_\odot^2 and Δm_{atm}^2 are separated by about two orders of magnitude, the oscillation phenomena are expected to be well separated for the two mass scales. Despite these justifications, since the problem is nonlinear, there is no guarantee that there will be no nontrivial effect from the three-flavor phenomenology. In particular, it has been argued that the results in the three-flavor scenario could be qualitatively different from the ones in the two-flavor scenario (Friedland 2010).

3.4.1 Hamiltonian in a dense neutrino gas

In a dense neutrino gas, there is a new term in the Hamiltonian due to the presence of the neutrino-neutrino interaction which is given by Qian and Fuller (1995)

$$H_{\nu\nu} = \sqrt{2}G_{\text{F}} \sum_{\alpha} \left[\int dn_{\nu_{\alpha}}(\mathbf{p}') \rho_{\nu_{\alpha}}(\mathbf{p}') (1 - \mathbf{v}' \cdot \mathbf{v}) - \int dn_{\bar{\nu}_{\alpha}}(\mathbf{p}') \rho_{\bar{\nu}_{\alpha}}^*(\mathbf{p}') (1 - \mathbf{v}' \cdot \mathbf{v}) \right]. \quad (3.35)$$

Here \mathbf{p} is the neutrino momentum, \mathbf{v} is the unit vector that determines the direction of the neutrino velocity, subscript ν_{α} ($\bar{\nu}_{\alpha}$) denotes the neutrino (antineutrino) initially produced in flavor α , dn is the differential neutrino number density, and ρ is the reduced density matrix

$$\rho = \frac{1}{2} \begin{pmatrix} |\psi_{\nu_e}|^2 - |\psi_{\nu_x}|^2 & 2\psi_{\nu_e}\psi_{\nu_x}^* \\ 2\psi_{\nu_e}^*\psi_{\nu_x} & -|\psi_{\nu_e}|^2 + |\psi_{\nu_x}|^2 \end{pmatrix}, \quad (3.36)$$

for neutrinos and

$$\rho = \frac{1}{2} \begin{pmatrix} |\psi_{\bar{\nu}_e}|^2 - |\psi_{\bar{\nu}_x}|^2 & 2\psi_{\bar{\nu}_e}\psi_{\bar{\nu}_x}^* \\ 2\psi_{\bar{\nu}_e}^*\psi_{\bar{\nu}_x} & -|\psi_{\bar{\nu}_e}|^2 + |\psi_{\bar{\nu}_x}|^2 \end{pmatrix}, \quad (3.37)$$

for antineutrinos.

One should note that $H_{\nu\nu}$ is quite different from the vacuum and matter Hamiltonian because in the sense that it couples neutrinos and antineutrinos with different energies and momenta. This means that one needs to track the evolution of all neutrinos and antineutrinos simultaneously. In addition, $H_{\nu\nu}$ depends on the neutrino wave function itself which makes the problem nonlinear and difficult to solve.

The total Hamiltonian in a dense neutrino gas is given by

$$H_{\text{eff}} = H_{\nu\nu} + \frac{1}{2} \begin{pmatrix} -\omega \cos 2\theta + V_{\text{CC}} & \omega \sin 2\theta \\ \omega \sin 2\theta & \omega \cos 2\theta - V_{\text{CC}} \end{pmatrix}, \quad (3.38)$$

for neutrinos, where $V_{\text{CC}} = \sqrt{2}G_{\text{F}}n_e$ is the matter potential, and

$$\omega = \frac{\Delta m^2}{2E}. \quad (3.39)$$

is the vacuum neutrino oscillation frequency.

For antineutrinos one needs to make the replacements $V_{CC} \rightarrow -V_{CC}$ and $H_{\nu\nu} \rightarrow -H_{\nu\nu}^*$. Moreover, the change of the neutrino mass hierarchy is obtained by taking $\Delta m^2 \rightarrow -\Delta m^2$.

3.4.2 Neutrino Bulb model

To study neutrino oscillations in supernovae, one has to solve a set of highly nonlinear and correlated differential equations

$$i \frac{d}{dx} \Psi_{\nu_\alpha}(\mathbf{p}) = H_{\text{eff}} \Psi_{\nu_\alpha}(\mathbf{p}) \quad (3.40)$$

with H_{eff} defined in Eq. (3.35).

The most general problem that needs to be solved is a seven dimensional problem, one dimension for time, three dimensions for space and three dimensions for the neutrino momentum. The complexity of the problem compels one to make some simplifications so that it can be solved more easily. To make the problem more tractable, a simplified model, the so-called *neutrino Bulb* model, has been extensively used in the field (Duan et al. 2006c; 2010). In this model, it is assumed that neutrinos are emitted isotropically and homogeneously from the surface of the spherical proto-neutron star. Furthermore, it is assumed that outside the proto-neutron star, the physical conditions depend only on the distance from the center of the proto-neutron star. In order to maintain the spherical symmetry, one also needs to assume the axial symmetry around the radial direction. This means that different neutrino beams with the same emission angle ϑ_0 (see Fig. 3.4) evolve identically. Finally, it is assumed that the neutrino emission and the physical conditions in the bulb model are time-independent. As illustrated in Fig. 3.4, different neutrino beams can be labeled by their emission angles ϑ_0 .

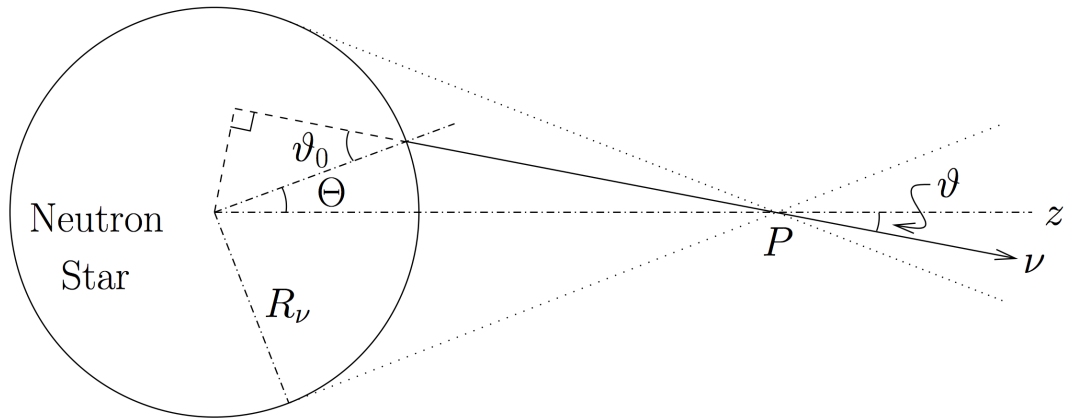


Figure 3.4: A schematic representation of the neutrino Bulb model. Here, the solid line is an arbitrary neutrino beam, ϑ is the angle between its propagation direction and the radial direction, and ϑ_0 is its emission angle on the surface of the proto-neutron star. Reprinted figure with permission from [H. Duan et al, Phys. Rev. D 74, 105014, 2006](#) (Ref. (Duan et al. 2006c)). Copyright 2006 by the American Physical Society.

In the neutrino Bulb model, the emission angle ϑ_0 on the surface of the proto-neutron star and the angle ϑ between the radial and the beam directions at the radius r is related by the following identity:

$$\sin \vartheta = \frac{R_\nu}{r} \sin \vartheta_0, \quad (3.41)$$

where R_ν is the radius of the neutrino sphere. One should note that the angle ϑ_0 is an intrinsic property of the neutrino beam.

In the neutrino Bulb model, the neutrino-neutrino interaction term in Eq. (3.35) can be written as (Duan et al. 2006c)

$$H_{\nu\nu} = \frac{\sqrt{2}G_F}{2\pi R_\nu^2} \sum_\alpha \int d(\cos \vartheta') dE' (1 - \cos \vartheta \cos \vartheta') \times \left[\frac{L_{\nu_\alpha}}{\langle E_{\nu_\alpha} \rangle} f_{\nu_\alpha}(E') \rho_{\nu_\alpha}(E', \vartheta') - \frac{L_{\bar{\nu}_\alpha}}{\langle E_{\bar{\nu}_\alpha} \rangle} f_{\bar{\nu}_\alpha}(E') \rho_{\bar{\nu}_\alpha}^*(E', \vartheta') \right]. \quad (3.42)$$

Here L_{ν_α} , $\langle E_{\nu_\alpha} \rangle$ and f_{ν_α} are the luminosity, the average energy and the energy

distribution function of the neutrino with flavor α on the surface of the proto-neutron star. The neutrino energy distribution function is normalized to one so that

$$\int_0^\infty dE' f_\nu(E') = 1. \quad (3.43)$$

A realistic form of $f_\nu(E)$ can be extracted from the supernova simulations. Two of the most popular forms of $f(E)$ are discussed in Section 2.5 and can be found in Eqs. (2.13) (the Fermi-Dirac distribution) and (2.14) (the power-law distribution). In what follows, we review the results obtained in Refs. (Duan et al. 2006a;c) where the Fermi-Dirac distribution function is used with $T_{\nu_e} = 2.76$ MeV, $T_{\bar{\nu}_e} = 4.01$ MeV, $T_{\nu_\mu} = T_{\bar{\nu}_\mu} = T_{\nu_\tau} = T_{\bar{\nu}_\tau} = 6.26$ MeV and $L_\nu = 10^{51}$ erg/s for all flavors. In addition, the baryon density is assumed to be

$$n_b = 4.2 \times 10^{30} \text{cm}^{-3} g_s \left(\frac{M_{\text{NS}}}{1.4 M_\odot} \right)^3 \left(\frac{100}{S} \right)^4 \left(\frac{10 \text{ km}}{r} \right) + n_{b0} \exp \left(- \frac{r - R_\nu}{h_{\text{NS}}} \right). \quad (3.44)$$

Here the total statistical weight of the relativistic particles, g_s , is taken to be 11/2, the entropy per baryon of the matter above the proto-neutron star, S , is assumed to be constant with the value of 140, the baryon density just above the proto-neutron star is $n_{b0} = 1.63 \times 10^{36} \text{cm}^{-3}$, and the scale height is $h_{\text{NS}} = 0.18$ km. One should note that, although the second term in the baryon density in Eq. (3.44) dominates near the proto-neutron star, it diminishes exponentially and becomes negligible at larger radii. The electron density $n_e = Y_e n_b$ can be obtained from the baryon density if the electron fraction Y_e is known.

3.4.3 Simulation of neutrino oscillations in the Bulb model

One can solve Eq. (3.40) numerically with the effective Hamiltonian given by Eq. (3.38). This means that one has to solve a large number of coupled nonlinear Schrödinger

equations simultaneously. Even for the Bulb model which is extremely simplified by the assumptions of the stationariness, and the spherical and axial symmetries, one has to solve $O(10^6)$ coupled nonlinear differential equations simultaneously.

Some of the results obtained in such simulations are presented in Figs. 3.5, 3.6 and 3.7. Fig. 3.5 shows the energy-averaged survival probabilities for ν_e and $\bar{\nu}_e$ in the normal and inverted hierarchies, respectively. The dotted line gives the average survival probabilities in the single-angle scenario in which it is assumed that the neutrino beams with different emission angles evolve exactly as the one propagating in the radial direction. The solid and dashed lines are for neutrino beams with emission angles $\vartheta_0 = 0, \pi/2$, respectively, in a multi-angle simulation. The results in Fig. 3.5 can not be simply explained only by the MSW mechanism. If the MSW was the only mechanism at work, one would expect the flavor conversion to occur only for the neutrinos (antineutrinos) if the neutrino mass hierarchy is normal (inverted).

Fig. 3.6 shows that the neutrino and antineutrino energy spectra in the normal and inverted hierarchies before and after the neutrino flavor conversion. As one can see, there are spectral swaps/splits in panels (a) and (c) where ν_e and ν_x almost swap their spectra in certain energy ranges. In Fig. 3.7, we show the neutrino and antineutrino survival probabilities in the normal and inverted hierarchies. We see that the energy spectra of ν_e and ν_x with energy below (above) $E \simeq 9$ MeV are almost completely swapped in the normal (inverted) hierarchy. The vertical fringes (the energy dependent features) are the results of the MSW flavor transformation which is energy dependent. The horizontal fringes (the angle-dependent features) are the result of the kinematic decoherence (Esteban-Pretel et al. 2007) originates from the fact that different neutrino beams travel different distances (from the surface of the proto-neutron star to the point at radius r).

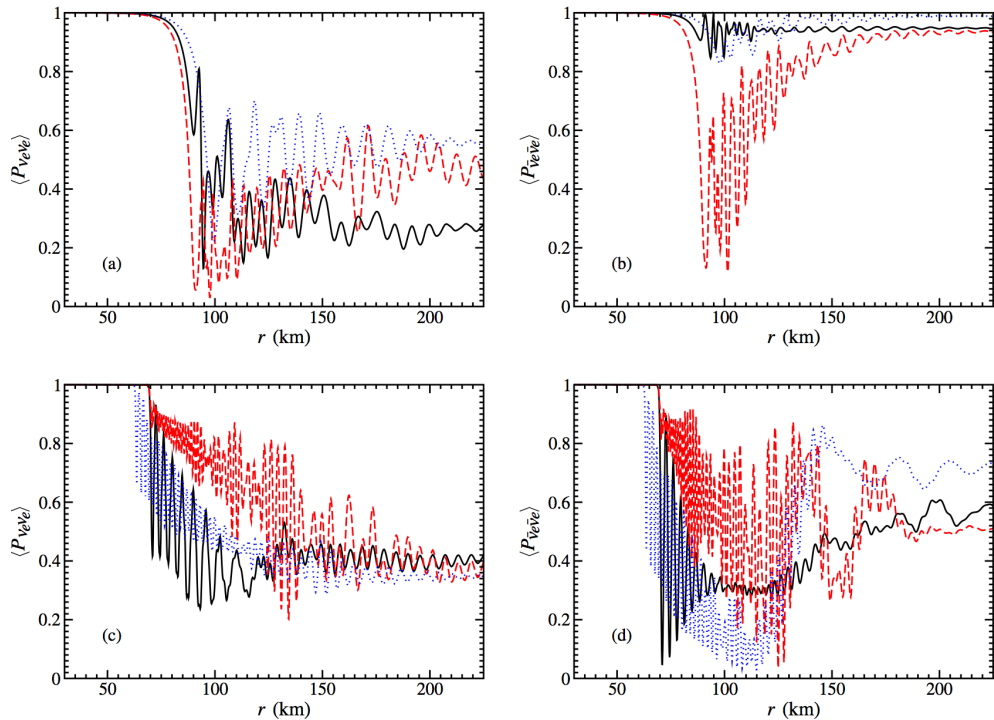


Figure 3.5: Energy-averaged survival probabilities for ν_e (left panels) and $\bar{\nu}_e$ (right panels) in the normal (upper panels) and inverted (lower panels) hierarchies. The solid (black) and dashed (red) lines are for neutrino beams with emission angles $\vartheta_0 = 0$ and $\pi/2$, respectively, in a multi-angle simulation. The dotted line (blue) is the energy-averaged survival probability in a single-angle simulation. Reprinted figure with permission from H. Duan et al, *Phys. Rev. Lett.* **97**, 241101, 2006 (Ref. (Duan et al. 2006a)). Copyright 2006 by the American Physical Society.

3.4.4 Neutrino flavor isospin

As discussed earlier, the results in Figs. 3.6 and 3.7 can not be simply explained by the MSW mechanism. In this section, we will try to develop an understanding of the spectral swaps/splits by studying the problem of neutrino oscillations in the *neutrino flavor isospin* (NFIS) picture, and we will see that spectral swaps/splits are the natural result of collective neutrino oscillations in the neutrino gas.

In the NFIS picture, the wave function can be represented by the NFIS vector

Chapter 3. Physics of Neutrino Oscillations

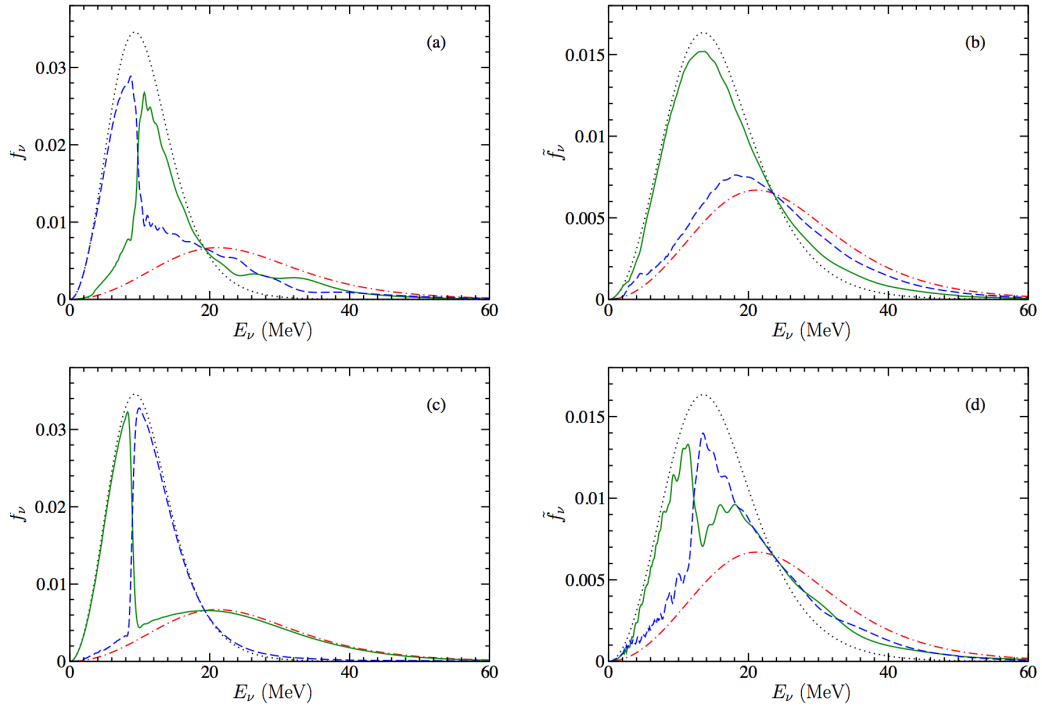


Figure 3.6: The energy spectra for ν_e (left panels) and $\bar{\nu}_e$ (right panels) in the normal (upper panels) and inverted (lower panels) hierarchies. The dotted and dot-dashed lines are the energy spectra of the neutrino (antineutrino) in electron and muon/tau flavors at $r = R_\nu$, respectively. The solid and dashed lines are the corresponding energy spectra at $r = 250$ km. Reprinted figure with permission from [H. Duan et al, Phys. Rev. D 74, 105014, 2006](#) (Ref. (Duan et al. 2006c)). Copyright 2006 by the American Physical Society.

which is defined by

$$\mathbf{s}_\nu \equiv \Psi_\nu^\dagger \frac{\boldsymbol{\sigma}}{2} \Psi_\nu = \frac{1}{2} \begin{pmatrix} 2 \operatorname{Re}(\psi_{\nu_e}^* \psi_{\nu_x}) \\ 2 \operatorname{Im}(\psi_{\nu_e}^* \psi_{\nu_x}) \\ |\psi_{\nu_e}|^2 - |\psi_{\nu_x}|^2 \end{pmatrix} \quad (3.45)$$

Chapter 3. Physics of Neutrino Oscillations

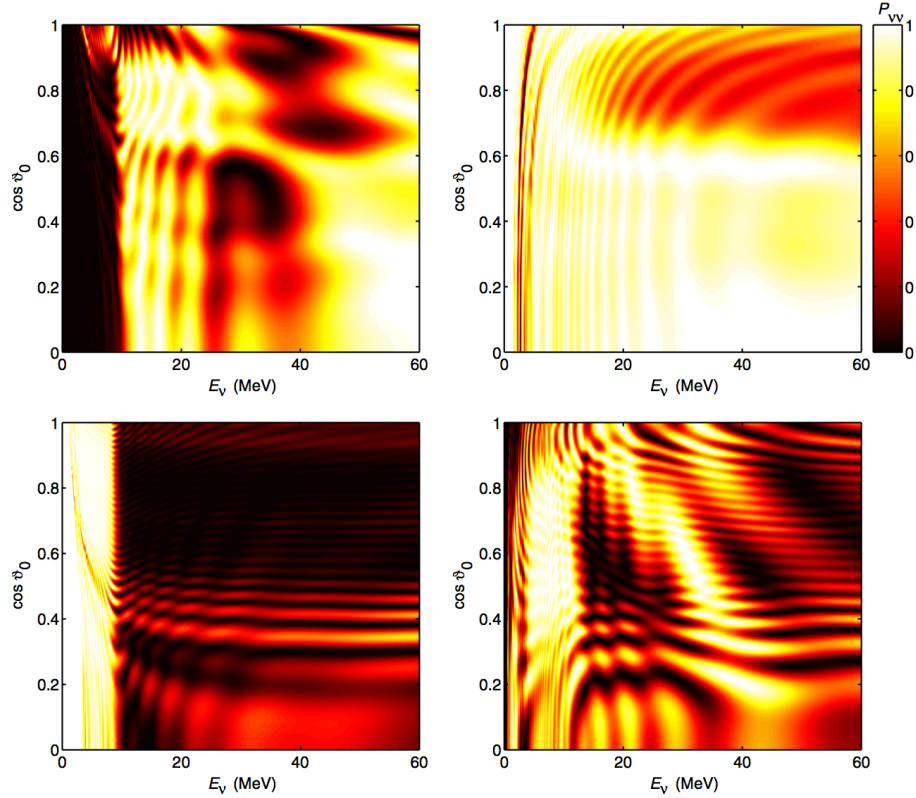


Figure 3.7: The survival probabilities as functions of the neutrino energy and emission angle ϑ_0 for ν_e (left panels) and $\bar{\nu}_e$ (right panels) in the normal (upper panels) and inverted (lower panels) hierarchies. Reprinted figure with permission from H. Duan et al, *Phys. Rev. Lett.* **97**, 241101, 2006 (Ref. (Duan et al. 2006a)). Copyright 2006 by the American Physical Society.

for the neutrino and

$$\mathbf{s}_{\bar{\nu}} \equiv (\sigma_2 \Psi_{\bar{\nu}})^\dagger \frac{\boldsymbol{\sigma}}{2} (\sigma_2 \Psi_{\bar{\nu}}) = -\frac{1}{2} \begin{pmatrix} 2 \operatorname{Re}(\psi_{\bar{\nu}_e} \psi_{\bar{\nu}_x}^*) \\ 2 \operatorname{Im}(\psi_{\bar{\nu}_e} \psi_{\bar{\nu}_x}^*) \\ |\psi_{\bar{\nu}_e}|^2 - |\psi_{\bar{\nu}_x}|^2 \end{pmatrix} \quad (3.46)$$

for the antineutrino. Here

$$\sigma_1 = \begin{pmatrix} 0 & 1 \\ 1 & 0 \end{pmatrix}, \quad \sigma_2 = \begin{pmatrix} 0 & -i \\ i & 0 \end{pmatrix}, \quad \sigma_3 = \begin{pmatrix} 1 & 0 \\ 0 & -1 \end{pmatrix} \quad (3.47)$$

Chapter 3. Physics of Neutrino Oscillations

are the Pauli matrices. Then the EoM can be written as

$$\frac{d\mathbf{s}_i}{dt} = \mathbf{s}_i \times \mathbf{H}_{\text{eff}}, \quad (3.48)$$

where the effective Hamiltonian vector is given by

$$\mathbf{H}_{\text{eff}} = \omega_i \mathbf{H}_{\text{vac}} + \mathbf{H}_e - 2\sqrt{2}G_{\text{F}} \sum_j n_j \mathbf{s}_j. \quad (3.49)$$

In this equation, $\mathbf{H}_e = -\sqrt{2}G_{\text{F}}n_e\mathbf{e}_3$ is the contribution due to the presence of the electron density with \mathbf{e}_3 being a unit vector, and \mathbf{H}_{vac} is the vacuum field defined by

$$\mathbf{H}_{\text{vac}} = -\mathbf{e}_1 \sin 2\theta + \mathbf{e}_3 \cos 2\theta, \quad (3.50)$$

where θ is the vacuum mixing angle. Here we use the convention in which $\theta < \pi/4$ for the normal hierarchy and $\theta > \pi/4$ for the inverted hierarchy. The vacuum neutrino oscillation frequency is given by

$$\omega_i = \pm \left| \frac{\Delta m^2}{2E_i} \right|, \quad (3.51)$$

where the $+$ ($-$) sign is for the neutrino (antineutrino).

It has been shown that the spectral swaps/splits are the common feature of both multi-angle and single-angle simulations (Duan et al. 2006c). Here, we focus on the neutrino oscillations in the single-angle model. The spectral swaps/splits observed in Figs. 3.6 and 3.7 can be explained by assuming that the NFIS vectors undergo a regular precession around the vacuum field \mathbf{H}_{vac} with a common frequency ω_{pr} (Duan et al. 2006c)

$$\frac{d\mathbf{s}_i}{dt} = \mathbf{s}_i \times \omega_{\text{pr}} \mathbf{H}_{\text{vac}}. \quad (3.52)$$

In the absence of matter, this equation combined with Eq. (3.48) results in

$$\mathbf{s}_i \times [(\omega_i - \omega_{\text{pr}})\mathbf{H}_{\text{vac}} + \mathbf{S}] = 0, \quad (3.53)$$

Chapter 3. Physics of Neutrino Oscillations

where $\mathbf{S} \equiv -2\sqrt{2}G_F \sum_i n_i \mathbf{s}_i$. This equation implies that during the regular precession, \mathbf{s}_i is either aligned or antialigned with the effective field \mathbf{F}_i defined by

$$\mathbf{F}_i = [(\omega_i - \omega_{\text{pr}})\mathbf{H}_{\text{vac}} + \mathbf{S}]. \quad (3.54)$$

If the neutrino number density varies very slowly, a NFIS vector initially aligned (antialigned) with \mathbf{F}_i , will always remain aligned (antialigned) with it. At large neutrino number densities, \mathbf{S} is the dominant term. Thus in the case that $\alpha = n_{\bar{\nu}_e}/n_{\nu_e} < 1$, electron neutrinos (antineutrinos) NFIS vectors are antialigned (aligned) with \mathbf{F}_i . During an adiabatic evolution and when neutrino number density is approximately zero, neutrinos (antineutrinos) NFIS vectors must be antialigned (aligned) with $\mathbf{F}_i = (\omega_i - \omega_{\text{pr}})\mathbf{H}_{\text{vac}}$. This implies that the neutrinos with energies below and above $\delta m^2/2\omega_{\text{pr}}$ behave differently in the adiabatic evolution. In particular, neutrinos with energy below (above) $\delta m^2/2\omega_{\text{pr}}$ are found to be antialigned (aligned) with \mathbf{H}_{vac} . In the case that the mixing angle is very small, i.e. $\theta \simeq 0$ for the normal hierarchy and $\theta \simeq \pi/2$ for the inverted hierarchy, $\mathbf{H}_{\text{vac}} \simeq \mathbf{e}_3$ ($\mathbf{H}_{\text{vac}} \simeq -\mathbf{e}_3$) for the normal (inverted) hierarchy. Therefore, the neutrinos with energies below (above) $\delta m^2/2\omega_{\text{pr}}$ in the normal (inverted) are completely converted to ν_x neutrinos. On the other hand, neutrinos with energy above (below) $\delta m^2/2\omega_{\text{pr}}$ in the normal (inverted) hierarchy experience almost no conversion.

In Fig. 3.8, we show the energy-averaged $\langle s_{\perp} \rangle$ and $\langle s_z \rangle$ (the component along \mathbf{e}_3) obtained from numerical simulations in the single-angle model as well as the regular precession and the MSW-like solutions ³.

³The MSW-like solution is the solution in which it is assumed that a neutrino initially in the light (heavy) mass eigenstate will stay in the same instantaneous mass eigenstate, and a NFIS initially aligned (anti-aligned) with its effective field will stay aligned (anti-aligned) with the effective field.

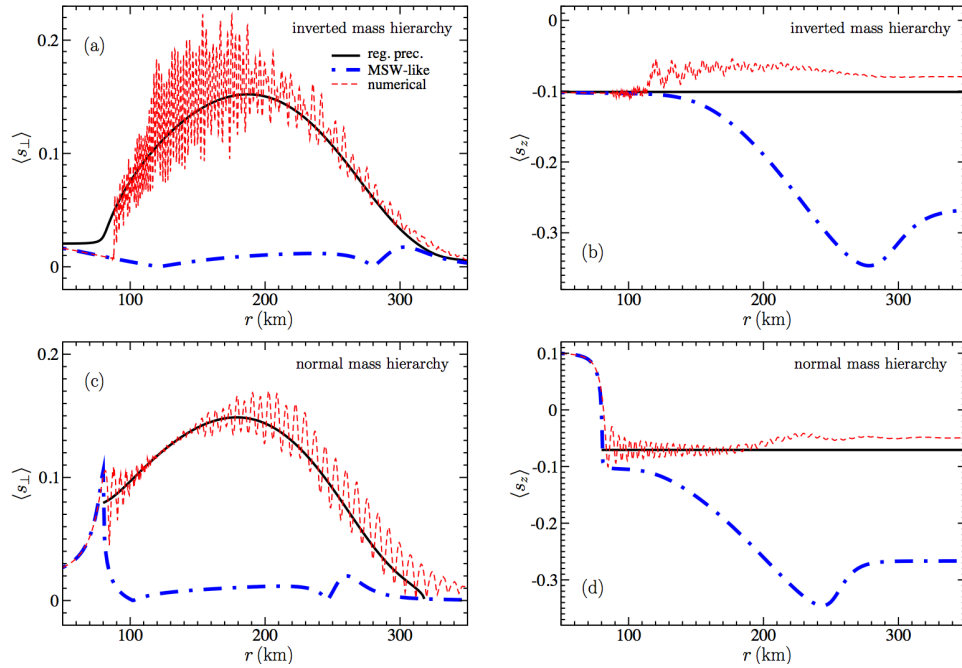


Figure 3.8: $\langle s_{\perp} \rangle$ (left panels) and $\langle s_z \rangle$ (right panels) in normal (upper panels) and inverted (lower panels) hierarchies. The solid (black) line is the regular precession solution, the thick (blue) dashed line shows the MSW-like solution and the thin (red) dashed line shows the results obtained from numerical simulations. Reprinted figure with permission from [H. Duan et al, Phys. Rev. D 76, 085013, 2007](#) (Ref. (Duan et al. 2007)). Copyright 2007 by the American Physical Society.

Chapter 4

Flavor Instabilities in the Neutrino Line Model

As discussed in the previous chapter, in order to make the problem of neutrino oscillations in supernovae more tractable, one has to make several simplifications. In particular, a simplified one-dimensional supernova model called the neutrino Bulb model has been widely used in the literature to study neutrino flavor evolution in supernovae (Duan et al. 2006c; 2010). Through the numerical simulations performed in the Bulb model, it was discovered that there were collective modes of neutrino oscillations in the dense neutrino gas above the proto-neutron star and that the neutrino flavor evolution can be dramatically different for the normal and inverted hierarchies inside supernovae (Duan et al. 2006b;c).

There are several effects that are not taken into account in the Bulb model, although they can modify neutrino oscillations significantly. For example, it was shown that the back-scattering of the neutrinos from the nucleons in the supernova envelope can lead to a significant modification of the neutrino potential which was not included in the original Bulb model (Cherry et al. 2012). It was also shown that the

axial symmetry around the radial direction in the Bulb model can be broken spontaneously during collective neutrino oscillations (Raffelt et al. 2013, Mirizzi 2013). Some very recent work has shown that the spatial symmetries in the low-dimensional models such as the spherical symmetry in the Bulb model can be broken in multi-dimensional models (Mangano et al. 2014, Duan and Shalgar 2015, Mirizzi et al. 2015, Mirizzi 2015, Chakraborty et al. 2016).

In this chapter we study the breaking of the spatial symmetry in a dense neutrino gas. For this purpose, we use the neutrino Line model which has two spatial dimensions. The study of this model can provide us with useful insights into the qualitative differences between the phenomenologies of collective neutrino oscillations in models of one and multiple spatial dimensions.

This study is a generalization of the work done for the two-beam Line model (see (Duan and Shalgar 2015)) where only two neutrino beams are emitted from each neutrino source point on the line.

4.1 The neutrino Line model

4.1.1 Equations of motion

In the stationary, two-dimensional (neutrino) Line model neutrinos and antineutrinos are emitted from the x -axis or the “neutrino Line” and propagate in the x - z plane (see Fig. 4.1). We assume that the neutrinos and antineutrinos are of single energy E and the same normalized angular distribution $g(\vartheta)$ such that the number fluxes of the neutrino and antineutrino within angle range $[\vartheta, \vartheta + d\vartheta]$ are $n_\nu g(\vartheta)d\vartheta$ and $n_{\bar{\nu}}g(\vartheta)d\vartheta$, respectively, where ϑ is the emission angle of the neutrino beam, and n_ν and $n_{\bar{\nu}}$ are the (constant) total number densities of the neutrino and antineutrino, respectively. The flavor quantum states of the neutrino and antineutrino of emission

Chapter 4. Flavor Instabilities in the Neutrino Line Model

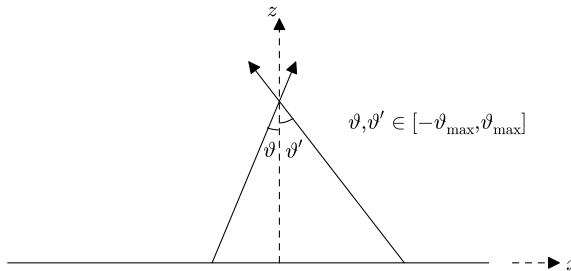


Figure 4.1: A schematic diagram of the two-dimensional (neutrino) Line model. Each point on the x -axis or the “neutrino Line” emits neutrino beams with emission angles ϑ within the range $[-\vartheta_{\max}, \vartheta_{\max}]$. Reprinted figure with permission from [S. Abbar et al, Phys. Rev. D 92, 065019, 2015](#) (Ref. (Abbar et al. 2015b)). Copyright 2015 by the American Physical Society.

angle ϑ and at position (x, z) are given by density matrices $\rho_{\vartheta}(x, z)$ and $\bar{\rho}_{\vartheta}(x, z)$, respectively (Sigl and Raffelt 1993). We use the normalization condition

$$\text{tr}\rho = \text{tr}\bar{\rho} = 1 \quad (4.1)$$

such that the diagonal elements of a density matrix give the probabilities for the neutrino or antineutrino to be in the corresponding weak-interaction states. With these conventions the self-interaction potential (see Eq. (3.35)) for $\rho_{\vartheta}(x, z)$ in the Line model can be written as

$$H_{\nu\nu,\vartheta}(x, z) = \mu \int [\rho_{\vartheta'}(x, z) - \alpha \bar{\rho}_{\vartheta'}(x, z)] [1 - \cos(\vartheta - \vartheta')] g(\vartheta') d\vartheta', \quad (4.2)$$

where $\mu = \sqrt{2}G_F n_{\nu}$ and $\alpha = n_{\bar{\nu}}/n_{\nu}$. In the Line model the strength of the neutrino self-interaction μ is constant. In realistic astrophysical environments such as core-collapse supernovae, however, μ can decrease with increasing distance from the neutrino source.

In the absence of collision, the flavor evolution of the neutrino obeys the Liouville equation (Sigl and Raffelt 1993, Strack and Burrows 2005, Cardall 2008)

$$\partial_t \rho + \mathbf{v} \cdot \nabla \rho = -i[H_{\text{vac}} + H_{\text{mat}} + H_{\nu\nu}, \rho], \quad (4.3)$$

Chapter 4. Flavor Instabilities in the Neutrino Line Model

where \mathbf{v} is the velocity of the neutrino, $\rho(t, \mathbf{x}, \mathbf{p})$ is the (Wigner-transformed) flavor density matrices of the neutrino which depends on time t , position \mathbf{x} and neutrino momentum \mathbf{p} , H_{vac} is the standard vacuum Hamiltonian, and H_{mat} and $H_{\nu\nu}$ are the matter and neutrino potentials (see Eq. 3.25), respectively. Here we assume the mixing between two active neutrino flavors ν_e and ν_x with a small vacuum mixing angle $\theta \ll 1$. Therefore,

$$H_\omega = H_{\text{vac}} + H_{\text{mat}} \approx \frac{(\lambda - \eta\omega)}{2} \begin{pmatrix} 1 & 0 \\ 0 & -1 \end{pmatrix} = \frac{(\lambda - \eta\omega)}{2} \sigma_3, \quad (4.4)$$

where $\lambda = V_{CC} = \sqrt{2}G_F n_e$ with n_e being the net electron number density, η is a parameter which takes a value of +1 (−1) for the normal (inverted) neutrino mass hierarchy or NH (IH). For the stationary line model, Eq. (4.3) can be written in a more explicit form:

$$i(\cos \vartheta \partial_z + \sin \vartheta \partial_x) \rho_\vartheta = \frac{(\lambda - \eta\omega)}{2} [\sigma_3, \rho_\vartheta] + \mu \int [1 - \cos(\vartheta - \vartheta')] [\rho_{\vartheta'} - \alpha \bar{\rho}_{\vartheta'}, \rho_\vartheta] g(\vartheta') d\vartheta'. \quad (4.5)$$

The EoM for $\bar{\rho}_\vartheta$ is the same as Eq. (4.5) except with replacement $\omega \rightarrow -\omega$.

Following Duan and Shalgar (2015), we impose a periodic boundary condition along the x -axis such that $\rho_\vartheta(x + L, z) = \rho_\vartheta(x, z)$ and $\bar{\rho}_\vartheta(x + L, z) = \bar{\rho}_\vartheta(x, z)$, where L is the basic period. It is convenient to recast the x -dependence of the neutrino density matrix in terms of Fourier moments:

$$\rho_{m,\vartheta}(z) = \frac{1}{L} \int_0^L e^{-ik_m x} \rho_\vartheta(x, z) dx, \quad \bar{\rho}_{m,\vartheta}(z) = \frac{1}{L} \int_0^L e^{-ik_m x} \bar{\rho}_\vartheta(x, z) dx, \quad (4.6)$$

where $k_m = 2\pi m/L$. It is straightforward to derive the EoM in the moment basis

which are

$$\begin{aligned}
 i \cos \vartheta \partial_z \rho_{m,\vartheta} &= k_m \sin \vartheta \rho_{m,\vartheta} + \frac{(\lambda - \eta\omega)}{2} [\sigma_3, \rho_{m,\vartheta}] \\
 &+ \mu \sum_{m'} \int [\rho_{m',\vartheta'} - \alpha \bar{\rho}_{m',\vartheta'}, \rho_{m-m',\vartheta}] [1 - \cos(\vartheta - \vartheta')] g(\vartheta') d\vartheta',
 \end{aligned}
 \tag{4.7a}$$

$$\begin{aligned}
 i \cos \vartheta \partial_z \bar{\rho}_{m,\vartheta} &= k_m \sin \vartheta \bar{\rho}_{m,\vartheta} + \frac{(\lambda + \eta\omega)}{2} [\sigma_3, \bar{\rho}_{m,\vartheta}] \\
 &+ \mu \sum_{m'} \int [\rho_{m',\vartheta'} - \alpha \bar{\rho}_{m',\vartheta'}, \bar{\rho}_{m-m',\vartheta}] [1 - \cos(\vartheta - \vartheta')] g(\vartheta') d\vartheta'.
 \end{aligned}
 \tag{4.7b}$$

4.1.2 Collective modes in the linear regime

We assume that the neutrinos and antineutrinos are emitted from the line source in the electron flavor only. In the regime where neutrino oscillations are insignificant, the neutrino density matrices have the form

$$\rho_\vartheta(x, z) \approx \begin{pmatrix} 1 & \epsilon_\vartheta \\ \epsilon_\vartheta^* & 0 \end{pmatrix}, \quad \bar{\rho}_\vartheta(x, z) \approx \begin{pmatrix} 1 & \bar{\epsilon}_\vartheta \\ \bar{\epsilon}_\vartheta^* & 0 \end{pmatrix}. \tag{4.8}$$

When there is a flavor instability, the off-diagonal elements of the density matrices grow exponentially, which can result in collective neutrino oscillations. In this section we apply the method of flavor stability analysis to the multi-angle Line model which was first developed by Banerjee et al. (2011).

In the moment basis we have

$$\rho_{m,\vartheta}(z) \approx \begin{pmatrix} \delta_{0,m} & \epsilon_{m,\vartheta} \\ \epsilon_{-m,\vartheta}^* & 0 \end{pmatrix}, \quad \bar{\rho}_{m,\vartheta}(z) \approx \begin{pmatrix} \delta_{0,m} & \bar{\epsilon}_{m,\vartheta} \\ \bar{\epsilon}_{-m,\vartheta}^* & 0 \end{pmatrix} \tag{4.9}$$

Chapter 4. Flavor Instabilities in the Neutrino Line Model

Keeping only the terms up to $\mathcal{O}(\epsilon)$ in Eq. (4.7) we obtain

$$i \cos \vartheta \partial_z \epsilon_{m,\vartheta} = [k_m \sin \vartheta + \lambda - \omega \eta + (1 - \alpha) \tilde{\mu}_\vartheta] \epsilon_{m,\vartheta} - \mu \int [1 - \cos(\vartheta - \vartheta')] (\epsilon_{m,\vartheta'} - \alpha \bar{\epsilon}_{m,\vartheta'}) g(\vartheta') d\vartheta', \quad (4.10a)$$

$$i \cos \vartheta \partial_z \bar{\epsilon}_{m,\vartheta} = [k_m \sin \vartheta + \lambda + \omega \eta + (1 - \alpha) \tilde{\mu}_\vartheta] \bar{\epsilon}_{m,\vartheta} - \mu \int [1 - \cos(\vartheta - \vartheta')] (\epsilon_{m,\vartheta'} - \alpha \bar{\epsilon}_{m,\vartheta'}) g(\vartheta') d\vartheta', \quad (4.10b)$$

where

$$\tilde{\mu}_\vartheta = \mu \int [1 - \cos(\vartheta - \vartheta')] g(\vartheta') d\vartheta' \quad (4.11)$$

is the effective strength of neutrino self-interaction for the neutrino beam with emission angle ϑ . As in the two-beam model, the flavor evolution of the neutrino fluxes in different moments is decoupled in the linear regime, although the evolution of the neutrino moments with different emission angles ϑ are still coupled.

Assuming that the m th neutrino moment oscillates with collective oscillation frequency Ω_m , we can write

$$\epsilon_{m,\vartheta}(z) = Q_{m,\vartheta} e^{-i\Omega_m z}, \quad \bar{\epsilon}_{m,\vartheta}(z) = \bar{Q}_{m,\vartheta} e^{-i\Omega_m z}, \quad (4.12)$$

where $Q_{m,\vartheta}$ and $\bar{Q}_{m,\vartheta}$ are z -independent. Applying this ansatz to Eq. (4.10) we obtain

$$D_m(\omega, \vartheta) Q_{m,\vartheta} = (a_m - c_m \cos \vartheta - s_m \sin \vartheta) \mu, \quad (4.13a)$$

$$D_m(-\omega, \vartheta) \bar{Q}_{m,\vartheta} = (a_m - c_m \cos \vartheta - s_m \sin \vartheta) \mu \quad (4.13b)$$

or

$$Q_{m,\vartheta} = \frac{(a_m - c_m \cos \vartheta - s_m \sin \vartheta) \mu}{D_m(\omega, \vartheta)}, \quad (4.14a)$$

$$\bar{Q}_{m,\vartheta} = \frac{(a_m - c_m \cos \vartheta - s_m \sin \vartheta) \mu}{D_m(-\omega, \vartheta)}, \quad (4.14b)$$

Chapter 4. Flavor Instabilities in the Neutrino Line Model

where

$$D_m(\pm\omega, \vartheta) = -\Omega \cos \vartheta + k_m \sin \vartheta + \lambda \mp \omega \eta + (1 - \alpha) \tilde{\mu}_\vartheta, \quad (4.15)$$

and

$$a_m = \int (Q_{m,\vartheta'} - \alpha \bar{Q}_{m,\vartheta'}) g(\vartheta') d\vartheta', \quad (4.16a)$$

$$c_m = \int (Q_{m,\vartheta'} - \alpha \bar{Q}_{m,\vartheta'}) \cos \vartheta' g(\vartheta') d\vartheta', \quad (4.16b)$$

$$s_m = \int (Q_{m,\vartheta'} - \alpha \bar{Q}_{m,\vartheta'}) \sin \vartheta' g(\vartheta') d\vartheta'. \quad (4.16c)$$

Substituting Eq. (4.14) in Eq. (4.16) we obtain a characteristic equation for (a_m, c_m, s_m) :

$$\begin{pmatrix} I_m[1] - 1 & -I_m[\cos \vartheta] & -I_m[\sin \vartheta] \\ I_m[\cos \vartheta] & -I_m[\cos^2 \vartheta] - 1 & -I_m[\cos \vartheta \sin \vartheta] \\ I_m[\sin \vartheta] & -I_m[\cos \vartheta \sin \vartheta] & -I_m[\sin^2 \vartheta] - 1 \end{pmatrix} \begin{pmatrix} a_m \\ c_m \\ s_m \end{pmatrix} = 0, \quad (4.17)$$

where

$$I_m[f(\vartheta)] = \int f(\vartheta) g(\vartheta) \left[\frac{\mu}{D_m(\omega, \vartheta)} - \frac{\alpha \mu}{D_m(-\omega, \vartheta)} \right] d\vartheta \quad (4.18)$$

for arbitrary function $f(\vartheta)$. Eq. (4.17) holds only when

$$\det \begin{vmatrix} I_m[1] - 1 & -I_m[\cos \vartheta] & -I_m[\sin \vartheta] \\ I_m[\cos \vartheta] & -I_m[\cos^2 \vartheta] - 1 & -I_m[\cos \vartheta \sin \vartheta] \\ I_m[\sin \vartheta] & -I_m[\cos \vartheta \sin \vartheta] & -I_m[\sin^2 \vartheta] - 1 \end{vmatrix} = 0. \quad (4.19)$$

For given m , λ and μ one can find a set of $\Omega_m^{(i)}(\lambda, \mu)$ ($i = 1, 2, \dots$) which satisfy Eq. (4.19) and which are the frequencies of the corresponding normal modes of collective neutrino oscillations. When

$$\kappa_m^{(i)} = \text{Im}(\Omega_m^{(i)}) \quad (4.20)$$

is positive, the corresponding normal mode is unstable and its amplitude grows exponentially. If there exist multiple unstable modes, the mode with the largest exponential growth rate,

$$\kappa_m^{\max} = \max(\kappa_m^{(i)}), \quad (4.21)$$

will eventually dominate.

4.2 Results in the linear regime

4.2.1 Numerical results

We develop a computer code to solve Eq. (4.7) numerically. In this code the continuous range of ϑ is represented by N discrete angle bins with central value ϑ_i ($i = 1, \dots, N$) and equal interval $\Delta\vartheta$. For an arbitrary function $f(\vartheta)$ one has

$$\int f(\vartheta) d\vartheta \longrightarrow \Delta\vartheta \sum_{i=1}^N f(\vartheta_i). \quad (4.22)$$

In our study we focus on the neutrino oscillations in the linear regime and the cases with a simple angular distribution which has isotropic neutrino fluxes within the range $[-\vartheta_{\max}, \vartheta_{\max}]$, i.e.

$$g(\vartheta) = \begin{cases} \frac{1}{2}\vartheta_{\max}^{-1} & \text{if } \vartheta \in [-\vartheta_{\max}, \vartheta_{\max}], \\ 0 & \text{otherwise.} \end{cases} \quad (4.23)$$

We choose to present our results with the following parameters

$$\vartheta_{\max} = \pi/6, \quad \alpha = 0.8 \quad \text{and} \quad L = 40\pi\omega^{-1}. \quad (4.24)$$

Because the evolution of different neutrino moments is decoupled in the linear regime, it is sufficient to include only the 0th and m th moments in studying the evolution

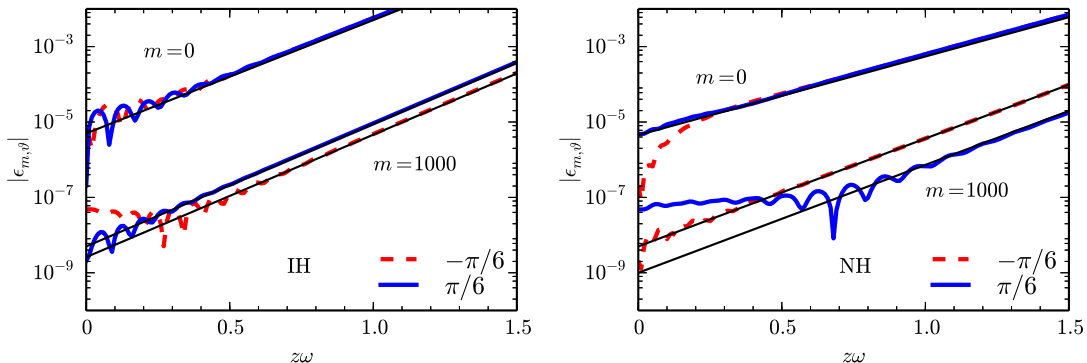


Figure 4.2: The evolution of $|\epsilon_{m,\vartheta}|$, the amplitudes of the off-diagonal elements of the neutrino moment matrices $\rho_{m,\vartheta}(z)$, in terms of propagation distance z for the inverted (left) and normal (right) neutrino mass hierarchies. The thick curves represent the numerical solution to Eq. (4.7) with the 0th and 1000th moments only. The thin solid lines represent the exponential growth functions $\sim \exp(\kappa_m^{\max} z)$ predicted by the linear stability analysis. In these calculations we used the parameters listed in Eq. (4.24), and we took the matter potential $\lambda = 0$ and neutrino potential $\mu/\omega = 1500$ (left) and 3000 (right) which is measured in the vacuum neutrino oscillation frequency ω . Reprinted figure with permission from [S. Abbar et al, Phys. Rev. D 92, 065019, 2015](#) (Ref. (Abbar et al. 2015b)). Copyright 2015 by the American Physical Society.

of the m th moment in this regime. [The 0th moment is needed because it has large diagonal elements even in the linear regime. See Eq. (4.9).]

In Fig. 4.2 we show the numerical solutions to Eq. (4.7) in two calculations with all but the 0th and 1000th moments being zero. In both calculations, $|\epsilon_{m,\vartheta}|$, the amplitudes of the off-diagonal elements of $\rho_{m,\vartheta}$, grow exponentially which is understood as flavor instabilities. As a comparison we plot in Fig. 4.2 the exponential growth functions $\sim \exp(\kappa_m^{\max} z)$ predicted by the flavor stability analysis, and they agree with the numerical results very well. As a further confirmation, we have compared the shapes of $|Q_{m,\vartheta}|$ and $|\bar{Q}_{m,\vartheta}|$ obtained from the flavor stability analysis (the dotted and dashed curves in Fig. 4.3) with those of $|\epsilon_{m,\vartheta}|$ and $|\bar{\epsilon}_{m,\vartheta}|$ in numerical calculations (not shown), and they also have good agreement. However, to achieve numerical convergence a large number of angle bins may be needed for the following

Chapter 4. Flavor Instabilities in the Neutrino Line Model

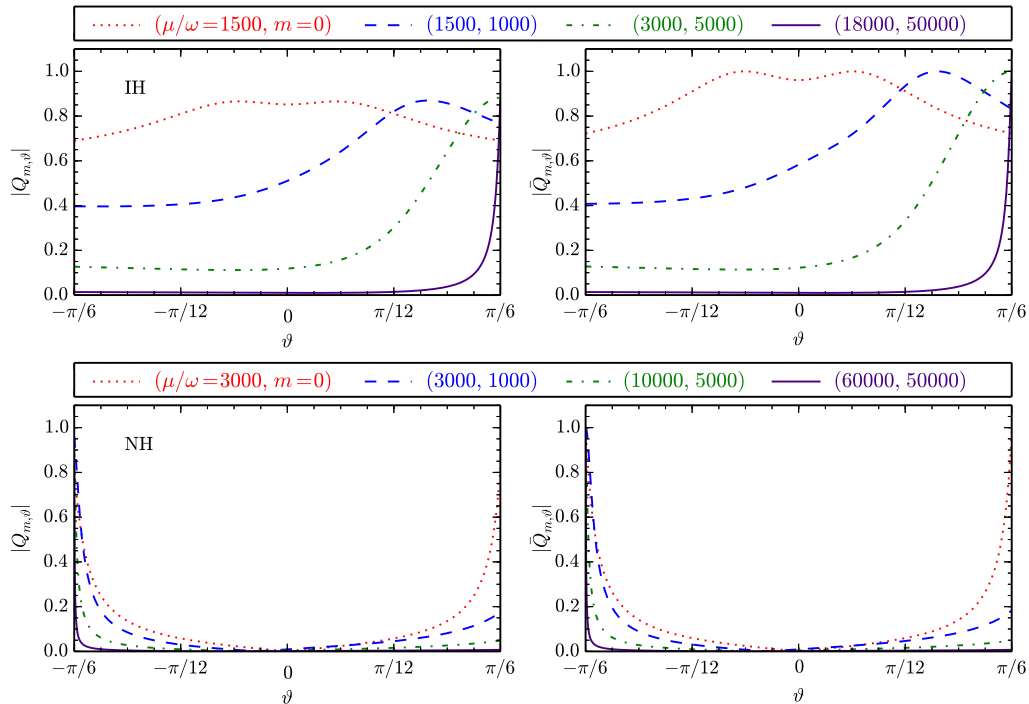


Figure 4.3: The amplitudes of the unstable modes of the m th neutrino moments (in arbitrary scale) as functions of neutrino emission angle ϑ which have the largest exponential growth rates in the linear regime at given neutrino number densities (indicated by $\mu = \sqrt{2}G_F n_\nu$ which is measured in the vacuum neutrino oscillation frequency ω). The top and bottom panels are for the inverted and normal neutrino mass hierarchies, respectively. In these calculations we used the parameters listed in Eq. (4.24), and we took the matter potential $\lambda = 0$. Reprinted figure with permission from S. Abbar et al, *Phys. Rev. D* 92, 065019, 2015 (Ref. (Abbar et al. 2015b)). Copyright 2015 by the American Physical Society.

reason.

As pointed out by Sarikas et al. (2012), there can exist many spurious flavor instabilities in the numerical implementation using the discrete (angle-bin) scheme.

Chapter 4. Flavor Instabilities in the Neutrino Line Model

This can be seen from the discretized version of Eq. (4.10):

$$i \cos \vartheta_i \partial_z \epsilon_{m,\vartheta_i} = [k_m \sin \vartheta_i + \lambda - \omega \eta + (1 - \alpha) \tilde{\mu}_{\vartheta_i}] \epsilon_{m,\vartheta_i} - \mu \Delta \vartheta \sum_j [1 - \cos(\vartheta_i - \vartheta_j)] (\epsilon_{m,\vartheta_j} - \alpha \bar{\epsilon}_{m,\vartheta_j}) g(\vartheta_j), \quad (4.25a)$$

$$i \cos \vartheta_i \partial_z \bar{\epsilon}_{m,\vartheta_i} = [k_m \sin \vartheta_i + \lambda + \omega \eta + (1 - \alpha) \tilde{\mu}_{\vartheta_i}] \bar{\epsilon}_{m,\vartheta_i} - \mu \Delta \vartheta \sum_j [1 - \cos(\vartheta_i - \vartheta_j)] (\epsilon_{m,\vartheta_j} - \alpha \bar{\epsilon}_{m,\vartheta_j}) g(\vartheta_j), \quad (4.25b)$$

or

$$i \partial_z \boldsymbol{\epsilon}_m = \boldsymbol{\Lambda}_m \cdot \boldsymbol{\epsilon}_m, \quad (4.26)$$

where $\boldsymbol{\epsilon}_m = (\epsilon_{m,\vartheta_1}, \bar{\epsilon}_{m,\vartheta_1}, \epsilon_{m,\vartheta_2}, \bar{\epsilon}_{m,\vartheta_2}, \dots, \epsilon_{m,\vartheta_N}, \bar{\epsilon}_{m,\vartheta_N})^T$ is a $2N$ -dimensional vector, and $\boldsymbol{\Lambda}_m$ is a $2N \times 2N$ real matrix. Matrix $\boldsymbol{\Lambda}_m$ has $2N$ eigenvalues $\Omega_m^{(i)}$ ($i = 1, 2, \dots, 2N$) each of which corresponds to the collective oscillation frequency of a collective mode in the discrete scheme. Many of these collective modes can be unstable, i.e. with $\kappa_m^{(i)} = \text{Im}(\Omega_m^{(i)}) > 0$. Only a few of the unstable modes correspond to the physical instabilities in the continuum limit (of the ϑ distribution), and the rest of them are “spurious” or the artifact of the numerical implementation.

In Fig. 4.4 we plot the exponential growth rates $\kappa_m^{(i)}$ of all the unstable collective modes both in the discrete scheme and in the continuum limit for the 0th and 5000th moments, respectively. This figure shows that spurious instabilities (in the discrete scheme) can dominate the physical instabilities (in the continuum limit) on small distance scales and/or large neutrino number densities (i.e. large $|m|$ and/or μ). In some extreme cases, e.g., the bottom middle panel of Fig. 4.4 where $\eta = +1$, $m = 5000$ and $N = 100$, none of the collective modes in the discrete scheme matches the ones in the continuum limit. This is likely due to the fact that $Q_{m,\vartheta}$ and $\bar{Q}_{m,\vartheta}$ become sharply peaked functions of ϑ at large $|m|$ and/or μ , which requires many angle bins to resolve (see Fig. 4.3). Indeed, the comparison between the middle and right panels of Fig. 4.4 shows that the spurious instabilities are more suppressed when more angle bins are employed.

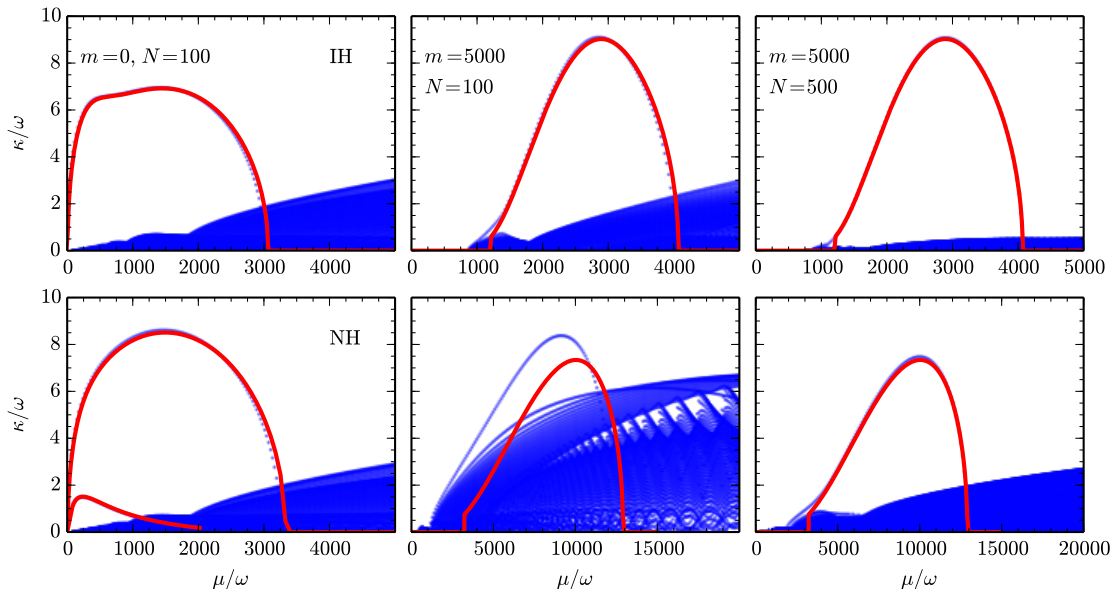


Figure 4.4: The exponential growth rates $\kappa_m^{(i)}$ of the unstable collective modes of the m th neutrino moment as functions of neutrino self-interaction strength $\mu = \sqrt{2}G_F n_\nu$ in the discrete angle-bin scheme with N angle bins (as labeled and shown as the dotted curves) and in the continuum limit of angular distribution (solid curves), respectively. Both κ and μ are measured in the vacuum neutrino oscillation frequency ω . The top and bottom panels are for the inverted and normal neutrino mass hierarchies, respectively. In these calculations we used the parameters listed in Eq. (4.24), and we took the matter potential $\lambda = 0$. Reprinted figure with permission from S. Abbar et al, *Phys. Rev. D* **92**, 065019, 2015 (Ref. (Abbar et al. 2015b)). Copyright 2015 by the American Physical Society.

4.2.2 Flavor instabilities and matter effect

We have solved the flavor instabilities of the multi-angle Line model using the angular distribution in Eq. (4.23) and the parameters listed in Eq. (4.24). The results for the neutrino gas in the absence of matter are shown in the upper panels of Fig. 4.5. From this figure one can see that, unlike the two-beam Line model (Duan and Shalgar 2015), the flavor instabilities in the multi-angle model depend on the neutrino mass hierarchy, and collective oscillations can begin at larger neutrino

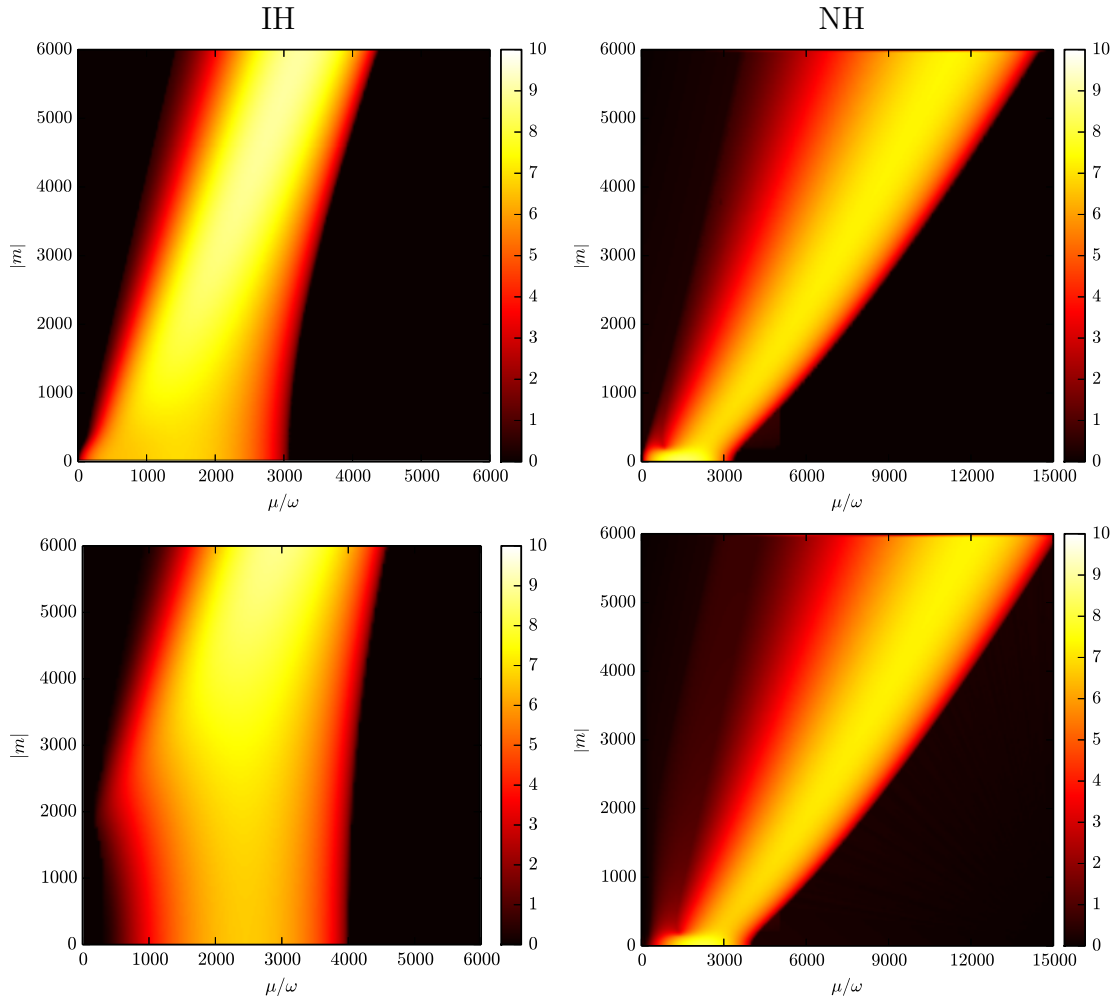


Figure 4.5: Maximum exponential growth rate $\kappa_m^{\max}(\lambda, \mu)$ (indicated by the color scale) of the collective neutrino oscillation modes in the multi-angle Line model as a function of moment index m and the neutrino self-coupling strength $\mu = \sqrt{2}G_F n_\nu$. Both κ and μ are measured in the vacuum neutrino oscillation frequency ω . The left and right panels are for the inverted and normal neutrino mass hierarchies, respectively, and the top and bottom panels are for $\lambda = \sqrt{2}G_F n_e = 0$ and 200ω , respectively. In these calculations we assume isotropic neutrino fluxes within angular range $\vartheta \in [-\pi/6, \pi/6]$, and we used the parameters listed in Eq. (4.24). Reprinted figure with permission from S. Abbar et al, *Phys. Rev. D* 92, 065019, 2015 (Ref. (Abbar et al. 2015b)). Copyright 2015 by the American Physical Society.

density in NH than in IH. One also sees that both μ_m^{\max} and μ_m^{\min} , the maximum and minimum μ values where the m th modes are unstable, seem to increase linearly with $|m|$. In contrast, both μ_m^{\max} and μ_m^{\min} increase linearly with $\sqrt{|m|}$ in the two-beam model.¹ This implies that, for sufficiently large $|m|$, flavor instabilities can develop at even larger neutrino densities in the multi-angle model than in the two-beam model.

Unlike in the two-beam model, the presence of matter can affect collective oscillations in the multi-angle model because the neutrinos propagate in different directions can travel through different distances between two lines that are parallel to the neutrino line. In the lower panels of Fig. 4.5 we show the flavor instabilities in the multi-angle Line model with $\lambda = 200\omega$. Similar to the situation in the spherical neutrino Bulb model for supernova (Banerjee et al. 2011, Esteban-Pretel et al. 2008), both μ_m^{\max} and μ_m^{\min} of the homogeneous mode (i.e. with $m = 0$) shift to larger values in the presence of a large matter density in both NH and IH. However, μ_m^{\min} of inhomogeneous modes actually shifts to smaller values for both NH and IH when $|m|$ is sufficiently large.

4.3 Discussion

Although the Line model does not represent any real physical environment, the study of this toy model can provide insights into the important differences between the models of one spatial dimension (e.g. the neutrino Bulb model for supernova) and multi-dimension models.

An important goal of our study is to check if the inhomogeneous collective modes are suppressed in the multi-angle environment because of the high neutrino densities

¹The neutrino self-coupling strength μ defined by Duan and Shalgar (2015) has taken into account the geometric factor $1 - \cos(\vartheta - \vartheta')$ and is equivalent to $\tilde{\mu}_\vartheta$ in this chapter. For the angular distribution in Eq. (4.23) $\tilde{\mu}_0 = (1 - \sin \vartheta_{\max}/\vartheta_{\max})\mu \approx 0.045\mu$.

Chapter 4. Flavor Instabilities in the Neutrino Line Model

which is known to exist in the Bulb model (Duan and Friedland 2011, Esteban-Pretel et al. 2008). Somewhat surprisingly, our work suggests that, in the absence of ordinary matter, inhomogeneous collective modes on small scales are not only not suppressed in the multi-angle environment, but can become unstable at larger neutrino densities than in the two-beam model.

We also examined whether the presence of a large matter density can suppress collective oscillations in the two-dimensional Line model as in the one-dimensional Bulb model (Esteban-Pretel et al. 2008). Our study shows that the presence of ambient matter does suppress inhomogeneous oscillation modes on large distance scales in the Line model as it occurs to the homogeneous modes in the Bulb model. However, it appears that the inhomogeneous modes on very small scales can occur at smaller neutrino number densities with ambient matter than without. In addition, the flavor unstable region of the certain inhomogeneous modes can extend to the regime of lower neutrino densities than that for the homogeneous mode.

We have shown that, as in the Bulb model, there exist spurious oscillations in the numerical implementation of the multi-angle Line model if the discrete angle-bin scheme is employed. The problem of spurious oscillations appears to be more severe at higher neutrino densities and on smaller distance scales. Although this problem can be mitigated by using more angle bins, it does add complications to the already challenging task of computing collective neutrino oscillations near astrophysical neutrino sources such as core-collapse supernovae and black-hole accretion disks. It is probably helpful to develop the multipole expansion method similar to that for the Bulb model (Duan and Shalgar 2014).

Our study in this chapter has focused on the neutrino flavor instabilities in the linear regime. However, not every flavor instability in the linear regime can result in significant neutrino flavor transformation. For example, in the realistic supernova environment, the neutrino density decreases as neutrinos travel away from the center

Chapter 4. Flavor Instabilities in the Neutrino Line Model

of the supernova which results in the shift of the instability region. It is, therefore, possible that a collective oscillation mode does not grow all the way to the nonlinear regime during the finite distance interval where it is unstable. We have considered the mixing of two neutrino flavors only, which can be quite different from the neutrino flavor transformation of three flavors (Friedland 2010). Ultimately, the phenomenon of collective neutrino oscillations has to be studied in realistic, multi-dimensional models for compact objects such as core-collapse supernovae and black-hole accretion disks before one can fully understand the impact of neutrino oscillations to these extreme environments.

Chapter 5

Neutrino Flavor Instabilities in Time-Dependent Bulb Model

One of the essential assumptions behind the neutrino Bulb model is that it is an stationary model. In the Bulb model, it is assumed that one can impose the time translation symmetry because the timescale of neutrino oscillations is much shorter than those in the neutrino emission or dynamic evolution in supernovae. However, as discussed in the previous chapter, it turns out that very small deviations from the initial symmetric conditions can be amplified by the symmetry-breaking oscillation modes in a dense neutrino gas.

It is natural to wonder if collective neutrino oscillations can also break the time-translation symmetry spontaneously in supernovae (Raffelt et al. 2013). If they do, then a time-independent supernova model may not accurately describe the neutrino oscillation phenomenon in supernovae even though the typical timescale of the variation in the neutrino emission is much longer than that of neutrino oscillations. In this chapter we analyze the neutrino flavor stability in a time-dependent supernova model which should provide some interesting insights to this question.

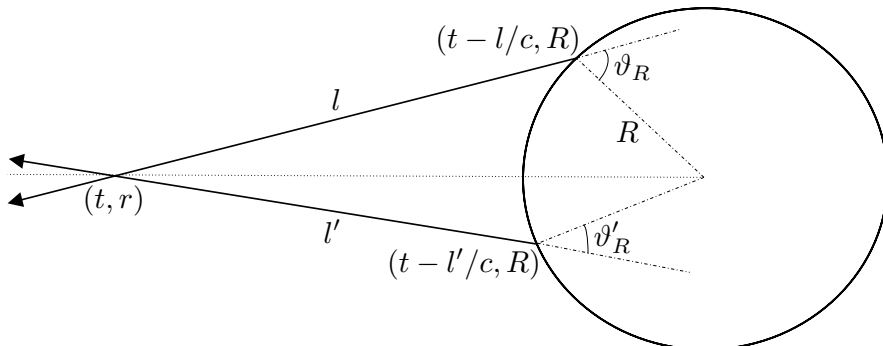


Figure 5.1: The geometric picture of the time-dependent (neutrino) Bulb model for the supernova. Two neutrinos emitted from the neutrino sphere of radius R with emission angles ϑ_R and ϑ'_R and at time $t - l/c$ and $t - l'/c$ meet each other at radius r and time t , where l and l' are the distances by which the two neutrinos have traveled from the neutrino sphere to their meeting point, respectively. Figure adapted from (Abbar and Duan 2015).

5.1 Time-dependent neutrino Bulb model

We will focus on the potential differences between the results obtained from the time-dependent and stationary supernova models. Therefore, we will employ the time-dependent Bulb model which has the same spatial spherical symmetry and the directional axial symmetry as in the conventional Bulb model. Unlike the conventional stationary Bulb model, however, we will not assume that the emission and flavor evolution of the neutrinos are time-independent (see Fig. 5.1). For simplicity, we will consider the mixing between two active flavors, the e and x flavors, with the latter being the linear superposition of the μ and τ flavors. We also assume a small vacuum mixing angle $\theta \ll 1$.

We define reduced neutrino density matrix

$$\rho(t; r; \omega, u) \propto \begin{cases} \rho & \text{if } \omega > 0, \\ \bar{\rho} & \text{if } \omega < 0 \end{cases} \quad (5.1)$$

Chapter 5. Neutrino Flavor Instabilities in Time-Dependent Bulb Model

where $\bar{\rho}$ is the antineutrino density matrix. One has the normalization condition

$$\text{tr}\rho = 1, \quad (5.2)$$

where $u = \sin^2 \vartheta_R$ with ϑ_R being the emission angle of the neutrino on the neutrino sphere (see Fig. 5.1), and r is the radial distance from the center of the supernova. In the time-dependent Bulb model, the EoM for the (reduced) density matrix (see Eq. (4.3)) ρ can be written as

$$i(\partial_t + v_u \partial_r)\rho = [H_{\text{vac}} + H_{\text{mat}} + H_{\nu\nu}, \rho], \quad (5.3)$$

where

$$v_u(r) = \sqrt{1 - \left(\frac{R}{r}\right)^2} u \quad (5.4)$$

is the radial velocity of the neutrino.

In this chapter we assume that the number flux $F_{\nu_\alpha/\bar{\nu}_\alpha}(E, \vartheta_R)$ of the neutrino or antineutrino in flavor α ($\alpha = e, x$) is time independent (Mirizzi and Serpico 2012). We define the distribution function of the neutrino emission to be

$$g(\omega, u) \propto \left| \frac{dE}{d\omega} \right| \times \begin{cases} (F_{\nu_e} + F_{\nu_x}) & \text{if } \omega > 0, \\ -(F_{\bar{\nu}_e} + F_{\bar{\nu}_x}) & \text{if } \omega < 0 \end{cases} \quad (5.5)$$

with normalization conditions

$$\int_0^\infty d\omega \int_0^1 \frac{du}{2} g(\omega, u) = 1, \quad (5.6a)$$

$$\int_{-\infty}^0 d\omega \int_0^1 \frac{du}{2} g(\omega, u) = -\frac{N_{\bar{\nu}}^{\text{tot}}}{N_{\nu}^{\text{tot}}}, \quad (5.6b)$$

where

$$N_{\nu}^{\text{tot}} = \int_0^\infty dE \int_0^1 \frac{du}{2} (F_{\nu_e} + F_{\nu_x}), \quad (5.7a)$$

$$N_{\bar{\nu}}^{\text{tot}} = \int_0^\infty dE \int_0^1 \frac{du}{2} (F_{\bar{\nu}_e} + F_{\bar{\nu}_x}) \quad (5.7b)$$

are the total number luminosities of the neutrino and antineutrino (i.e. the number of neutrinos or antineutrinos emitted by the whole neutrino sphere per unit time), respectively. The opposite signs of $g(\omega, u)$ for the neutrino and antineutrino in Eq. (5.5) take into account their different contributions to the neutrino potential in Eq. (4.3). In the Bulb model the neutrino potential can be written as (see Eq. (3.35))

$$H_{\nu\nu}(t; r; u) = \frac{\sqrt{2}G_{\text{F}}N_{\nu}^{\text{tot}}}{4\pi r^2} \int_{-\infty}^{\infty} d\omega' \int_0^1 \frac{du'}{v_{u'}} (1 - v_u v_{u'}) \times g(\omega', u') \rho(t; r; \omega', u'). \quad (5.8)$$

Because collective neutrino oscillations usually occur in the regime $R/r \ll 1$ in the Bulb model, we will take the large-radius approximation (Esteban-Pretel et al. 2008)

$$v_u(r) \approx 1 - \left(\frac{R}{r}\right)^2 \frac{u}{2}. \quad (5.9)$$

In this approximation,

$$H_{\nu\nu}(t; r; u) \approx \mu \int \left(\frac{u + u'}{2}\right) g' \rho' d\Gamma', \quad (5.10)$$

where all the primed quantities are functions of u' and ω' , e.g., $\rho' = \rho(t; \omega', u'; r)$,

$$\mu(r) = \frac{\sqrt{2}G_{\text{F}}N_{\nu}^{\text{tot}}}{4\pi R^2} \left(\frac{R}{r}\right)^4 \quad (5.11)$$

is the strength of the neutrino potential at radius r , and

$$\int d\Gamma' \equiv \int_{-\infty}^{\infty} d\omega' \int_0^1 du'. \quad (5.12)$$

5.2 Linear regime

In the regime where no significant flavor transformation has occurred, the linear flavor-stability analysis is applicable (Banerjee et al. 2011). In this regime the neutrino density matrices take the form

$$\rho(t; r; \omega, u) \approx \frac{\rho_{ee} + \rho_{xx}}{2} \begin{pmatrix} 1 & 0 \\ 0 & 1 \end{pmatrix} + \frac{\rho_{ee} - \rho_{xx}}{2} \begin{pmatrix} 1 & \epsilon \\ \epsilon^* & -1 \end{pmatrix}, \quad (5.13)$$

Chapter 5. Neutrino Flavor Instabilities in Time-Dependent Bulb Model

where $\rho_{ee}(\omega, u)$ and $\rho_{xx}(\omega, u)$ are the probabilities for the neutrino (or antineutrino) to be in the e and x flavors, respectively, and $|\epsilon(t; r; \omega, u)| \ll 1$. Here in the spirit of flavor-stability analysis we have assumed that ρ_{ee} and ρ_{xx} are approximately constant. At the onset of collective neutrino oscillations ϵ grow exponentially. If ϵ has strong time dependence, the time translation symmetry is broken spontaneously by collective neutrino oscillations.

Keeping only the terms up to $\mathcal{O}(\epsilon)$ in Eq. (5.3) we obtain

$$i(\partial_t + v_u \partial_r) \epsilon \approx (-\eta\omega + \lambda + C) \epsilon - \frac{\mu}{2} \int (u + u')(\rho'_{ee} - \rho'_{xx})g' \epsilon' d\Gamma', \quad (5.14)$$

where

$$C(u, \mu) = \frac{\mu}{2} \int (u + u')(\rho'_{ee} - \rho'_{xx})g' d\Gamma'. \quad (5.15)$$

Defining

$$\epsilon_{\varpi}(r; \omega, u) = \int_{-\infty}^{\infty} \epsilon(t; r; \omega, u) e^{i\varpi t} dt \quad (5.16)$$

we can rewrite Eq. (5.14) in frequency space as

$$i\partial_r \epsilon_{\varpi} \approx \left\{ -\eta\omega + (\lambda - \varpi) \left[1 + \left(\frac{R}{r} \right)^2 \frac{u}{2} \right] + C \right\} \epsilon_{\varpi} - \frac{\mu}{2} \int (u + u')(\rho'_{ee} - \rho'_{xx})g' \epsilon'_{\varpi} d\Gamma'. \quad (5.17)$$

We note that frequency ϖ in the above equations represents the temporal variation of the neutrino flavor quantum state at given radius r , and it shall not be confused with the vacuum oscillation frequency ω which is determined by the energy of the neutrino.

We also note that the starting point of collective oscillations is determined by the comparison of the dispersion in each term of the neutrino propagation Hamiltonian

in Eq. (4.3) with the overall strength of the neutrino potential. The spreads in the vacuum Hamiltonian H_{vac} and the neutrino potential $H_{\nu\nu}$ are dominated by variations in vacuum oscillation frequency ω and trajectory parameter u , respectively. Therefore, we have taken $v_u \approx 1$ for these terms in Eq. (5.17) as in (Esteban-Pretel et al. 2008). For the matter potential H_{mat} , however, the lowest order term of $v_u^{-1}H_{\text{mat}}$ in the large-radius expansion is the same for all neutrinos and does not suppress collective oscillations (Duan et al. 2006d). In Eq. (5.17) we have included its next-order term which can suppress collective oscillations if a very large matter potential is present (Esteban-Pretel et al. 2008).

Eq. (5.17) is the same as that for neutrino oscillations in the stationary Bulb model except with replacement $\lambda \rightarrow \lambda - \varpi$. The flavor-stability analysis of this model is very similar to the stability analysis that we did in the previous chapter and has been carried out in details by Banerjee et al. (2011) which we shall not repeat here. The essence of this analysis is to find out all the collective oscillation solutions to Eq. (5.17) which are of the form

$$\epsilon_{\varpi} = Q_{\varpi} e^{-i\Omega_{\varpi} r}, \quad (5.18)$$

where $Q_{\varpi}(\omega, u)$ is independent of r , and $\Omega_{\varpi}(\lambda, \mu)$ is the collective oscillation frequency. If

$$\kappa_{\varpi} = \text{Im}(\Omega_{\varpi}) \quad (5.19)$$

is positive, there exists a flavor instability, and ϵ_{ϖ} will grow exponentially in terms of r which can lead to significant flavor transformation. If there exist multiple unstable modes, the unstable mode with the largest exponential growth rate κ^{max} will eventually dominate.

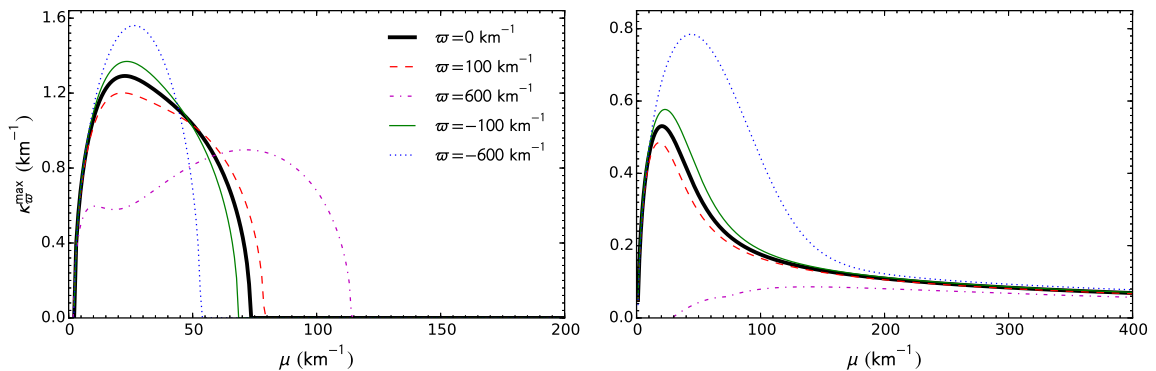


Figure 5.2: The maximum exponential growth rates κ^{\max} of a few Fourier modes with various frequencies ϖ (as labeled) as functions of the strength of the neutrino potential μ in the neutrino Bulb model. The left panel uses a single-energy spectrum (Mirizzi 2015), and the right panel a continuous spectrum (Duan and Friedland 2011, Banerjee et al. 2011). The peaks of $\kappa_{\varpi=0}^{\max}(\mu)$ correspond to distances 107 km (left) and 149 km (right) from the center of the supernova. The matter density is assumed to be not large enough to suppress collective neutrino oscillations. Figure adapted from (Abbar and Duan 2015).

5.3 Results and discussion

We analyzed the flavor instabilities in the time-dependent Bulb model with two sets of neutrino spectra. In the first case we assume the same single-energy spectrum as by Mirizzi (2015). In this case, all neutrinos and antineutrinos have the same vacuum oscillation frequency $\omega_0 = 0.68 \text{ km}^{-1}$ and the number fluxes are $N_{\nu_e} = 1.25 \times 10^{56} \text{ s}^{-1}$, $N_{\bar{\nu}_e} = 8.32 \times 10^{55} \text{ s}^{-1}$ and $N_{\nu_x/\bar{\nu}_x} = 5.20 \times 10^{55} \text{ s}^{-1}$. In the second case we assume the same Fermi-Dirac spectra as in Refs. (Duan and Friedland 2011, Banerjee et al. 2011) which have degeneracy parameters $\eta_{\nu_e} = 3.9$, $\eta_{\bar{\nu}_e} = 2.3$ and $\eta_{\nu_x/\bar{\nu}_x} = 2.1$, average energies $\langle E_{\nu_e} \rangle = 9.4 \text{ MeV}$, $\langle E_{\bar{\nu}_e} \rangle = 13.0 \text{ MeV}$, $\langle E_{\nu_x/\bar{\nu}_x} \rangle = 15.8 \text{ MeV}$, and luminosities $L_{\nu_e} = 4.1 \times 10^{51} \text{ erg s}^{-1}$, $L_{\bar{\nu}_e} = 4.3 \times 10^{51} \text{ erg s}^{-1}$, $L_{\nu_x/\bar{\nu}_x} = 7.9 \times 10^{51} \text{ erg s}^{-1}$. In both cases we assume a neutrino sphere of radius $R = 10 \text{ km}$ and mass-squared difference $\Delta m^2 = -2.4 \times 10^{-3} \text{ eV}^2$, i.e. with an inverted neutrino mass hierarchy.

Chapter 5. Neutrino Flavor Instabilities in Time-Dependent Bulb Model

In Fig. 7.4 we plot κ^{\max} for a few frequency modes as functions of neutrino potential strength μ [see Eq. (5.11)] assuming that the matter density is not large enough to suppress collective oscillations (i.e. $v^{-1}\lambda \approx \lambda$ is valid). In both cases both the instability region and κ^{\max} are about the same for the frequency modes with $|\varpi| \lesssim 100 \text{ km}^{-1}$. This is not a coincidence. Compared to the stationary model, the time-dependent model has a new term in Eq. (5.17)

$$\frac{\varpi}{v_u} \approx \varpi + \left(\frac{R}{r}\right)^2 \frac{u\varpi}{2}. \quad (5.20)$$

The first term in the above equation changes only the real part of the collective oscillation frequency Ω_ϖ and has no impact on the flavor stability. The second term depends on the neutrino trajectory and has a spread $\Delta\varpi \sim (R/r)^2|\varpi|$. It becomes important only when

$$\Delta\varpi \gtrsim \omega_0, \quad (5.21)$$

where $\omega_0 \sim 1 \text{ km}^{-1}$ is the typical vacuum oscillation frequency (and also the spread of ω) of supernova neutrinos with the atmospheric mass-squared difference. In both cases collective neutrino oscillations occur at $r \sim 10R$ which implies that the stability condition of the frequency modes with $|\varpi| \lesssim 100 \text{ km}^{-1}$ are about the same.

The above arguments can be generalized to the scenarios where collective oscillations occur close to the neutrino sphere (but not too close so that $r - R \ll R$) because of, e.g., spatial inhomogeneous oscillation modes (Duan and Shalgar 2015, Mirizzi et al. 2015, Chakraborty et al. 2016, Abbar et al. 2015b) or different angular distributions for neutrino fluxes in different flavors (Mirizzi 2013, Sawyer 2016). In these scenarios the spread in $v_u^{-1}\varpi$ is of the same order as ϖ itself, and the frequency modes with $|\varpi| \lesssim 1 \text{ km}^{-1} \approx (3 \mu\text{s})^{-1}$ should have the same stability condition. These arguments also apply in the presence of a large matter density because the comparison between $\Delta\varpi$ and ω_0 is not affected by the presence of the matter potential.

We note that there exists a causality constraint in the time-dependent Bulb

Chapter 5. Neutrino Flavor Instabilities in Time-Dependent Bulb Model

model. Suppose that there is a temporary change in the neutrino fluxes on one side of the neutrino sphere which lasts for a time interval Δt . Because it takes at least $\Delta t' \sim R$ for this change to propagate throughout the proto-neutron star, the assumption of the spherical symmetry implies that the inequality $\Delta t \gtrsim R$ must hold. Therefore, only the oscillation modes of frequencies

$$\varpi \lesssim R^{-1} \sim (10 \text{ km})^{-1} \approx (30 \mu\text{s})^{-1} \quad (5.22)$$

are allowed in the spherical Bulb model. From the above discussion we conclude that there should be no significant difference between the flavor stability conditions in the time-dependent and stationary Bulb models. For more general time-dependent supernova models, collective neutrino oscillations should occur at approximately the same radius as in the corresponding stationary models unless there exist very rapid variations in local physical conditions on the timescales of a few microseconds or shorter.

Meanwhile, the fact that the frequency modes with $|\varpi| \lesssim 1 - 100 \omega_0$ all have similar instability regions also implies that the time-translation symmetry can indeed be broken spontaneously by collective neutrino oscillations in the Bulb model, and that neutrino oscillations can have a strong time dependence once collective oscillations begin. As a result, there may exist qualitative differences between neutrino oscillations in time-dependent and stationary supernova models.

Chapter 6

Neutron Stars

Neutron was discovered in 1932 (Chadwick 1932). A year after this discovery, Baade and Zwicky pointed out the possibility of neutron stars while they were studying the supernova explosion (Baade and Zwicky 1934). They came up with the idea that the energy released in a supernova explosion is essentially the gravitational binding energy of a very compact object which is made up of neutrons. The first calculation of the structure of neutron stars was carried out in 1939 by Oppenheimer and Volkoff (Oppenheimer and Volkoff 1939) in which they studied the hydrodynamical stability of a spherical compact object in general relativity. However, since there was no observation confirming their existence, the idea of neutron stars did not attract much attention for almost 30 years after Baade and Zwicky proposal.

In 1967, Hewish and Bell detected a radio signal with a pulsing period of 1.337 seconds (Hewish et al. 1968). Soon it was realized that pulsars are rotating neutron stars with very large magnetic fields. Pulsar signal comes from the strong electromagnetic radiation which is emitted along the magnetic axis of the neutron star and beams toward the earth once in every rotation. It was after this discovery that the idea of the neutron star became popular. Today, almost 2000 pulsars are known.

In this chapter, we briefly review the physics of neutron stars. Throughout this chapter, we adopt the physical units with $\hbar = c = G = 1$.

6.1 Mass and radius of the neutron star

A simple study of the structure of neutron stars in general relativity can be done by considering the Einstein equation in the spherical symmetry. The resulting equations were first studied by Tolman, Oppenheimer and Volkoff (Oppenheimer and Volkoff 1939) (TOV equations) and can be written as

$$\frac{dm}{dr} = 4\pi r^2 \rho, \quad (6.1a)$$

$$\frac{dP}{dr} = -\frac{\rho m}{r^2} \left(1 + \frac{P}{\rho}\right) \left(1 + \frac{4\pi P r^3}{m}\right) \left(1 - \frac{2m}{r}\right)^{-1}, \quad (6.1b)$$

$$\frac{d\Phi}{dr} = -\frac{1}{\rho} \frac{dP}{dr} \left(1 + \frac{P}{\rho}\right)^{-1}. \quad (6.1c)$$

Here r is the radial distance in spherical coordinate, Φ is the gravitational potential, P is the pressure, ρ is the energy density, and $m(r)$ is the gravitational mass of the matter inside the sphere of radius r . In the cold matter when the temperature is negligible, P and ρ are related through an equation of state (EOS) of the form

$$P = P(\rho). \quad (6.2)$$

The total mass of the neutron star is given by

$$M = \int_0^R 4\pi r^2 \rho dr. \quad (6.3)$$

It is important to note that M includes the contribution from all the sources of energy and is not just the rest mass of the star. The Newtonian limit can be achieved if $P \ll \rho$ and $m \ll r^1$.

¹This condition implies that the star's radius is much larger than the schwarzschild radius, $r_s = 2M$.

Chapter 6. Neutron Stars

Eq. (6.1) has been solved for a configuration composed of a pure, non-interacting neutron gas by Oppenheimer and Volkoff. They found the maximum mass for this configuration to be $M_{\max} \simeq 0.7M_{\odot}$. In their calculations, the maximum-mass neutron star has the radius $R \simeq 9.6$ km and the central density $\rho_c \simeq 5 \times 10^{15}$ g cm⁻³.

A more reasonable EOS results from a gas consisting of a mixture of electrons, protons and neutrons in equilibrium. In this case, the neutrons are present only when the density is larger than about 1.2×10^7 g cm⁻³. This is because, for smaller densities, any existing neutron can decay through the beta-decay process

$$n \rightarrow e + p + \bar{\nu}_e. \quad (6.4)$$

For higher densities, the fermi energy of electron is sufficient to produce a neutron in the process

$$e + p \rightarrow n + \bar{\nu}_e. \quad (6.5)$$

The resulted EOS is very similar to the one of the pure neutron gas. The maximum mass was found to be $M_{\max} \simeq 0.72 M_{\odot}$ with $R \simeq 8.8$ km and $\rho_c \simeq 5.8 \times 10^{15}$ g cm⁻³.

For more realistic EOS'es, the maximum mass of the neutron star depends on the EOS at supra-nuclear densities which is subject to significant uncertainties (Lattimer and Prakash 2016). However, one can still put some constraints on the maximum mass of the neutron star without knowing the details of the EOS at very large densities. As was pointed out by Rhoades Jr and Ruffini (1974) (see also (Koranda et al. 1997)) one can use two very general and physical conditions to limit the mass of neutron stars.

The first condition is the condition of the *microscopic stability* in which the pressure must increase monotonically with ρ , i.e.

$$\frac{dP}{d\rho} \geq 0. \quad (6.6)$$

Chapter 6. Neutron Stars

This condition implies the stability of the matter. If it is violated, the neutron star will collapse.

The other general condition that can be used to limit the maximum mass of the neutron star is the *causality* which implies

$$\frac{dP}{d\rho} = c_s^2 \leq 1. \quad (6.7)$$

This condition states that the velocity of sound in the medium must be smaller than (or equal to) the speed of light.

Having these conditions in mind, one can find the stiffest EOS at supra-nuclear densities that maximizes the mass of the neutron star. A simple choice used by Rhoades Jr and Ruffini (1974) is

$$P = P_0 + (\rho - \rho_0) \quad \text{at} \quad \rho \geq \rho_0, \quad (6.8)$$

where ρ_0 is a density (with the value of about nuclear density) above which there exists large uncertainty for the equation of state and P_0 is the corresponding pressure. Rhoades and Ruffini used $\rho_0 = 4.6 \times 10^{14} \text{ g cm}^{-3}$ in their calculations. Using the EOS in Eq. (6.8) at supra-nuclear densities, the maximum mass was found to be

$$M_{\text{max}} \simeq \left(\frac{\rho_0}{4.6 \times 10^{14} \text{ g cm}^{-3}} \right)^{-1/2} 3.2 M_{\odot}. \quad (6.9)$$

It should be noted that the reason for the existence of a maximum mass is different in Newtonian physics and general relativity. In Newtonian physics, there exists a maximum mass only when the EOS is too soft (e.g., the EOS of relativistic particles). In particular, for the EOS of non-relativistic particles there is no limit on the mass of the star. On the other hand, In general relativity the existence of the maximum mass comes from the nonlinearity of the TOV equations and there is a maximum mass even for very stiff EOS'es.

Chapter 6. Neutron Stars

For a given EOS, Eq. (6.1) can be solved for a given central density ρ_c as the initial condition. Then one can find the mass-radius curve which is different for different EOS'es (see Fig. 6.1). To develop some insight into the nature of the solutions of the structure equations, let us consider Eq. (6.1) in the Newtonian limit:

$$\begin{aligned}\frac{dm}{dr} &= 4\pi r^2 \rho, \\ \frac{dP}{dr} &= -\frac{\rho m}{r^2}, \\ \frac{d\Phi}{dr} &= \frac{m}{r^2}.\end{aligned}\tag{6.10}$$

Assuming a polytropic EOS of the form

$$P = K\rho^\gamma,\tag{6.11}$$

one can find the mass of the star as a function of its radius in the Newtonian limit to be (Kippenhahn et al. 1990)

$$M = \xi R^{(4-3\gamma)/(2-\gamma)},\tag{6.12}$$

where ξ is a constant that depends on γ . For the low mass neutron stars where the densities are relatively low, the neutron star is supported mostly by the pressure of the degenerate relativistic electron gas. In this case $\gamma \simeq 4/3$, and one finds

$$M = \text{constant}.\tag{6.13}$$

In other words, the mass of a low mass neutron star almost remains constant with respect to the radius. For high mass neutron stars, however, it is expected that a significant part of the pressure is due to the matter at densities larger than the nuclear saturation density $n_s \simeq 0.16 \text{ fm}^{-3}$. At these densities, almost all theories for dense matter suggest that $\gamma \simeq 2$ (Lattimer and Prakash 2016). For this value of γ , one finds that

$$R = \text{constant}.\tag{6.14}$$

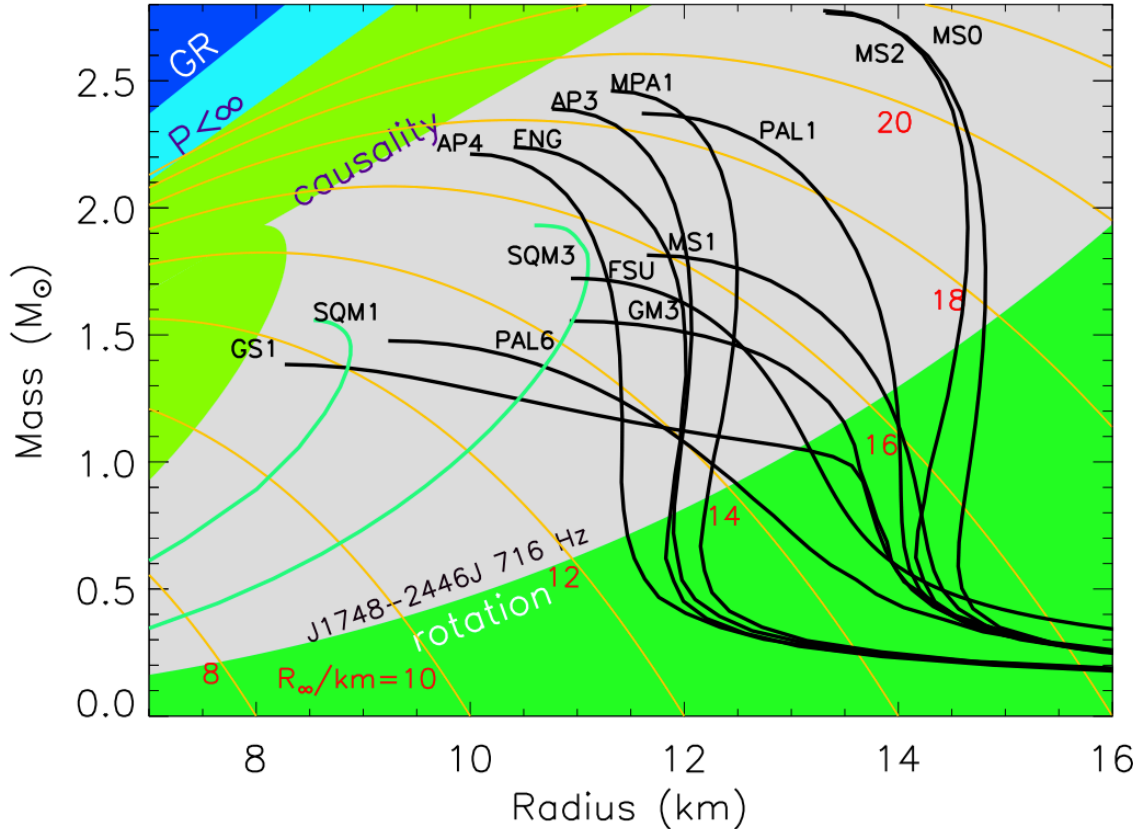


Figure 6.1: Mass-radius curves for a variety of popular equations of state. The bright green region at the top left is excluded by causality. The dark green region at the bottom is excluded by the most rapidly spinning pulsar. Black curves come from different equations of state for hadronic matter and the green curves are from equations of state of quark matter. R_∞ is defined as $R_\infty = R\sqrt{1 - 2\beta}$ where $\beta = GM/R$. Reprinted from [Phys. Rep., 621, J. M. Lattimer & M. Prakash, The equation of state of hot, dense matter and neutron stars, 127](#) Copyright 2016, with permission from Elsevier (Ref. (Lattimer and Prakash 2016)).

The interior of a neutron star can be divided into five important regions (Lattimer and Prakash 2016) (see also Figs. 6.2 and 6.3). The outermost region is the *atmosphere* which is only ~ 1 cm thick. In spite of its small thickness, this region is very important since it controls the observed energy spectra of the radiation from the

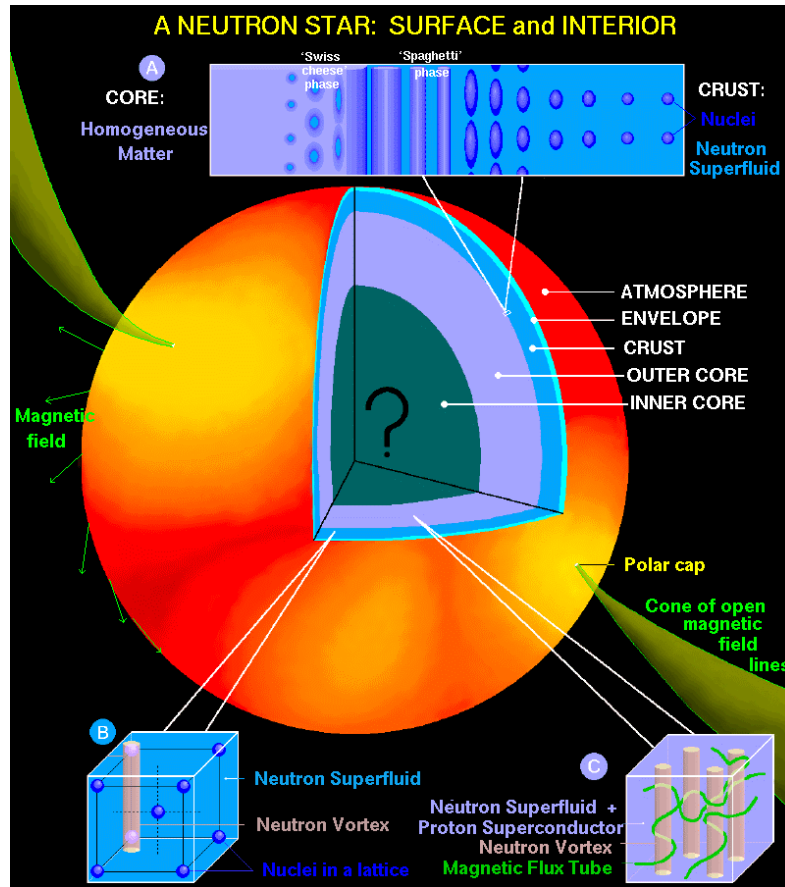


Figure 6.2: Schematic representation of the structure of a neutron star. Figure adapted from Page and Reddy (2006).

neutron star. The next layer is the *envelope* which controls the effective temperature of the neutron star. Below the envelope is the *crust* which is a region composed of nuclei in a Coulomb lattice. This region itself can be divided into two parts: the outer crust which is a lattice composed of nuclei with $Z \simeq 56$ and the inner crust with ρ in the range $4 \times 10^{11} \text{ g cm}^{-3} - 10^{14} \text{ g cm}^{-3}$. The nuclei in the inner crust are more massive and neutron rich. Due to the competition between the Coulomb and surface energies, nuclei are likely deformed in the inner crust. At higher densities, this deformation leads to the formation of the so-called pasta-phase. Moreover, in

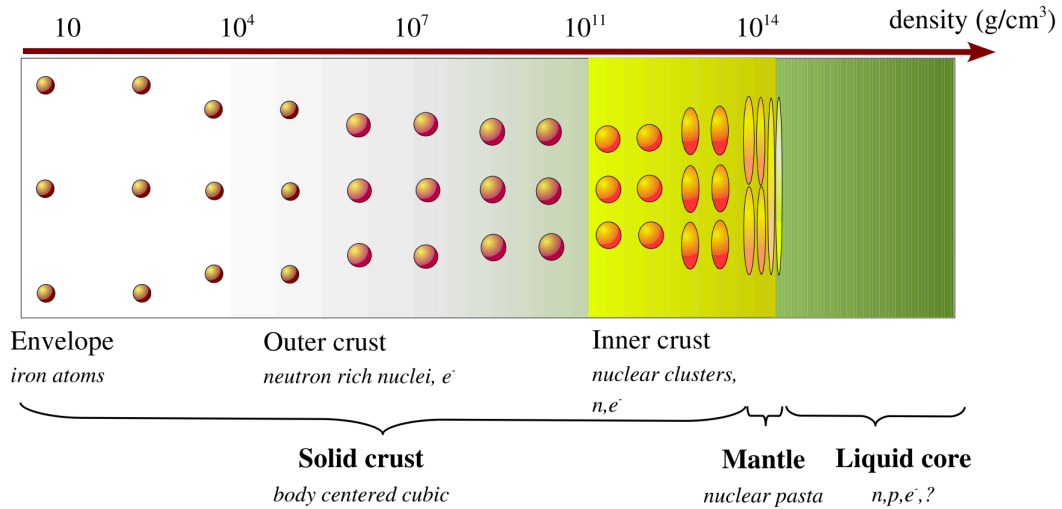


Figure 6.3: Schematic picture of the composition of the neutron star along the density axis. Figure adapted from (Chamel and Haensel 2008).

the inner crust there exist free neutrons which have dripped out of the nuclei. At the boundary of the inner crust and the core, the density is approximately $10^{14} \text{ g cm}^{-3}$, and the inhomogenous phase of the nuclei is replaced by a homogenous phase of the nucleons in the *outer core*. The innermost region is the *inner core* with a composition that is mostly unknown. There are a number of candidate phases for the matter inside the inner core, from a phase which is mostly composed of nucleons to a phase of deconfined quarks.

6.2 Cooling of the neutron star

Neutron stars are born with very high internal temperatures ($T \gtrsim 10^{11} \text{ K}$). Its surface temperature decreases to a few 10^6 K after a few hundreds of years and remains in the vicinity of this value for a few hundred thousands of years. For these temperatures, i.e. $T \simeq 0.1 - 1 \text{ KeV}$ we expect a thermal radiation in the x-ray band.

Chapter 6. Neutron Stars

The cooling history of a neutron star is very sensitive to the physics of its interior. Therefore by studying the thermal evolution of the neutron star and comparing the theoretical predictions with observations, we can develop our understanding of the high-density matter inside the neutron star. In this section we discuss briefly the equations that govern the thermal evolution of a neutron star.

Since the structure of the neutron star can affect its thermal evolution, the equations that govern the thermal evolution of the neutron star is coupled to its structure equations. The physics of the thermal structure of the neutron star can be described by six ordinary differential equations (see, e.g., (Gudmundsson et al. 1983)). The first three equations are the structure equations in Eq. (6.1). The heat transport equation is given by

$$\frac{d(Te^\Phi)}{dr} = -\frac{3\kappa\rho}{16\sigma T^3} \frac{L_d}{4\pi r^2} e^\Phi e^\Lambda, \quad (6.15)$$

where σ is the Stefan-Boltzmann constant, L_d is the luminosity due to thermal conduction and radiation, κ is the total opacity of the stellar mater, e^Φ is the redshift factor, and

$$e^\Lambda = \left(1 - \frac{2m}{r}\right)^{-1/2}. \quad (6.16)$$

is the relativistic length correction factor. The next equation is the equation that governs the neutrino luminosity L_ν :

$$\frac{d(L_\nu e^{2\Phi})}{dr} = \epsilon_\nu e^{2\Phi} 4\pi r^2 e^\Lambda, \quad (6.17)$$

where ϵ_ν is the neutrino emissivity per unit volume. At $T \lesssim 10^9$ K, one can ignore the transport of neutrinos inside the neutron star because the neutrino mean free path is larger than the radius of the neuron star (Shapiro and Teukolsky 2008). If there is no source of internal heating, the energy conservation gives

$$\frac{d(Le^{2\Phi})}{dr} = -c_v \frac{dT}{dt} 4\pi r^2 e^\Lambda, \quad (6.18)$$

Chapter 6. Neutron Stars

where L is the total luminosity $L = L_d + L_\nu$, c_v is the specific heat per unit volume, and t is the time measured by an observer at $r = \infty$.

In the Newtonian limit, the equations of the thermal evolution can be written as

$$\frac{dL_d}{dr} + \epsilon_\nu = -c_v \frac{dT}{dt} 4\pi r^2 \quad (6.19)$$

and

$$\frac{dT}{dr} = -\frac{3\kappa\rho}{16\sigma T^3} \frac{L_d}{4\pi r^2}. \quad (6.20)$$

From these equations, one can find the characteristic time-scale of the neutron star cooling

$$\tau_{th} \approx \frac{C_V l^2}{\kappa}, \quad (6.21)$$

where l is the length-scale of temperature variations, and C_V is the total heat capacity of the entire neutron star.

Since the thermal conductivity is very large at large matter densities, the interior of the neutron star is almost isothermal except for a very narrow region near the surface where there is a very large temperature gradient. To find a relation between the surface and interior temperatures of a neutron star, Gudmundsson et al. (1983) divided the neutron star into two regions. The inner region has a larger density ($\rho \geq 10^{10} \text{ g cm}^{-3}$) and includes the core (and a part of the crust). The outer region has a smaller density ($\rho \leq 10^{10} \text{ g cm}^{-3}$) and includes the atmosphere, the envelope and a part of the outer crust. In their calculations it was assumed that (see (Richardson et al. 1982)) for a neutron star more than a few tens of years old, the temperature in the outer region has fallen below 10^9 K so that this region is in a quasi-stationary state. This means that the right-hand side of Eq. (6.18) becomes zero and

$$L e^{2\Phi} \simeq \text{constant} \quad (6.22)$$

Chapter 6. Neutron Stars

within the outer region. It was shown that the terms of order P/ρ can be ignored in this region with an accuracy better than 0.1% and that the e^Φ and e^Λ terms are constant in the outer region with an accuracy better than 0.5%. With these simplifications for the matter in the outer region, Gudmundsson et al. (1983) came up with a simple equation that governs the variation of the temperature for the outer region

$$\frac{dT}{dP} = \frac{3}{16} \frac{\kappa}{T^3} \frac{T_s^4}{g_s}, \quad (6.23)$$

where

$$g_s = \frac{M}{R^2} e^{\Lambda_s} \quad (6.24)$$

is the surface gravity of the neutron star, and subscript “s” signifies the values at the surface of the neutron star. This equation determines the thermal structure of the outer region and can be solved for the interior temperature of the neutron star with the given surface temperature.

To obtain some insight into the neutron star cooling time scales, we will ignore the thermal structure inside the neutron star, and we will assume that the neutron star is isothermal to a very good approximation. In the Newtonian limit, The thermal evolution of the neutron star is governed by

$$\frac{dU}{dt} = C_V \frac{dT}{dt} = -(L_\nu + L_\gamma), \quad (6.25)$$

where L_ν and L_γ are total neutrino and photon luminosities, respectively. If the neutron star can be approximated as a blackbody, its total photon luminosity is related to the effective surface temperature by

$$L_\gamma = 4\pi R^2 \sigma T_s^4. \quad (6.26)$$

To a very good approximation, one can assume that the thermal energy of the neutron star resides almost entirely in the degenerate fermion gas. The heat capacity of a

Chapter 6. Neutron Stars

fermion gas with N particles at temperature T is given by (Shapiro and Teukolsky 2008)

$$C_V \simeq \pi^2 \frac{(1+x^2)^{1/2}}{x^2} \frac{NT}{m}, \quad (6.27)$$

where m is the mass of the particle, and $x = p_F/m$ with p_F being the Fermi momentum of the particle. With this expression for C_v , one can find the neutron star cooling time scale if the neutrino cooling process is known. For example, if the neutrino pair Bremsstrahlung is the dominant cooling process, one has (Shapiro and Teukolsky 2008)

$$L_\nu \simeq 5 \times 10^{39} \text{ erg s}^{-1} \left(\frac{M_{\text{crust}}}{M_\odot} \right) \left(\frac{T}{10^9 \text{ K}} \right)^6, \quad (6.28)$$

and the neutrino pair Bremsstrahlung cooling time scale is

$$\tau_c \simeq 2 \text{ yr} \left(\frac{M_{\text{crust}}}{M_\odot} \right) \left(\frac{\rho}{2.8 \times 10^{14} \text{ g cm}^{-3}} \right)^{-2/3} \left(\frac{T}{10^9 \text{ K}} \right)^{-4}, \quad (6.29)$$

where ρ is the average density of the neutron star. Depending on the cooling mechanism, the cooling time scale ranges from a few seconds to several years.

Chapter 7

Thermal Conductivity of the Neutron Star Crust

In the previous chapter, we mentioned that the observations of the cooling of neutron stars can provide us with valuable information of the physics of the neutron stars interior. In particular, observations of transient phenomena in accreting neutrons stars including magnetars (Eichler and Cheng 1989, Rutledge et al. 2002) have motivated recent attempts to model the thermal evolution of the neutron star crust (see (Shternin et al. 2007, Brown and Cumming 2009, Page and Reddy 2012; 2013)). These studies have shown that the thermal conductivity of the crust plays a very important role in shaping the temporal structure of the x-ray emission from these systems. In this chapter we will study the thermal conductivity of the outer crust of the neutron star where the typical densities are in the range of $10^8 - 10^{11} \text{ g cm}^{-3}$ and temperatures are expected to be in the range of $10^7 - 10^9 \text{ K}$.

7.1 Thermal conductivity of the outer crust

In the simplest scenario the outer crust at given density is composed of cold catalyzed matter of a single ion species. The mass number A and charge Z of the ions are density dependent and are determined by minimizing the total energy of the system. The ground state of such matter is a strongly correlated one component plasma (OCP) with bare nuclei immersed in a degenerate and weakly coupled electron gas. The characteristic energy of the electron is set by its Fermi momentum

$$\begin{aligned} p_F &= (3\pi^2 n_e)^{1/3} \\ &\simeq (25 \text{ fm})^{-1} \left(\frac{Z}{30}\right)^{1/3} \left(\frac{A}{80}\right)^{-1/3} \rho_{10}^{1/3}, \end{aligned} \quad (7.1)$$

where n_e is the number density of electrons, and ρ_{10} is the mass density in units of $10^{10} \text{ g cm}^{-3}$. For the densities of interest in the outer crust, which are typically in the range of $10^8 - 10^{11} \text{ g cm}^{-3}$, p_F is much larger than electron mass m_e , and it is a good approximation to treat electrons as ultra-relativistic. In contrast, ions are heavy and correlated. One characteristic energy is set by the ion plasma frequency

$$\begin{aligned} \Omega_P &= \left(\frac{4\pi Z^2 e^2 n_I}{M}\right)^{1/2} \\ &\approx (2.9 \times 10^8 \text{ K}) \left(\frac{Z}{30}\right) \left(\frac{A}{80}\right)^{-1} \rho_{10}^{1/2}, \end{aligned} \quad (7.2)$$

where $n_I = n_e/Z$ is the ion density, $M \approx Am_p$ is the mass of the ion with m_p being the proton mass, and $e^2 \approx 1/137$ is the fine structure constant in natural units.

The typical Coulomb energy is of order $Z^2 e^2/a$, where

$$a = \left(\frac{4\pi n_I}{3}\right)^{-1/3} \approx (147 \text{ fm}) \left(\frac{A}{80}\right)^{1/3} \rho_{10}^{-1/3} \quad (7.3)$$

is the inter-ion distance. The temperature T provides a measure of the “extractable” kinetic energy or the thermal energy of the ions. The ratio between the Coulomb energy and the thermal energy of the ions is a measure of the importance of interactions

in the plasma and defines the dimensionless Coulomb parameter

$$\Gamma = \frac{Z^2 e^2}{aT}. \quad (7.4)$$

In a weakly coupled plasma $\Gamma \ll 1$, and Coulomb interaction can be studied with the perturbation theory. Numerical simulations of the OCP have shown that ions crystallize into a solid state when $\Gamma > \Gamma_m \approx 175$ (Slattery et al. 1980; 1982, Jones and Ceperley 1996). The melting temperature of the solid

$$T_m = \frac{Z^2 e^2}{a\Gamma_m} \approx 2.0 \Omega_P \left(\frac{Z}{30}\right) \left(\frac{A}{80}\right)^{2/3} \rho_{10}^{-1/6} \quad (7.5)$$

can be correspondingly defined. We note that the electron screening modifies the Coulomb potential generated by the ion at large distances. The modified potential is

$$V(r) = \frac{Ze}{r} e^{-r k_{\text{TF}}}, \quad (7.6)$$

where

$$k_{\text{TF}} = \left(4\pi e^2 \frac{\partial n_e}{\partial \mu_e}\right)^{1/2} \xrightarrow{p_F \gg m_e} \sqrt{\frac{4e^2}{\pi}} p_F \approx (1.7a)^{-1} \left(\frac{Z}{30}\right)^{1/3} \quad (7.7)$$

is the Thomas-Fermi (screening) momentum, and $\mu_e = \sqrt{m_e^2 + p_F^2}$ is the electron Fermi energy. Because $k_{\text{TF}} a < 1$ for the densities of interest, screening will not greatly alter the nearest neighbor ion-ion interaction, and the Coulomb parameter of the OCP without screening continues to provide a reasonable measure of the strength of interactions and the melting temperature. In this chapter we have chosen to present results at fiducial densities 10^{10} and 10^{11} g cm⁻³, labelled as LD and HD, respectively. The chemical compositions in these two cases are chosen according to (Page and Reddy 2012) for catalyzed matter in the outer crust. We list the physical conditions of the two cases in Table 7.1.

The information about inter-particle correlations and their time evolution is contained in the dynamic structure function and is given by (see, e.g., (Ashcroft and

Chapter 7. Thermal Conductivity of the Neutron Star Crust

Name	Lattice	ρ	Ion	a	Ω_P	T_m	p_F^{-1}	k_{TF}^{-1}	k_D^{-1}
LD	BCC	10^{10}	${}^{84}_{34}\text{Se}$	149	0.32	0.75	24	249	62
HD	BCC	10^{11}	${}^{80}_{28}\text{Ni}$	68	0.87	1.11	12	121	28

Table 7.1: Key parameters for cold catalyzed matter in neutron star crust at two fiducial densities. The compositions are chosen according to (Page and Reddy 2012). Here a , p_F^{-1} , k_{TF}^{-1} and k_D^{-1} are all in units of fm and Ω_P and T_m are in 10^9 K.

(Mermin 1976))

$$S(\omega, \mathbf{q}) = \frac{1}{N} \sum_{i,j=1}^N e^{-i\mathbf{q}\cdot(\mathbf{R}_i-\mathbf{R}_j)} \int \frac{dt}{2\pi} e^{i\omega t} \langle e^{i\mathbf{q}\cdot\mathbf{u}_j(0)} e^{-i\mathbf{q}\cdot\mathbf{u}_i(t)} \rangle_T, \quad (7.8)$$

where N is the total number of ions in the crystal, \mathbf{R}_i is the equilibrium position of the ion on the i 'th site, $\mathbf{u}_i(t)$ is the displacement of this ion at time t , and $\langle \dots \rangle_T$ denotes the thermal average.

Since electrons are relativistic, weakly coupled and very degenerate, they dominate the thermal conductivity of the neutron star crust. The electron thermal conductivity κ is mainly limited by electron-ion scattering and can be written as

$$\kappa = \frac{\pi^2 T n_e}{3 \varepsilon_F \nu_\kappa}, \quad (7.9)$$

where $\varepsilon_F \approx p_F$ is the electron Fermi energy, and the effective collision rate is (Flowers and Itoh 1976)

$$\nu_\kappa = \frac{2}{3} \frac{\varepsilon_F}{Z(2\pi)^3} \int_0^{2p_F} dq q^3 |v(q)|^2 S'_\kappa(q). \quad (7.10)$$

In the above expression

$$|v(q)|^2 = e^2 |V(q)|^2 \left(1 - \frac{q^2}{4p_F^2} \right) \quad (7.11)$$

is the square of the scattering matrix element for electron-ion interaction with momentum exchange \mathbf{q} , and the screened Coulomb potential generated by the ion in momentum space is

$$V(q) = \frac{4\pi Z e}{\epsilon(q) q^2}, \quad (7.12)$$

where

$$\epsilon(q) = 1 + \frac{k_{\text{TF}}^2}{q^2} \quad (7.13)$$

is the static dielectric function in the Thomas-Fermi approximation. The effects due to ion-ion correlations on electron scattering are included in Eq. (7.10) through

$$S'_\kappa(q) = \int_{-\infty}^{\infty} d\omega \langle S'(\omega, \mathbf{q}) \rangle_{\hat{\mathbf{q}}} w_\kappa(\omega/T, q), \quad (7.14)$$

where $S'(\omega, \mathbf{q})$ is the inelastic part of the dynamic structure function, $\langle \dots \rangle_{\hat{\mathbf{q}}}$ is the average over the direction of unit vector $\hat{\mathbf{q}} = \mathbf{q}/q$, and

$$w_\kappa(z = \omega/T, q) = \frac{z}{e^z - 1} \left[1 + \frac{z^2}{\pi^2} \left(\frac{3p_{\text{F}}^2}{q^2} - \frac{1}{2} \right) \right]. \quad (7.15)$$

We note that the elastic Bragg scattering does not contribute to the conductivity because it has been accounted for in the ground state which leads to the electronic band structure.

Because the response at high frequency $|\omega| \gg \Omega_{\text{P}}$ cannot involve collective motion of the ions, we expect that most of the strength of the dynamic response will reside at energies that are comparable to Ω_{P} . Therefore, when $T \gtrsim \Omega_{\text{P}}$ it is a good approximation to retain only the leading terms of $w_\kappa(z, q)$ in $z = \omega/T$ in the integrand in Eq. (7.14), and the static approximation $S'_\kappa(q) \approx S'(q)$ is valid, where

$$S'(q) = \int_{-\infty}^{\infty} d\omega \langle S'(\omega, \mathbf{q}) \rangle_{\hat{\mathbf{q}}}, \quad (7.16)$$

is the inelastic part of the static structure function. At very low temperature $T \ll \Omega_{\text{P}}$, however, the exponential factor $1/(e^{-\omega/T} - 1)$ in $w_\kappa(z, q)$ dominates. In this limit the static approximation breaks down, and $S'_\kappa(q) \ll S'(q)$. Between these two temperature limits two competing factors in $w_\kappa(z, q)$ dominate in different ranges of q . For large-angle scattering (with large q values) the exponential factor still dominates, and $S'_\kappa(q) < S'(q)$. But for small-angle scattering (with small q values) the factor p_{F}^2/q^2 can dominate, and $S'_\kappa(q) > S'(q)$.

7.2 Phonon spectrum and dynamical response

At low temperature the characteristic distance scale for ion motion in lattice is

$$\lambda_I = \left(\frac{1}{2M\Omega_P} \right)^{1/2} \approx (3.2 \text{ fm}) \left(\frac{Z}{30} \right)^{-1/2} \rho_{10}^{-1/4}, \quad (7.17)$$

which is much shorter than the inter-ion distance a . Under these conditions the restoring force on the ion is quadratic in the displacement $\mathbf{u}_i(t)$, and the detailed phonon spectrum can be calculated by using the dynamic matrix (see, e.g., (Carr 1961, Ashcroft and Mermin 1976))

$$D(\mathbf{k}) = 2 \sum_{i=1}^N \sin^2 \left(\frac{\mathbf{k} \cdot \mathbf{R}_i}{2} \right) \left[\frac{\partial^2 V(\mathbf{x})}{\partial \mathbf{x} \partial \mathbf{x}^T} \right]_{\mathbf{x}=\mathbf{R}_i}. \quad (7.18)$$

The phonon frequencies $\omega_s(\mathbf{k})$ ($s = 1, 2, 3$) are obtained by solving the eigenvalue equation $M\omega_s^2(\mathbf{k}) - D(\mathbf{k}) = 0$, and the corresponding normalized eigenvectors $\hat{\mathbf{e}}_s(\mathbf{k})$ are the phonon polarization vectors. In the long wavelength limit, phonons have a linear dispersion relation

$$\omega_s(\mathbf{k}) = c_s(\hat{\mathbf{k}})k + \mathcal{O}(k^2), \quad (7.19)$$

where $c_s(\hat{\mathbf{k}})$ is the sound speed of the phonon mode in propagation direction $\hat{\mathbf{k}} = \mathbf{k}/k$. Generally speaking, polarization vectors $\hat{\mathbf{e}}_s(\hat{\mathbf{k}})$ are neither parallel nor perpendicular to $\hat{\mathbf{k}}$. However, for $ka \lesssim 1$, two of the phonon modes in a cubic lattice are approximately transverse, and the third mode is approximately longitudinal.

In Fig. 7.1 we show the phonon dispersion relations and polarization of a body centered cubic (BCC) lattice which are calculated from the dynamic matrix. The lower frequency modes in the left-panel of Fig. 7.1 correspond to the modes that are mostly transverse with $\hat{\mathbf{e}}_s \cdot \hat{\mathbf{k}} \approx 0$, and the higher frequency modes are mostly longitudinal with $|\hat{\mathbf{e}}_s \cdot \hat{\mathbf{k}}| \approx 1$.

Despite the relatively large spread of velocities associated with the transverse modes it is often useful to represent them by an ‘‘average velocity’’ denoted as c_t .

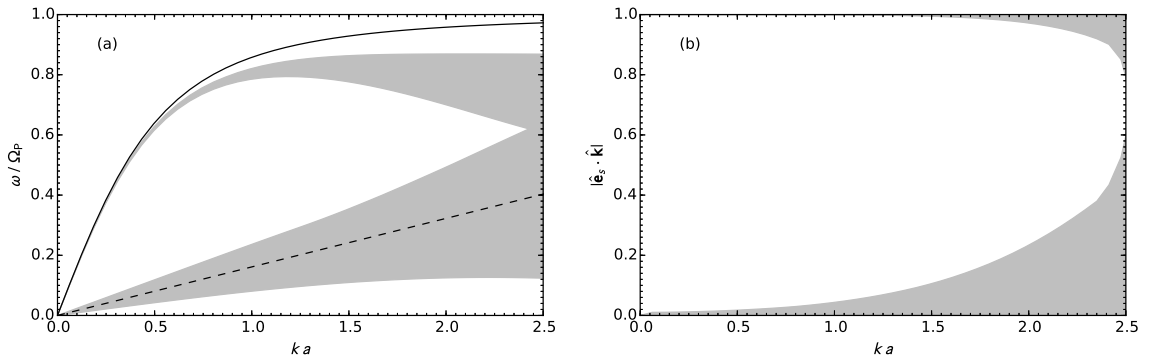


Figure 7.1: The dispersion relations of the phonon modes of the Coulomb lattice. Left panel: The phonon frequencies ω as functions of wave number k . The dashed and solid curves are for the transverse and longitudinal modes described by Eqs. (7.20) and (7.22), respectively. The shaded region gives the range of the eigenvalues of the dynamic matrix in Eq. (7.18). Right panel: The shaded region gives the range of $|\hat{\mathbf{e}}_s \cdot \hat{\mathbf{k}}|$ for the eigenvectors $\hat{\mathbf{e}}_s(\mathbf{k})$ of the dynamic matrix. The results in both panels are computed for the LD matter. Reprinted figure with permission from [S. Abbar et al, Phys. Rev. C 92, 045809, 2015](#) (Ref. (Abbar et al. 2015a)). Copyright 2015 by the American Physical Society.

This is typically defined by taking the limit of $k \rightarrow 0$ in which case

$$c_t = \frac{\alpha \Omega_P}{k_D} \approx 0.0031 \left(\frac{\alpha}{0.4} \right) \left(\frac{Z}{30} \right) \left(\frac{A}{80} \right)^{-2/3} \rho_{10}^{1/6}, \quad (7.20)$$

where $\alpha \approx 0.39$ according to (Chabrier et al. 1992), and

$$k_D = (6\pi^2 n_I)^{1/3} \approx (0.41a)^{-1} \quad (7.21)$$

is the Debye wave number. An approximate relation for the longitudinal mode is given by

$$\omega_l^2(k) = \frac{\Omega_P^2}{\epsilon(k)} \approx \frac{\Omega_P^2}{1 + (k_{TF}/k)^2}. \quad (7.22)$$

At low temperature it is useful to write the dynamic structure function as a sum of the contributions from n -phonon processes ($n = 0, 1, \dots$):

$$S(\omega, \mathbf{q}) = S^{(0)}(\omega, \mathbf{q}) + S^{(1)}(\omega, \mathbf{q}) + \dots \quad (7.23)$$

The elastic or Bragg scattering is the 0-phonon contribution and is given by

$$S^{(0)}(\omega, \mathbf{q}) = e^{-2W(q)} \delta(\omega) N \sum_{\mathbf{K}} \delta_{\mathbf{q}, \mathbf{K}}, \quad (7.24)$$

where \mathbf{K} is a reciprocal lattice vector, and

$$e^{-2W(q)} = \exp(-\langle [\mathbf{q} \cdot \mathbf{u}(0)]^2 \rangle_T) \quad (7.25)$$

is the Debye-Waller factor which accounts for the suppression of coherent scattering by thermal and quantum fluctuations of the ions. As mentioned earlier, the 0-phonon contribution does not affect electron scattering. At low temperature electron-ion scattering is dominated by the 1-phonon contribution

$$\begin{aligned} S^{(1)}(\omega, \mathbf{q}) = & \frac{e^{-2W}}{2M} \sum_{s, \mathbf{K}} \int d^3k \frac{[\mathbf{q} \cdot \hat{\mathbf{e}}_s(\mathbf{k})]^2}{\omega_s(\mathbf{k})} \delta^3(\mathbf{K} + \mathbf{k} - \mathbf{q}) \\ & \times \left[\frac{\delta(\omega - \omega_s(\mathbf{k}))}{e^{\omega_s(\mathbf{k})/T} - 1} + \frac{\delta(\omega + \omega_s(\mathbf{k}))}{1 - e^{-\omega_s(\mathbf{k})/T}} \right] \end{aligned} \quad (7.26)$$

where the phonon momentum \mathbf{k} is restricted to the first Brillouin zone (Flowers and Itoh 1976, Ashcroft and Mermin 1976). In this case, $S'_\kappa(q)$ in Eq. (7.10) can be replaced by

$$S_\kappa^{\text{OPA}}(q) = \int_{-\infty}^{\infty} d\omega \langle S^{(1)}(\omega, \mathbf{q}) \rangle_{\hat{\mathbf{q}}} w_\kappa(\omega/T, q). \quad (7.27)$$

Note that large-angle scattering involves a finite $|\mathbf{K}| \gg |\mathbf{k}|$ where the crystal absorbs a large component of the momentum. This is well-known as the Umklapp process in solid state physics (Ashcroft and Mermin 1976). Flowers and Itoh (1976) realized that these processes dominate over normal processes (with $\mathbf{K} = 0$) in the neutron star context for typical temperatures of interest because $p_F \gg k_D$. However, transitions with small \mathbf{k} and finite \mathbf{K} can be suppressed by the effects of the electronic band structure which we shall now briefly discuss.

Although it is generally a good approximation to assume that electrons are free, on patches of the electron Fermi surface which intersect with the Brillouin zone

boundaries, the effect of the periodic background ion potential is large. It distorts the Fermi surface and creates a band gap in the electron spectrum at the Fermi surface which is given by

$$\Delta\varepsilon(p_F) \simeq \frac{4e^2}{3\pi} \frac{e^{-W(p_F)} F(p_F)}{\epsilon(p_F)} p_F \quad (7.28)$$

where $F(p_F)$ is the charge form factor of the nucleus (Pethick and Thorsson 1997). This gap can suppress the Umklapp processes when

$$T \lesssim T_U \simeq c_t \Delta\varepsilon(p_F), \quad (7.29)$$

(Ziman 1960, Raikh and Yakovlev 1982, Chugunov 2012). From Eq. (7.29) we can deduce that $T_U < 10^{-2}\Omega_P$. In what follows we restrict our analysis to the regime where T is in the range $10^{-2} - 1 \Omega_P$ and where the effects due to the band gap in the electron spectrum can be safely neglected (Chugunov 2012).

To determine the temperature regimes where the static approximation $S'_\kappa(q) \approx S'(q)$ is valid, one can compute the static structure function $S'(q)$ in one-phonon approximation (OPA):

$$S^{\text{OPA}}(q) = \int_{-\infty}^{\infty} d\omega \langle S^{(1)}(\omega, \mathbf{q}) \rangle_{\mathbf{q}}. \quad (7.30)$$

In Fig. 7.2 we show $S'_\kappa(q)$ and $S^{\text{OPA}}(q)$ of the LD matter at three different temperatures, $T/\Omega_P = 0.03, 0.1$ and 0.3 , respectively. The right panel of this figure shows that, even at $T = 0.3 \Omega_P$, $S'_\kappa(q) = S'(q)$ is already a good approximation. The left panel of Fig. 7.2 shows that, at low temperature $T = 0.03 \Omega_P$, the exponential factor $1/(e^{\omega/T} - 1)$ in Eq. (7.15) dominates, and $S'_\kappa(q) \ll S'(q)$ in most of the range of q . The middle panel of Fig. 7.2 with $T = 0.1 \Omega_P$ illustrates the competition between two factors in the expression of w_κ at moderate temperatures, which are discussed earlier following Eq. (7.16) in Section 7.1. For large-angle scattering with $qa \gtrsim 5$ the exponential factor still dominates, and $S'_\kappa(q) < S'(q)$. For small-angle scattering

Chapter 7. Thermal Conductivity of the Neutron Star Crust

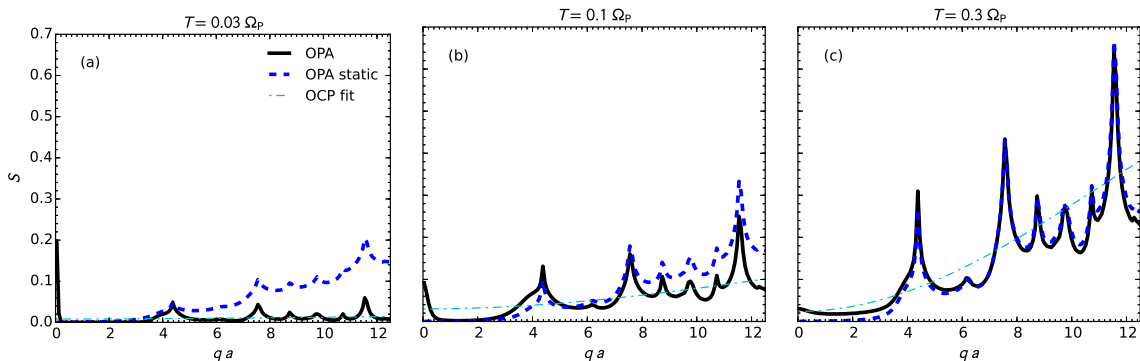


Figure 7.2: The one-phonon approximation results of $S'_\kappa(q)$ (thick solid curves) and $S'(q)$ (thick dashed curves) for the LD matter at the three temperatures as labelled. The results of $S'_\kappa(q)$ obtained using the fitting formula by Potekhin et al. (1999), which is based on the harmonic approximation for the one-component Coulomb plasma and which includes multi-phonon contributions, are also shown (as dot-dashed curves) for comparison. Reprinted figure with permission from [S. Abbar et al, Phys. Rev. C 92, 045809, 2015](#) (Ref. (Abbar et al. 2015a)). Copyright 2015 by the American Physical Society.

with $qa \lesssim 5$, however, the factor p_F^2/q^2 dominates, and $S'_\kappa(q) > S'(q)$. We note that at low temperature $S'_\kappa(q)$ has a peak at $q \rightarrow 0$ because

$$w_\kappa(\omega/T \ll 1, qa \ll 1) \approx 1 + \frac{3}{\pi^2} \left(\frac{p_F}{T}\right)^2 \left(\frac{\omega}{q}\right)^2,$$

and the second term in this expression always dominates under the typical conditions in the neutron star crust.

For comparison we also show in Fig. 7.2 the results of $S'_\kappa(q)$ obtained using the fitting formula by Potekhin et al. (1999) which is based on the harmonic approximation for the one-component Coulomb plasma and which includes multi-phonon contributions.

7.3 Static structure function and Monte Carlo simulations

The neutron star crust spans the regimes where purely classical simulations are sufficient and where quantum effects start to play a significant role. We can use classical and Quantum Monte Carlo simulations (CMC and QMC) to address these conditions. The QMC simulations have the classical simulations as a specific limit. Both the CMC and QMC calculations can easily address the static structure function $S(q)$. They can also be used to compute further information about the energy dependence of the response as well as other observables.

In CMC the kinetic and potential energies are independent variables. Hence the positions of the particles can be sampled independently of their momentum. One can use a simple version of the Metropolis Monte Carlo method to sample the positions of the nuclei in periodic boundary conditions at fixed density and temperature. The simulations use $N \gtrsim 1000$ particles, initially at predetermined lattice sites in a periodic cubic box with length $L = (N/n_I)^{1/3}$. Proposed particle moves $\{\mathbf{x}_i\} \rightarrow \{\mathbf{x}'_i\}$ have equal transition probabilities as their reverses:

$$\mathcal{T}(\{\mathbf{x}_i\} \rightarrow \{\mathbf{x}'_i\}) = \mathcal{T}(\{\mathbf{x}'_i\} \rightarrow \{\mathbf{x}_i\}), \quad (7.31)$$

and they are accepted with probabilities

$$P(\{\mathbf{x}_i\} \rightarrow \{\mathbf{x}'_i\}) = \begin{cases} e^{-\Delta E/T_\sigma} & \text{if } \Delta E \geq 0, \\ 1 & \text{otherwise.} \end{cases} \quad (7.32)$$

For CMC $T_\sigma = T$, and the energy change is the same as the change in total potential energy:

$$\Delta E = E_{\text{pot}}(\{\mathbf{x}'_i\}) - E_{\text{pot}}(\{\mathbf{x}_i\}), \quad (7.33)$$

where

$$E_{\text{pot}}(\{\mathbf{x}_i\}) = \sum_{i < j} V(|\mathbf{x}_i - \mathbf{x}_j|). \quad (7.34)$$

In Eq. (7.34) the sums over i and j run over the particles in the simulation volume plus their periodic images. Typically plus or minus one image in each direction (i.e. 27 periodic boxes in total) is sufficient in these simulations because of the screening of the ion-ion potential. Standard Ewald summation is also possible but would be slower. Detailed balance ensures that the Markov chain constructed with the method described above will converge eventually to sample particle positions proportional to the partition function.

Quantum fluctuations become important when $T/\Omega_{\text{P}} \lesssim 1$. For such scenarios one can use path integral QMC simulations (see, e.g., (Ceperley 1995)). The single position for each particle in the classical simulation becomes a path in path integral simulations with periodic boundary conditions in imaginary time. Boson or fermion path integrals would require exchanges in the imaginary time boundary conditions with the appropriate statistics, e.g. -1 for odd permutations of fermions. Because the characteristic distance λ_I of the ion motion in the lattice is much shorter than the inter-ion distance a , quantum statistics (the boson or fermion nature of nuclei) is not important, and we can consider the particles as distinguishable.

In (path integral) QMC simulations the imaginary time or inverse temperature $\beta = 1/T$ is split into N_β slices. Each slice is a classical N -particle system described above but with effective temperature

$$T_\sigma = (\Delta\tau)^{-1} = \left(\frac{\beta}{N_\beta}\right)^{-1}. \quad (7.35)$$

For QMC each imaginary-time slice involves a high-temperature expansion of the propagator $\exp(-H\Delta\tau)$. For a large enough number of slices N_β the results are independent of the number of slices. Typically of order 10 slices are required in the present calculations.

Chapter 7. Thermal Conductivity of the Neutron Star Crust

As in CMC, the Markov chain is again constructed by moving the particles according to the acceptance probability defined in Eq. (7.32). For QMC the energy change includes the changes in both kinetic and potential energies:

$$\begin{aligned} \Delta E = & [E_{\text{pot}}(\{\mathbf{x}'_{i,\sigma}\}) + E_{\text{kin}}(\{\mathbf{x}'_{i,\sigma}\})] \\ & - [E_{\text{pot}}(\{\mathbf{x}_{i,\sigma}\}) + E_{\text{kin}}(\{\mathbf{x}_{i,\sigma}\})], \end{aligned} \quad (7.36)$$

where

$$E_{\text{kin}}(\{\mathbf{x}_{i,\sigma}\}) = \sum_{i=1}^N \sum_{\sigma=1}^{N_\beta} \frac{(\mathbf{x}_{i,\sigma+1} - \mathbf{x}_{i,\sigma})^2}{2M(\Delta\tau)^2}, \quad (7.37)$$

$$E_{\text{pot}}(\{\mathbf{x}_{i,\sigma}\}) = \sum_{\sigma=1}^{N_\beta} \sum_{i<j} V(|\mathbf{x}_{i,\sigma} - \mathbf{x}_{j,\sigma}|) \quad (7.38)$$

with $\mathbf{x}_{i,N_\beta+1} = \mathbf{x}_{i,1}$. Clearly, a CMC simulation can be considered as a special case of QMC simulation with $N_\beta = 1$.

The static structure function is then obtained from the points sampled after convergence. In Monte Carlo simulations

$$S(q) = \frac{1}{NN_\beta} \left\langle \sum_{\sigma=1}^{N_\beta} \sum_{i,j=1}^N e^{i\mathbf{q}\cdot(\mathbf{x}_{i,\sigma} - \mathbf{x}_{j,\sigma})} \right\rangle_{\hat{\mathbf{q}}, T}, \quad (7.39)$$

which includes both the one-phonon and multi-phonon contributions. Because of the periodic condition,

$$\mathbf{q} = \frac{2\pi}{L} (n_x \hat{\mathbf{x}} + n_y \hat{\mathbf{y}} + n_z \hat{\mathbf{z}}) \quad (7.40)$$

take discrete values, where $n_{x(y,z)}$ are integers. To obtain the inelastic part of the static structure function $S'(q)$ we simply remove the points that correspond to the Bragg peaks in the BCC lattice. Other detailed structures predicted by QMC and CMC, i.e. the smaller peaks and troughs away from the Bragg peaks (see Fig. 7.3), are finite-size artifacts whose amplitude decreases with increasing particle number in the simulation. However, the integrated strength over any reasonable interval

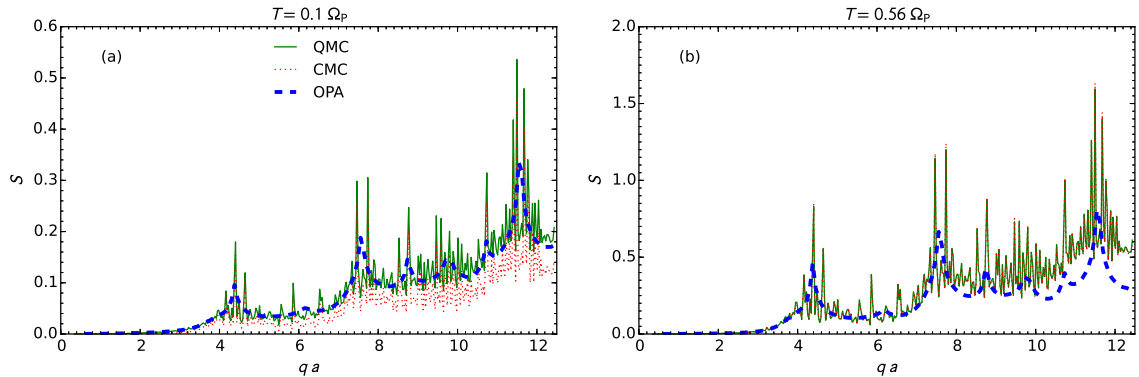


Figure 7.3: The inelastic part of static structure function $S'(q)$ of the LD matter at the two temperatures as labelled. The results are obtained using the one-phonon approximation (thick dashed curves), and quantum and classical Monte Carlo simulations (solid and dotted curves), respectively. Reprinted figure with permission from S. Abbar et al, *Phys. Rev. C* 92, 045809, 2015 (Ref. (Abbar et al. 2015a)). Copyright 2015 by the American Physical Society.

in q is physically relevant and is insensitive to finite-size effects after the numerical convergence has been achieved.

At high temperature $T \gtrsim \Omega_P$ all phonon modes are excited and $S^{\text{CMC}}(q)$ and $S^{\text{QMC}}(q)$, which are $S'(q)$ obtained using CMC and QMC simulations, respectively, should agree. But at low temperature $T \ll \Omega_P$ quantum fluctuations become prominent, and $S^{\text{QMC}}(q) > S^{\text{CMC}}(q)$. In Fig. 7.3 we compare $S^{\text{CMC}}(q)$ and $S^{\text{QMC}}(q)$ for the LD matter at two different temperatures, $T/\Omega_P = 0.1$ and 0.56 , respectively. Indeed, $S^{\text{QMC}}(q)$ is clearly larger than $S^{\text{CMC}}(q)$ at $T = 0.1 \Omega_P$, but it is somewhat surprising that $S^{\text{CMC}}(q)$ and $S^{\text{QMC}}(q)$ agree very well even at temperature as low as $T = 0.56 \Omega_P$.

For comparison we also show $S^{\text{OPA}}(q)$ in Fig. 7.3. This figure shows that $S^{\text{QMC}}(q)$ and $S^{\text{OPA}}(q)$ agree with each other at low T and/or small q , although there exist rapid oscillations in Monte Carlo results because of the finite size of the system. At high T and/or large q multi-phonon contributions are significant, and the one-phonon

approximation breaks down.

Note that in Eq. (7.39) only the equal-time correlator has been evaluated. By including an offset in the imaginary times between the evaluations of positions of particles i and j ,

$$S(s\Delta\tau, q) = \frac{1}{NN_\beta} \left\langle \sum_{\sigma=1}^{N_\beta} \sum_{i,j=1}^N e^{i\mathbf{q}\cdot(\mathbf{x}_{i,\sigma} - \mathbf{x}_{j,\sigma+s})} \right\rangle_{\mathbf{q}, T}, \quad (7.41)$$

one can obtain information of the energy dependence of the response (Ceperley 1995). It is also possible to calculate the properties of MCP in both the classical and quantum regimes. This would require simulations significantly larger than the OCP studied here, to ensure that the periodic boundary conditions do not impact the results. Simulations of this magnitude should be readily achievable on modern parallel computers.

7.4 Discussion

We have calculated the thermal conductivity of OCP for the LD and HD ambient conditions outlined in Table 7.1 for the temperatures of interest to neutron star phenomenology. To this end we use the various approximate methods outlined in previous sections to calculate $S'_\kappa(q)$, which is the kernel function for computing effective electron collision rate ν_κ in Eq. (7.10). We then calculated κ for the catalyzed neutron star matter with densities 10^{10} g cm $^{-3}$ (LD) and 10^{11} g cm $^{-3}$ (HD), respectively. The results are shown in Fig. 7.4 where the thermal conductivity is obtained by replacing $S'_\kappa(q)$ with $S_\kappa^{\text{OPA}}(q)$ (thick solid curves), $S^{\text{OPA}}(q)$ (thick dashed curves), $S_\kappa^{\text{OPA}}(q)$ with simple phonon dispersion relations [see Eqs. (7.20) and (7.22)] (thin solid curves), the fitting formula of $S'_\kappa(q)$ based on the harmonic approximation (Potekhin et al. 1999) (thin dot-dashed curves), $S^{\text{QMC}}(q)$ (filled circles) and $S^{\text{CMC}}(q)$ (filled squares), respectively.

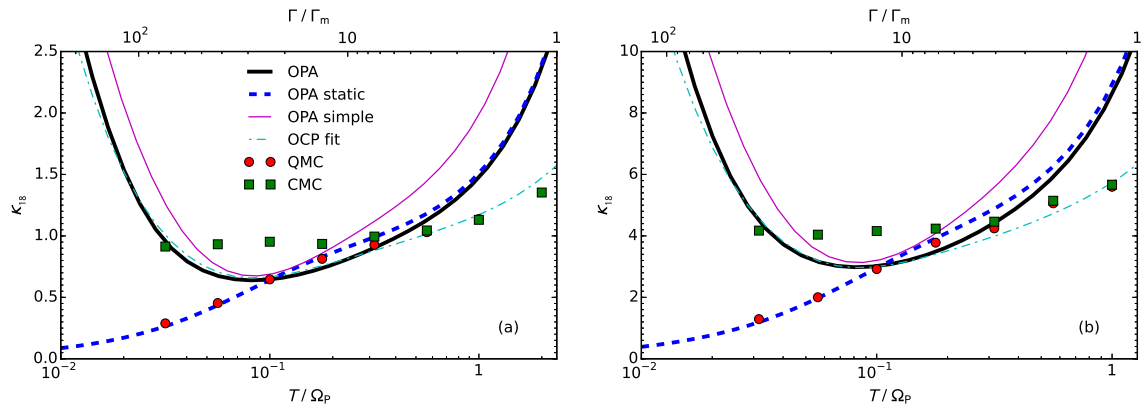


Figure 7.4: Thermal conductivity of the LD (left panel) and HD matter (right panel) in units of $10^{18} \text{ erg cm}^{-1} \text{ s}^{-1} \text{ K}^{-1}$ and as a function of temperature. The results are obtained by replacing $S'_\kappa(q)$ in Eq. (7.10) with $S_\kappa^{\text{OPA}}(q)$ (thick solid curves), $S^{\text{OPA}}(q)$ (thick dashed curves), $S_\kappa^{\text{OPA}}(q)$ with approximate phonon dispersion relations [see Eqs. (7.20) and (7.22)] (thin solid curves), fitting formula of $S'_\kappa(q)$ for one-component Coulomb plasma based on the harmonic approximation (Potekhin et al. 1999) (thin dot-dashed curves), $S^{\text{QMC}}(q)$ (filled circles) and $S^{\text{CMC}}(q)$ (filled squares), respectively. Reprinted figure with permission from S. Abbar et al, *Phys. Rev. C* 92, 045809, 2015 (Ref. (Abbar et al. 2015a)). Copyright 2015 by the American Physical Society.

A careful comparison of the results obtained using different approximations for the function $S'_\kappa(q)$ provides the following useful insights:

1. It is adequate to set $S'_\kappa(q) = S'(q)$ in calculating κ at temperature as low as $T \approx 0.1 \Omega_P$. A comparison between the thick dashed curves obtained using $S^{\text{OPA}}(q)$ and the thick solid curves obtained using $S_\kappa^{\text{OPA}}(q)$ supports this conclusion. The validity of this approximation is expected and well known for $T \gtrsim \Omega_P$. One can see that $S'_\kappa(q) \approx S'(q)$ even at $T = 0.3 \Omega_P$ (see Fig. 7.2). Further, for $0.1 \lesssim T/\Omega_P \lesssim 0.3$, this approximate method can still be used to compute κ even though $S'_\kappa(q)$ and $S'(q)$ differ. This is because there are two competing factors in $w_\kappa(\omega/T, q)$ which are discussed earlier following Eq. (7.30) in Section 7.1.

2. Multi-phonon effects become relevant for $\Gamma/\Gamma_m \lesssim 4$ in our simulations. At higher Γ or lower temperature the one-phonon approximation is adequate for OCP but is sensitive to the phonon dispersion relation. This is evident when we compare the thick solid curves, the thin solid curves and thin dot-dashed curves, which are obtained using the exact phonon dispersion relations from the dynamical matrix, the approximate phonon dispersion relations, and the harmonic approximation method with multi-phonon contributions (Potekhin et al. 1999), respectively.
3. The comparison between the results obtained using CMC and QMC simulations, shown by the filled squares and circles, respectively, indicates that quantum effects in thermal conductivity are significant when $T \lesssim 0.3 \Omega_P$ where classical calculations systematically underestimate $S'(q)$. At $T \approx 0.1 \Omega_P$ CMC results overestimate κ by about 30%.
4. The fitting formula for $S'_\kappa(q)$ which is based on the harmonic approximation (Potekhin et al. 1999) (dot-dashed curves) works quite well for the one-component Coulomb lattice in the whole temperature range which we have studied. This can be seen when we compare them with the thick solid curves at $T \lesssim 0.3 \Omega_P$ and filled circles/squares at $T \gtrsim 0.3 \Omega_P$ which are obtained using the one-phonon approximation and Monte Carlo simulations, respectively. At the highest temperature where $\Gamma \approx \Gamma_m$ the results obtained using the harmonic approximation include multi-phonon excitations and agree well with the QMC results. This indicates that anharmonic effects are small even in this regime. At the lowest temperatures, although the $S'_\kappa(q)$ obtained from the fitting formula based on the harmonic approximation differs from that obtained in the OPA (see Fig. 7.2), the predictions for the thermal conductivity agree well as already discussed in (Potekhin et al. 1999).

Some of the trends emerging from these comparisons could have been be ex-

pected qualitatively. As previously alluded to, this systematic quantitative comparisons between QMC results and those obtained using the standard electron-phonon treatment provide a basis to assess the viability of using QMC calculations of $S(q)$ at low temperature for complex multi-component systems. In the standard treatment, multi-component systems are modeled as a regular lattice plus uncorrelated impurities, and electron scattering is assumed to arise due to incoherent contributions from electron-phonon and electron-impurity scattering. This treatment fails when the spatial distribution of the minority species is correlated, and QMC is a viable technique to calculate the role of these correlations in strongly coupled plasmas with $\Gamma \gg 1$ in the regime when $T < \Omega_P$.

One observes that $S(q)$ obtained from QMC is adequate to calculate κ for $T \gtrsim 0.1 \Omega_P$, and CMC may be adequate to compute thermal conductivity of OCP at $T \gtrsim 0.3 \Omega_P$. For lower temperatures, more detailed information about the energy dependence of the response is needed and we have briefly commented on how we can access this in the discussion following Eq. (7.41).

Chapter 8

Summary and Outlook

In this dissertation, I have studied two important aspects of the physics of supernovae and neutron stars. In the first part, I show that the spatial and time symmetries can be broken spontaneously in a dense neutrino gas. I show that neutrino flavor oscillations can occur on very small length scales if the neutrino density is sufficiently large. In the presence of matter, our results suggest that the matter suppresses flavor conversions at smaller neutrino number densities. It does so by pushing neutrino flavor instabilities to larger neutrino number densities.

I also show that the stationarity of a neutrino gas can be broken due to the presence of neutrino-neutrino interaction. Our results suggest that the onset radii of significant flavor conversion are similar for time-dependent and time-independent neutrino gases unless there exist extremely rapid initial perturbations in the neutrino gases. When the flavor conversion occurs, however, we do expect qualitatively different behaviors in the two scenarios.

In our studies we have focused on the neutrino flavor instabilities in the linear regime. However, it is important to check if these instabilities develop into full oscillations in the nonlinear regime in a time-dependent and inhomogeneous neutrino

Chapter 8. Summary and Outlook

gas. It is expected that this could be a very challenging problem. When the symmetries of the neutrino gas are broken, one needs to solve neutrino oscillations in models with larger dimensions. Our results also suggest that the problem of spurious oscillations could be more severe in an inhomogeneous neutrino gas.

In our research, we have used a simple matter profile which is a slowly¹ varying function of radius. The question yet to be answered is whether a fast varying matter profile such as what one expects in the turbulence can affect the instabilities of the homogeneous and inhomogeneous modes. It is possible that the turbulence in the direction perpendicular to the direction of the neutrino propagation can affect the instabilities in the inhomogeneous mode.

In the second part of the dissertation I study the thermal conductivity of the outer crust of the neutron star as a function of temperature at low temperatures ($T \lesssim \Omega_P$). We show that the quantum effects become important when $T \lesssim 0.3 \Omega_P$. At $T \simeq 0.1 \Omega_P$ the quantum effects suppress κ by about 30%. We also show that the dynamical information become necessary when $T \lesssim 0.1 \Omega_P$.

In our calculations, we have modeled the neutron star crust as a one-component plasma. However, as discussed in Chapter 7 a more realistic calculation must include a configuration consisting of multiple ion species. The calculations with the multi-component plasma can be challenging from the computational point of view. We have also ignored the effects of the large magnetic fields that can exist on the surface of the neutron star.

In the future, we will remove some of these limitations in our current study and we will investigate the new effects that may arise in the more realistic models.

¹The variation of the matter density should be sufficiently slow in comparison with flavor variations in the neutrino gas.

References

- Abbar, S., Carlson, J., Duan, H., and Reddy, S. (2015a). Quantum Monte Carlo calculations of the thermal conductivity of neutron star crusts. *Phys. Rev.*, C92(4).
- Abbar, S. and Duan, H. (2015). Neutrino flavor instabilities in a time-dependent supernova model. *Phys. Lett.*, B751.
- Abbar, S., Duan, H., and Shalgar, S. (2015b). Flavor instabilities in the multiangle neutrino line model. *Phys. Rev.*, D92(6).
- Ashcroft, N. and Mermin, N. (1976). *Solid State Physics*. Saunders College, Philadelphia.
- Baade, W. and Zwicky, F. (1934). Remarks on super-novae and cosmic rays. *Phys. Rev.*, 46(1).
- Banerjee, A., Dighe, A., and Raffelt, G. (2011). Linearized flavor-stability analysis of dense neutrino streams. *Phys. Rev.*, D84.
- Brown, E. F. and Cumming, A. (2009). Mapping crustal heating with the cooling lightcurves of quasi-persistent transients. *Astrophys. J.*, 698.
- Burrows, A., Hayes, J., and Fryxell, B. A. (1995). On the nature of core collapse supernova explosions. *Astrophys. J.*, 450.

REFERENCES

- Cardall, C. Y. (2008). Liouville equations for neutrino distribution matrices. *Phys. Rev.*, D78.
- Carr, W. J. (1961). Energy, Specific Heat, and Magnetic Properties of the Low-Density Electron Gas. *Phys. Rev.*, 122.
- Ceperley, D. M. (1995). Path integrals in the theory of condensed helium. *Rev. of Mod. Phys.*, 67.
- Chabrier, G., Ashcroft, N. W., and Dewitt, H. E. (1992). White dwarfs as quantum crystals. *Nature*, 360.
- Chadwick, J. (1932). Possible existence of a neutron. *Nature*, 129(3252).
- Chakraborty, S., Hansen, R. S., Izaguirre, I., and Raffelt, G. (2016). Self-induced flavor conversion of supernova neutrinos on small scales. *JCAP*, 1601(01).
- Chamel, N. and Haensel, P. (2008). Physics of neutron star crusts. *Living Rev. Relat.*, 11(10).
- Chandrasekhar, S. (1934). Stellar configurations with degenerate cores. *The Observatory*, 57.
- Cherry, J. F., Carlson, J., Friedland, A., Fuller, G. M., and Vlasenko, A. (2012). Neutrino scattering and flavor transformation in supernovae. *Phys. Rev. Lett.*, 108.
- Chugunov, A. I. (2012). Electrical conductivity of the neutron star crust at low temperatures. *Astron. Lett.*, 38.
- Cleveland, B. T., Daily, T., Davis Jr, R., Distel, J. R., Lande, K., Lee, C., Wildenhain, P. S., and Ullman, J. (1998). Measurement of the solar electron neutrino flux with the homestake chlorine detector. *Astrophys. J.*, 496(1).

REFERENCES

- Da Silva, L. (1993). The classification of supernovae. *Astrophys. space sci.*, 202(2).
- Duan, H. and Friedland, A. (2011). Self-induced suppression of collective neutrino oscillations in a supernova. *Phys. Rev. Lett.*, 106.
- Duan, H., Fuller, G. M., Carlson, J., and Qian, Y.-Z. (2006a). Coherent development of neutrino flavor in the supernova environment. *Phys. Rev. Lett.*, 97(24).
- Duan, H., Fuller, G. M., Carlson, J., and Qian, Y.-Z. (2006b). Coherent development of neutrino flavor in the supernova environment. *Phys. Rev. Lett.*, 97.
- Duan, H., Fuller, G. M., Carlson, J., and Qian, Y.-Z. (2006c). Simulation of coherent nonlinear neutrino flavor transformation in the supernova environment: Correlated neutrino trajectories. *Phys. Rev.*, D74(10).
- Duan, H., Fuller, G. M., and Qian, Y.-Z. (2006d). Collective neutrino flavor transformation in supernovae. *Phys. Rev.*, D74.
- Duan, H., Fuller, G. M., and Qian, Y.-Z. (2007). Simple picture for neutrino flavor transformation in supernovae. *Phys. Rev.*, D76(8).
- Duan, H., Fuller, G. M., and Qian, Y.-Z. (2010). Collective Neutrino Oscillations. *Ann. Rev. Nucl. Part. Sci.*, 60.
- Duan, H. and Shalgar, S. (2014). Multipole expansion method for supernova neutrino oscillations. *JCAP*, 1410(10).
- Duan, H. and Shalgar, S. (2015). Flavor instabilities in the neutrino line model. *Phys. Lett.*, B747.
- Eichler, D. and Cheng, A. F. (1989). Thermal afterglow from transient energy release in neutron stars. *Astrophys. J.*, 336.
- Esteban-Pretel, A. et al. (2008). Role of dense matter in collective supernova neutrino transformations. *Phys. Rev.*, D78.

REFERENCES

- Esteban-Pretel, A., Pastor, S., Tomas, R., Raffelt, G. G., and Sigl, G. (2007). De-coherence in supernova neutrino transformations suppressed by deleptonization. *Phys. Rev.*, D76(12).
- Flowers, E. and Itoh, N. (1976). Transport properties of dense matter. *Astrophys. J.*, 206.
- Friedland, A. (2010). Self-refraction of supernova neutrinos: mixed spectra and three-flavor instabilities. *Phys. Rev. Lett.*, 104.
- Fukuda, Y., Hayakawa, T., Ichihara, E., Inoue, K., Ishihara, K., Ishino, H., Itow, Y., Kajita, T., Kameda, J., Kasuga, S., et al. (1998). Evidence for oscillation of atmospheric neutrinos. *Phys. Rev. Lett.*, 81(8).
- Giunti, C. and Kim, C. W. (2007). *Fundamentals of neutrino physics and astrophysics*. Oxford University Press, Oxford.
- Gudmundsson, E. H., Pethick, C., and Epstein, R. I. (1983). Structure of neutron star envelopes. *Astrophys. J.*, 272.
- Haxton, W. C. (1995). The solar neutrino problem. *Ann. Rev. Astron. Astrophys.*, 33.
- Heger, A., Fryer, C., Woosley, S., Langer, N., and Hartmann, D. H. (2003). How massive single stars end their life. *Astrophys. J.*, 591(1).
- Hewish, A., Bell, S. J., Pilkington, J., Scott, P., and Collins, R. (1968). Observation of a rapidly pulsating radio source. *Nature*, 217(5130).
- Hopkins, A. (2013). Australian astronomical observatory. *Asia Pacific Physics Newsletter*, 2(02).
- Janka, H. T., Hanke, F., Huedepohl, L., Marek, A., Mueller, B., and Obergaulinger, M. (2012). Core-Collapse Supernovae: Reflections and Directions. *PTEP*, 2012.

REFERENCES

- Jones, M. D. and Ceperley, D. M. (1996). Crystallization of the one-component plasma at finite temperature. *Phys. Rev. Lett.*, 76.
- Keil, M. T., Raffelt, G. G., and Janka, H.-T. (2003). Monte carlo study of supernova neutrino spectra formation. *Astrophys. J.*, 590(2).
- Kippenhahn, R., Weigert, A., and Weiss, A. (1990). *Stellar structure and evolution*, volume 44. Springer, Heidelberg.
- Koranda, S., Stergioulas, N., and Friedman, J. L. (1997). Upper limits set by causality on the rotation and mass of uniformly rotating relativistic stars. *Astrophys. J.*, 488(2).
- Lattimer, J. M. and Prakash, M. (2016). The equation of state of hot, dense matter and neutron stars. *Phys. Rep.*, 621.
- Mangano, G., Mirizzi, A., and Saviano, N. (2014). Damping the neutrino flavor pendulum by breaking homogeneity. *Phys. Rev.*, D89(7).
- Mirizzi, A. (2013). Multi-azimuthal-angle effects in self-induced supernova neutrino flavor conversions without axial symmetry. *Phys. Rev.*, D88(7).
- Mirizzi, A. (2015). Breaking the symmetries in self-induced flavor conversions of neutrino beams from a ring. *Phys. Rev.*, D92(10).
- Mirizzi, A., Mangano, G., and Saviano, N. (2015). Self-induced flavor instabilities of a dense neutrino stream in a two-dimensional model. *Phys. Rev.*, D92(2).
- Mirizzi, A. and Serpico, P. D. (2012). Instability in the Dense Supernova Neutrino Gas with Flavor-Dependent Angular Distributions. *Phys. Rev. Lett.*, 108.
- Olive, K. A. et al. (2014). Review of Particle Physics. *Chin. Phys.*, C38:090001.
- Oppenheimer, J. R. and Volkoff, G. M. (1939). On massive neutron cores. *Phys. Rev.*, 55(4).

REFERENCES

- Page, D. and Reddy, S. (2006). Dense Matter in Compact Stars: Theoretical Developments and Observational Constraints. *Annu. Rev. Nucl. Part. Sci.*, 56.
- Page, D. and Reddy, S. (2012). *Thermal and transport properties of the neutron star inner crust*. Space Science, Exploration and Policies. NOVA.
- Page, D. and Reddy, S. (2013). Forecasting neutron star temperatures: predictability and variability. *Phys. Rev. Lett.*, 111.
- Peskin, M. and Schroeder, D. (1995). An introduction to quantum field theory.
- Pethick, C. and Thorsson, V. (1997). Effects of electron band structure on neutrino pair bremsstrahlung in neutron star crusts. *Phys. Rev.*, D56.
- Pontecorvo, B. (1957). Mesonium and antimesonium. *Zhur. Eksptl'. i Teoret. Fiz.*, 33.
- Pontecorvo, B. (1958). Mesonium and antimesonium. *Soviet Phys. JETP*, 6.
- Potekhin, A. Y., Baiko, D. A., Haensel, P., and Yakovlev, D. G. (1999). Transport properties of degenerate electrons in neutron star envelopes and white dwarf cores. *Astron. Astrophys.*, 346.
- Qian, X. and Vogel, P. (2015). Neutrino mass hierarchy. *Prog. Part. Nucl. Phys.*, 83.
- Qian, Y.-Z. and Fuller, G. M. (1995). Neutrino-neutrino scattering and matter-enhanced neutrino flavor transformation in supernovae. *Phys. Rev.*, D51(4):1479.
- Raffelt, G., Sarikas, S., and Seixas, D. d. S. (2013). Axial symmetry breaking in self-induced flavor conversion of supernova neutrino fluxes. *Phys. Rev. Lett.*, 111.
- Raffelt, G. G. (1996). *Stars as laboratories for fundamental physics: The astrophysics of neutrinos, axions, and other weakly interacting particles*. University of Chicago press, Chicago.

REFERENCES

- Raikh, M. E. and Yakovlev, D. G. (1982). Thermal and electrical conductivities of crystals in neutron stars and degenerate white dwarfs. *Astrophys. Space Sci.*, 87.
- Rhoades Jr, C. E. and Ruffini, R. (1974). Maximum mass of a neutron star. *Phys. Rev. Lett.*, 32(6).
- Richardson, M., Van Horn, H., Ratcliff, K., and Malone, R. (1982). Neutron star evolutionary sequences. *Astrophys. J.*, 255.
- Rutledge, R. E., Bildsten, L., Brown, E. F., Pavlov, G. G., Zavlin, V. E., and Ushomirsky, G. (2002). Crustal Emission and the Quiescent Spectrum of the Neutron Star in KS 1731-260. *Astrophys. J.*, 580.
- Sarikas, S., Seixas, D. d. S., and Raffelt, G. (2012). Spurious instabilities in multi-angle simulations of collective flavor conversion. *Phys. Rev.*, D86.
- Sawyer, R. F. (2016). Neutrino cloud instabilities just above the neutrino sphere of a supernova. *Phys. Rev. Lett.*, 116(8).
- Shapiro, S. L. and Teukolsky, S. A. (2008). *Black holes, white dwarfs and neutron stars: the physics of compact objects*. John Wiley & Sons, Weinheim.
- Shternin, P. S., Yakovlev, D. G., Haensel, P., and Potekhin, A. Y. (2007). Neutron star cooling after deep crustal heating in the X-ray transient KS 1731-260. *Monthly Notices of the RAS*, 382.
- Sigl, G. and Raffelt, G. (1993). General kinetic description of relativistic mixed neutrinos. *Nucl. Phys.*, B406.
- Slattery, W. L., Doolen, G. D., and DeWitt, H. E. (1980). Improved equation of state for the classical one-component plasma. *Phys. Rev.*, A21.
- Slattery, W. L., Doolen, G. D., and DeWitt, H. E. (1982). N dependence in the classical one-component plasma monte carlo calculations. *Phys. Rev.*, A26.

REFERENCES

- Strack, P. and Burrows, A. (2005). A generalized boltzmann formalism for oscillating neutrinos. *Phys. Rev.*, D71.
- Ziman, J. (1960). *Electrons and Phonons: The Theory of Transport Phenomena in Solids*. International series of monographs on physics. Oxford University Press, Oxford.